Title
Multifuntional Zeolitic Porous Chalcogenide

Author
Chen, Xitong

Publication Date
2017

UNIVERSITY OF CALIFORNIA
RIVERSIDE

Multifuntional Zeolitic Porous Chalcogenides

A Dissertation submitted in partial satisfaction
of the requirements for the degree of

Doctor of Philosophy

in

Chemistry

by

Xitong Chen

December 2017

Dissertation Committee:
    Dr. Pingyun Feng, Chairperson
    Dr. Yadong Yin
    Dr. Hill Harman

The Dissertation of Xitong Chen is approved:

____

____

____
Committee Chairperson

University of California, Riverside

Acknowledgement

By taking this opportunity, I want to express my gratitude to everyone who supported me throughout my Ph.D. study and research. I am thankful for their aspiring guidance and invaluable constructive advice. I am sincerely grateful to everyone for their patience and support in overcoming numerous obstacles I have been facing through my research.

Foremost, I would like to express my sincere appreciation to my advisor Prof. Pingyun Feng for the continuous support of my Ph.D. study and research. I am so proud that I can join her research team. Her patience, motivation, broad knowledge and insight always give me motivation to keep ahead. Her constant guidance and encouragement helped me in all the time of research and writing of this thesis. For her unwavering support, I am truly grateful.

I also want to thank Prof. Xianhui Bu from CSULB for the valuable discussions. It's great pleasure to collaborate with him. His warm help, insightful suggestions and active collaborations encouraged me in continuing current work and creating new ideas.

I am also grateful to all of the past and current group members from Prof. Pingyun Feng's research team. First of all, I want to thank two postdoctoral researchers in the past: Dr. Qipu Lin and Dr. Quanguo Zhai. I have learned a lot from their experience, knowledge and technical support. I also want to thank Dr. Xiang Zhao for his great personality, help and advice. Moreover, I want to thank: Dr. Yang Hou, Dr. Fan Zuo, Dr. Le Wang, Dr. Jikai Liu, Dr. Fei Bu, Dr. Chengyu Mao, Dr. Koroush Sasan, Dr. Yuan Wang and Yanxiang Wang. It's great experience to work with them.

I am also thankful to my committee members Prof. Yangdong Yin and Prof. Hill Harman for their valuable comments on my dissertation. Especially, I want to express my sincere appreciation to Prof. Robert Cort Haddon, who is the chairperson of committee in my oral qualifying exam.

I also would like to thank the staff in Department of Chemistry for their kindly help.

Last but not the least, I would like to thank my mother, Zhihong Meng, and my father, Chaocun Chen for everything they did for me. None of this would be possible without their deeply love and support. Their moral and emotional supports are the most valuable motivation for me to overcome every obstacle thorough my Ph.D. research and study.

Dedication

To my mother Zhihong Meng and father Chaocun Chen

ABSTRACT OF THE DISSERTATION

Multifuntional Zeolitic Porous Chalcogenides

by

Xitong Chen

Doctor of Philosophy, Graduate Program in Chemistry
University of California, Riverside, December 2017
Dr. Pingyun Feng, Chairperson

Crystalline porous metal chalcogenides have attracted extensive attentions due to its integration of highly porous structure and semiconducting property. Our research group has made great contributions to the development of chalcogenide molecular clusters with their three-dimensional (3D) structures.

While most of the previous efforts are devoted to developing new crystal structures, research on the functionalization of this kind of materials are somewhat ignored. As built from well-defined nanoclusters, the metal chalcogenide materials can build a bridge between the molecular clusters and the resulting three-dimensional structures. By controlling the chemical composition on the nano-sized clusters or tuning the host-guest chemistry in the frameworks, custom-design functionalization can be realized.

Among them, zeolitic porous chalcogenide, possessing the zeotype structures, stands out due to its high thermal and chemical stability, high porosity, flexible chemical composition and accessible cation-exchange property.

In the first part of this work, trimetallic zeolitic porous chalcogenides with tunable chemical compositions were successfully developed. The valence and ionic diameter of the metal cations, were found as the key factors affecting the self-assembling process. Through tuning the chemical composition with different atomic ratio in the molecular clusters, tunable band gaps can be successfully realized. The studies here build a bridge between the molecular semiconducting clusters and the resulting frameworks, providing a systematic investigation on the structural retention and alternation of zeolitic porous chalcogenides. The as-synthesized frameworks exhibit the selective photocatalytic properties. By integration of high porosity, semiconductivity and cation-exchange property, a promising platform is well demonstrated for the development of selective photocatalytic materials.

In the second part, functionalization of zeolitic porous chalcogenide through cation exchange are well demonstrated. Because of their unique integration of the chalcogen-soft surface, high porosity, all-inorganic crystalline framework, and the tunable charge-to-volume ratio of exchangeable cations, a special family of porous chalcogenides for CO_2 adsorption in terms of extraordinarily high selectivity, large uptake capacity, and robust structure is developed. Moreover, zeolitic porous chalcogenide can serve as the dual hard template for fabricating the heteroatom doped carbon materials for electrocatalytic reactions with high efficiency.

Table of Contents

List of Figures

List of Tables

List of Schemes

Chapter 1 Introduction

1.1 Crystalline Porous Materials

Due to their controllable pore structure, precise pore size, high surface area and high density active sites inside the pore structure, CPMs (Crystalline Porous Materials) have been widely used not only in the traditional areas, such as heterogeneous catalysis[1], adsorbent[2] and ion-exchange[3], but also in some novel emerging fields from electronics[4] to medical diagnosis[5].

Crystalline porous materials involve various classes of solid state materials such as metal oxides including zeolite[6-8], metal phosphate[9-11] and metal chalcogenide open frameworks[12-14], covalent organic frameworks (COFs)[15-17] and metal-organic frameworks (MOFs)[18-20]. Compared with amorphous porous materials, due to its well-defined pore structure with long range ordering of atoms, more chemical information can be derived with CPMs. For instance, the well-defined pore size can endow the crystalline material with selective adsorption and exclusion.[21-23]

Based on the pore size, the porous materials can be divided into microporous (with pore diameter smaller than 2nm), mesoporous (with pore diameter larger than 2nm but smaller than 50nm) and macroporous (with pore size larger than 50nm) materials.[24] Materials with different porosities can possess unique advantages towards different functionalities. Among them, microporous material have exhibited promising applications in the selective capture and catalysis of small molecules. Compared with mesoporous and macroporous materials, more active sites are located inside the microporous structures, which will be beneficial for interaction towards small molecules. Moreover, the confinement effect will be much helpful for trapping small gas molecules.

During the several past decades, much of efforts have been devoted to synthesizing new structures. Lots of new topologies were emerged along with new type of crystalline porous materials. In comparison, exploring their intriguing properties and applications needs more attention.

1.2 From Microporous Metal Oxide to Metal Chalcogenide Open Framework

1.2.1 Zeolite

Zeolite is the first member of microporous crystalline materials due to the existence of natural zeolites.[25, 26] Zeolite is the porous structure of aluminosilicate. The tetrahedral SiO_4 and AlO_4 building blocks join together through sharing the corner oxygen atoms, resulting in the three-dimensional (3D) porous structures, which is the structural feature in the zeolite. It is worth noting that two AlO_4 building blocks cannot directly connect together by sharing corner oxygen atoms, based on Lowensteins' rule.

The tetrahedral building blocks (SiO_4 or AlO_4) join together, forming the rings with different numbers of nodes. (Figure 1.1 (a)) Three common rings are four-membered, six-membered and eight-membered rings. The combination of four-membered and six-membered rings can give α-cage and the combination of four-membered and eight-membered rings will result in β-cage. (Figure 1.1 (b)) These cages with different sizes of apertures can endow the materials with selective adsorption or catalytic properties.

Zeolites have been widely used in industrial production. Due to the existence of AlO_4 in the framework, the host framework is negatively charged, which needs the cationic species, such as alkaline metal or tetraalkylammonium cations, as charge-balanced species in the channel. Those cations can be exchanged with other metal cations, indicating the promising application in the field of ion-exchange, such as removal of heavy metal and radioactive metal cations in waste water, desalination of seawater and hard water softening. The appearance of high-silica zeolite, such as ZSM-5[27, 28], have been widely applied in the catalytic reaction of petroleum. In addition, as mentioned above, the well-defined porous cages can trap some small molecules with specific shapes, which can be used in the purification of gas and liquid.

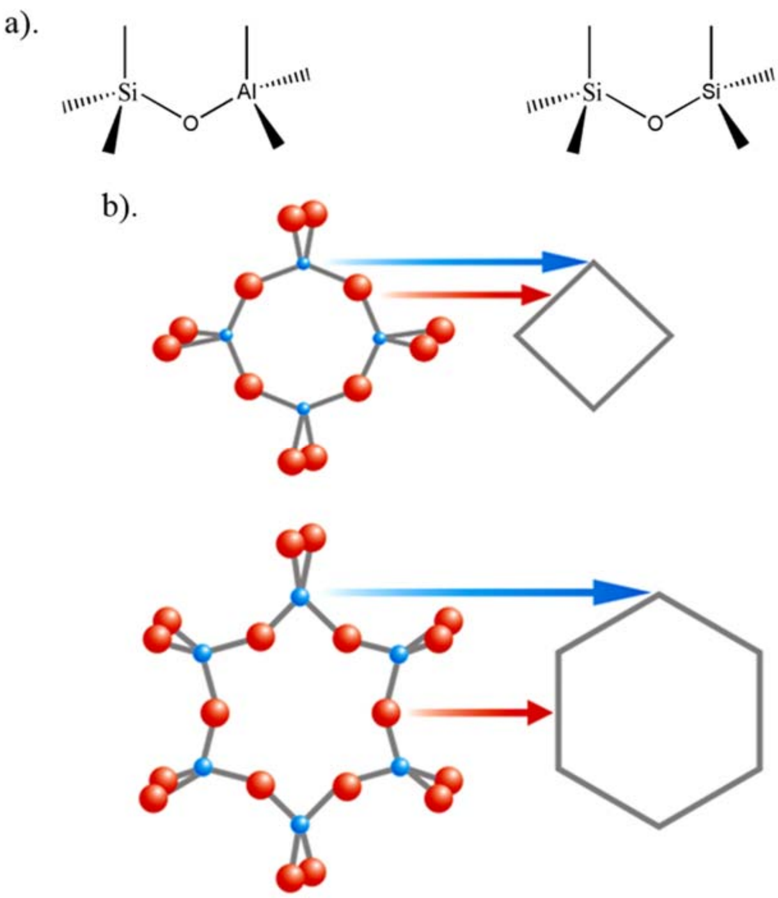

Figure 1.1 Schematic illustration of a). The connecting modes between different SiO_4 and AlO_4 tetrahedron; b). four- and six-membered rings made of different tetrahedrons with their similpificaitons.

1.2.2 Metal-Phosphate Open Framework

In addition to zeolites, over the past few decades, much efforts have been devoted to develop new zeolite-like molecular sieves. In 1982, a class of non-aluminosilicate, aluminophosphate, was firstly synthesized by Flanigen et al.[29] Later on, a lot of research groups worked on this new type of microporous crystalline materials. Replacement of Si^{4+} and partial of Al^{3+} cations with P^{5+} and transition metal cations, such as Co^{2+}, Fe^{2+}, Mn^{2+}

and Zn^{2+}, could produce zeolite analogues with diverse chemical compositions ,structural types and even large membered rings (Figure 1.2), implying a generalized synthetic method to generate transition-metal-rich zeolite-type structures.[9, 10] Besides, the newly developed synthetic parameters, such as the structure-directing agents with different sizes, shapes and polarities, played a vital role in the search for new types of metal phosphate zeolite analogues.

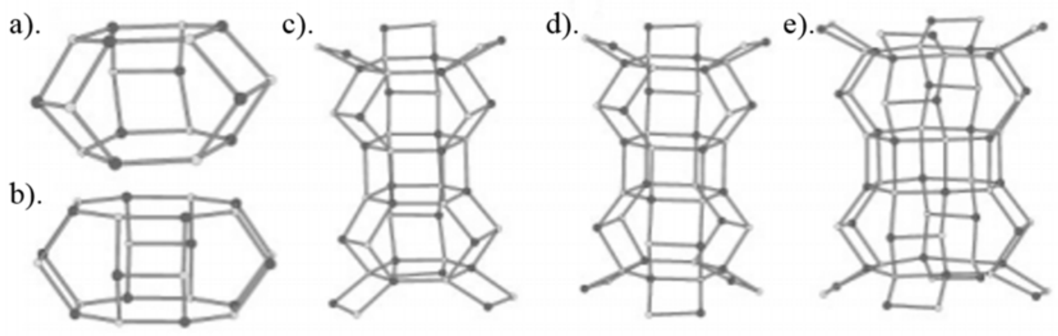

Figure 1.2 a). The *can* cage in UCSB-6 and UCSB-10; b). the *ocn* cage in UCSB-8; c). the capped (m)-*can*-D6R-*can* unit in UCSB-6; d). the capped (i)-*can*-D6R-can unit in UCSB-10 and e) the capped (m)-*ocn*-D8R-*ocn* unit in UCSB-8.

1.2.3 Metal Chalcogenide Open Framework

The basic building blocks in zeolite or metal phosphate materials are MO_4 tetrahedron, rather limiting the pore sizes. Moreover, the large band gaps or insulating properties in these materials indicate that they are hardly applied in areas such as optics and electronics. These limitations can be avoided in another class of zeolite analogue, metal chalcogenide open framework, since the solid state metal sulfide materials with the semiconducting properties has already shown lots of promising properties such as photocatalysis, photoelectrocatalysis, solar cells and energy storage. The first open framework metal chalcogenide was reported by Bedard in 1989.[30] Since then, metal chalcogenides arouse lots of research interest and have been well developed.[31, 32] As most of metal chalcogenides mimic the 4 connection mode in zeolite, it integrates the porosity and semiconducting property, exhibiting potential applications in optics and electronics.

In zeolite, oxygen atoms are shared by two MO_4 tetrahedrons. In metal chalcogenides, the framework anions O^{2-} are replaced by chalcogens (S^{2-} or Se^{2-}). From the viewpoint of chemical composition, the discrepancy of oxides and sulfides can guide the materials to different applications. Besides this, with the replacement of oxygen by chalcogen, it is worth noting that the resulting microporous structures are different from the perspective of the structural chemistry. M-X-M (X= chalcogen anion) angles are typically within the range 105° ~115°, which is much smaller and less flexible than M-O-M in open framework oxides (100° ~180°). In addition, the M-X bond length (typically larger than 2.1Å) is much larger than that in metal oxides.

It is worth noting that chalcogen anions possess a much larger ionic radius than that of O^{2-}, meaning there would be more coordination cations surrounding the center chalcogen anions. For instance, the coordination number of sulfur anions easily go up to 4, even with large metal cations such as Cd^{2+}. However, the linkage mode of oxygen in zeolite are usually bi-coordinated bridging mode. It is hard for the small sized oxygen anions to accommodate four cations. The rich coordination modes of chalcogen anion could induce the clustering in the solutions before crystallization process. In addition, as shown in Figure 1.3, with the rich linkage modes of chalcogen anions (bi-coordinated, three-coordinated or four-coordinated), there are more opportunities in open framework metal chalcogenide for the constructions of new types of structures beyond the limitation of zeolite types, which are restricted by the bridging mode of oxygen anions.[33-35]

Except devising the linkage mode at the corner, the chalcogenide clusters, which can be simplified as the artificial tetrahedral atoms in the zeolite, are tunable in sizes and chemical compositions, thus providing the secondary level of structural controlling.

It is also worth mentioning that as a well-defined molecular cluster, it can build a bridge between semiconducting nanoclusters and 3D covalent superlattice. By tuning the chemical composition or the size of the nanocluster, the properties of the resulting porous structure can be rationally modified, thus realizing the target properties or applications from the molecular level.[36]

In the following chapter, I would like to give a brief review for crystalline porous metal chalcogenide open framework. Since our interest focused on the zeolite analogue, most of the framework discussed here would adopt the 4-connected building blocks. By rationally selecting four-coordinated metal cations and chalcogen atoms, variety of metal chalcogenide frameworks mimicking the 4-connecting mode can be synthesized. Different from the fixed MO_4 building blocks in zeolite, the size of the building blocks in metal chalcogenides can be tunable, which would make the suitable pore size in the framework.

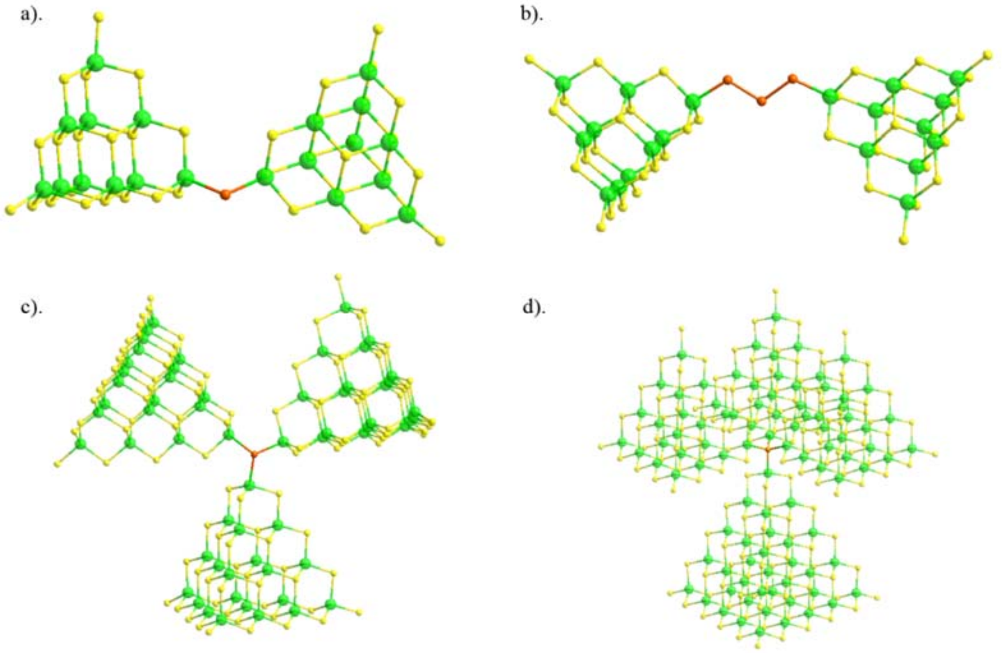

Figure 1.3 Different linkage mode of corner chalcogen anions. a). bicoordinated S2- connecting two T3 clusters; b). S-S-S bridges connecting two T4 clusters; c). tricoordinated S2- connecting three T4 clusters; d). tetracoordinated S2- connecting four T5 clusters. Green balls represent the metal cations, yellow balls represents the chalcogen anions inside the supertetrahedral clusters and orange balls represent the connecting chalcogenide anions between clusters.

1.3 Open Framework Chalcogenide Based on Supertetrahesral Clusters

1.3.1 Charge-Density Matching Principle

Before we begin to talk about the designing of basic building blocks in metal chalcogenides, there are two principles we should pay attentions to: local charge-density matching and global charge-density matching.[32] Due to the various coordination modes of chalcogen anions, the coordination number should relate to the total valence from the metal cations surrounding it. Simply, the valence of the anion (-2 for chalcogen anion and -1 for the thiolate) should be quite closed to the sum of the electrostatic bond strengths contributed from neighboring cations to it. For example, for a three-coordinated S^{2-} it cannot bond to three tetrahedrally coordinated Ge^{4+} or Sn^{4+} since the overall electrostatic bond strengths from the cations are nearly +3, much more overwhelming the negative two charges on one sulfur. The same situation can be applied to the four-coordinated chalcogen anions.

The global charge-density matching principle relates to the overall charge of the host frameworks. It describes the relationships between the negatively charged framework and the positively charged extra-framework species. The common charge-balanced species are protonated amine, tetraalkyammonium and alkaline metal cations.

1.3.2 Basic Building Blocks in Metal Chalcogenide Open Framework

Much of efforts on designing and synthesizing open framework metal chalcogenide have ficused on the tetrahedral clusters, distinctively different from the basic MO_4 tetrahedron metal oxide open framework materials. This is because of the tetrahedral coordination of metal cations with the rich coordination modes of chalcogen anions. From the viewpoint of chemical composition, the most widely used metal cations in tetrahedral clusters are from Groups 12-14 metals (Zn^{2+}, Cd^{2+}, Ga^{3+}, In^{3+}, Ge^{4+} and Sn^{4+}). Besides, Li^{+}, Mn^{2+}, Fe^{2+}, Co^{2+} and Cu^{+} can also be used in the constructions of tetrahedral clusters as well.

Up to now, there are totally four kinds of tetrahedral cluster appearing in metal chalcogenide open framework. In terms of the structural features, they are called supertetrahedral cluster (Tn), penta-supertetrahedral cluster (Pn), capped-supertetrahedral cluster (Cn) and super-supertetrahedral cluster (Tp,q), respectively. The most common, also the most fundamental series of tetrahedral cluster is supertetraheal cluster. The remaining three kinds of clusters can be derived from this series. My research work in the following chapters in this dissertation focus on the frameworks built from the supertetraheal clusters.

Supertetrahedral cluster, denoted as Tn, where n is the number of metal layers, is actually the regular, tetrahedrally shaped fragments of cubic ZnS lattice, as shown in Figure 1.4. The chemical composition of isolated T1, T2, T3, T4 and T5 clusters are MX4, M_4X_{10}, $M_{10}X_{20}$, $M_{20}X_{35}$ and $M_{35}X_{56}$, respectively. Here M represents the tetrahedrally coordinated metal cations and X represents the chalcogenide anions. As shown in the series, the number of anions in a Tn cluster is equal to the number of anions in T(n+1) cluster. Generally, in an isolated Tn cluster, the number of cations will be [n(n+1)(n+2)]/6 and the number of anions will be [(n+1)(n+2)(n+3)]/6. The common linkage mode for the corner sulfur anions is bi-coordinated, demonstrating that the corner sulfur anions are usually shared by two supertetrahedral clusters and these Tn clusters can function as the artificial and tetrahedrally coordinated atoms in zeolite. Following this guideline, the number of anion sites in each cluster will be reduced by 2 when forming 3D structures. Since 4 corner S^{2-} are expected to be shared between two different clusters, the largest supertetrahedral cluster synthesized is T5, in both isolated form and 3D covalent lattice so far. As there exists a relationship between the dimension size of the cluster and the resulting properties, it is worth seeking for a route to synthesize large sized Tn clusters. Some of reported supertetrahedral clusters are given as examples here, as summarized in Table 1.1.

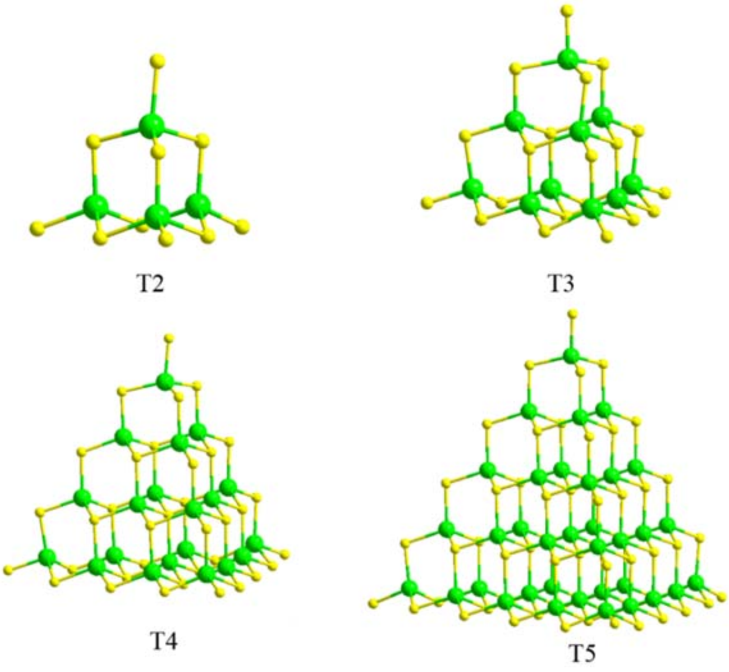
T2

T3

T4

T5

Figure 1.4 Schematic illustration of supertetrahedral T2, T3, T4 and T5 clusters. The green balls represent the metal cations and yellow balls represent the chalcogen anions.

The initial research work on supertetrahedral clusters began with the isolated T2 clusters in the aqueous solution such as $[Ge_4S_{10}]^{4-}$, $[Ga_4S_{10}]^{8-}$, $[In_4S_{10}]^{8-}$ and $[In_4Se_{10}]^{8-}$.[37, 38] The one with thiolate groups also exists, such as $[Cd_4(SPh)_{10}]^{2-}$ and $[Zn_4(SPh)^{10}]^{2-}$.[39] Three-dimensional structure didn't appear until some groups used transition metal cations such as Cu^+, Ag^+, Mn^{2+} and Fe^{2+} to connect $[Ge_4S_{10}]^{4-}$ together.[40-43] The incorporated transition metal cations helped to lower the overall negative charge of the framework, which was then charge-balanced by the structure directing agent such as tetramethylammonium cations. All of these frameworks possess the non-interpenetrating diamond superlattice. Later on, a double diamond type structure based on $[Ge_4S_{10}]^{4-}$ cluster was synthesized through the acidic polymerization of $[Ge_4S_{10}]^{4-}$.[44] It is worth mentioning that the composition is GeS_2 with a neutral framework, mimicking the high-silica zeolite such as ZSM-5.

Table 1.1 A summary of selected supertetrahedral clusters reported previously.

n	Stoichiometry	Examples
1	MX_4	$[MS_4]^{6-}$ (M=Mn, Fe, Co, Zn, Cd); $[MS_4]^{5-}$ (M= In, Ga); $[ME_4]^{4-}$ (M=Ge, Sn; E= S, Se, Te); $[M(SPh)_4]^{2-}$ (M= Zn, Cd, Co); $[M(SPh)_4]^{-}$ (M=Ga, In)
2	M_4X_{10}	$[Ge_4E_{10}]^{4-}$ (E= S, Se); $[Sn_4E_{10}]^{4-}$ (E= Se, Te); $[M_4S_{10}]^{8-}$ (M= Ga, In); $[In_4Se_{10}]^{8-}$; $[M_4(SPh)_{10}]^{2-}$ (M= Co, Fe, Zn, Cd)
3	$M_{10}X_{20}$	$[M_{10}E_{20}]^{10-}$ (M= Ga, In; E= S, Se); $[Sn_5Mn_5S_{20}]^{10-}$; $[Ga_{10}S_{16}(SH)(3,5\text{-}DMP)_3]^{3-}$; $[Ga_{10}S_{16}(SH)(3,4\text{-}DMP)_3]^{3-}$; $[In_{10}S_{16}(DBN)_4]^{2-}$; $[Ga_{10}S_{16}(3,5\text{-}Lutidine)_4]^{2-}$; $[M_{10}E_4(SPh)_{16}]^{4-}$ (M= Zn, Cd; E= S, Se);
4	$M_{20}X_{35}$	$[M_4In_{16}S_{35}]^{14-}$ (M= Mn, Fe, Co, Zn, Cd); $[Zn_4Ga_{16}E_{35}]^{14-}$ (E= S, Se); $[In_{16}M_4S_{31}(DBN)_4]^{6-}$ (M= Mn, Fe, Co, Cd); $[In_{16}Cd_4S_{31}(DMBIM)_2(DBN)_2]^{7-}$
5	$M_{35}X_{56}$	$[Cu_5In_{30}S_{56}]^{17-}$; $[Zn_{13}In_{22}S_{56}]^{20-}$; $[Cu_5In_{30}S_{52}(SH)_2Cl_2]^{13-}$; $[Cu_5Ga_{30}S_{52}(SH)_4]^{13-}$; $[Cu_5Ga_{30}S_{52}(SH)_2(Bim)_2]^{11-}$; $[Cu_5Ga_{30}S_{52}(SH)_{1.5}Cl(Bim)_{1.5}]^{11.5-}$; $[In_{22}Cd_{13}S_{52}(1\text{-}MIM)_4]^{12-}$
6	$M_{56}X_{84}$	None
≥ 7	M_xX_y	None

(x= [n(n+1)(n+2)]/6; y= [(n+1)(n+2)(n+3)]/6; 3,5-DMP = 3,5-dimethylpyridine; 3,4-DMP = 3,4- dimethylpyridine; DBN = 1,5 diazabicyclo[4.3.0]non-5-ene; 1-MIM = 1-methylimidazole; DMBIM = 5,6-dimethylbenzimidazolate; Bim= 1-butyl-2,3-dimethylimidazolium)

Although there was one neutral framework based on only T2 clusters successfully synthesized, other frameworks had not been realized until trivalent metal cations was incorporated into T2 clusters with Ge^{4+} or Sn^{4+}.[45-47] Possibly this was because the mixed valent T2 clusters would result in a negatively charged frameworks, which needed the protonated amines functioning as the charge-balanced and structure-directing agent inside the channels or cages. These T2 clusters could be assembled into four topologies, and they were sodalite, single diamond, augmented diamond and CrB_4, respectively, as shown in Figure 1.5. Among them, the protonated amine in UCR-20-GaGeS-TAEA could be exchanged out successfully with Cs^+ and the resulting structure had a surface area as high as 599 cm^2/g.

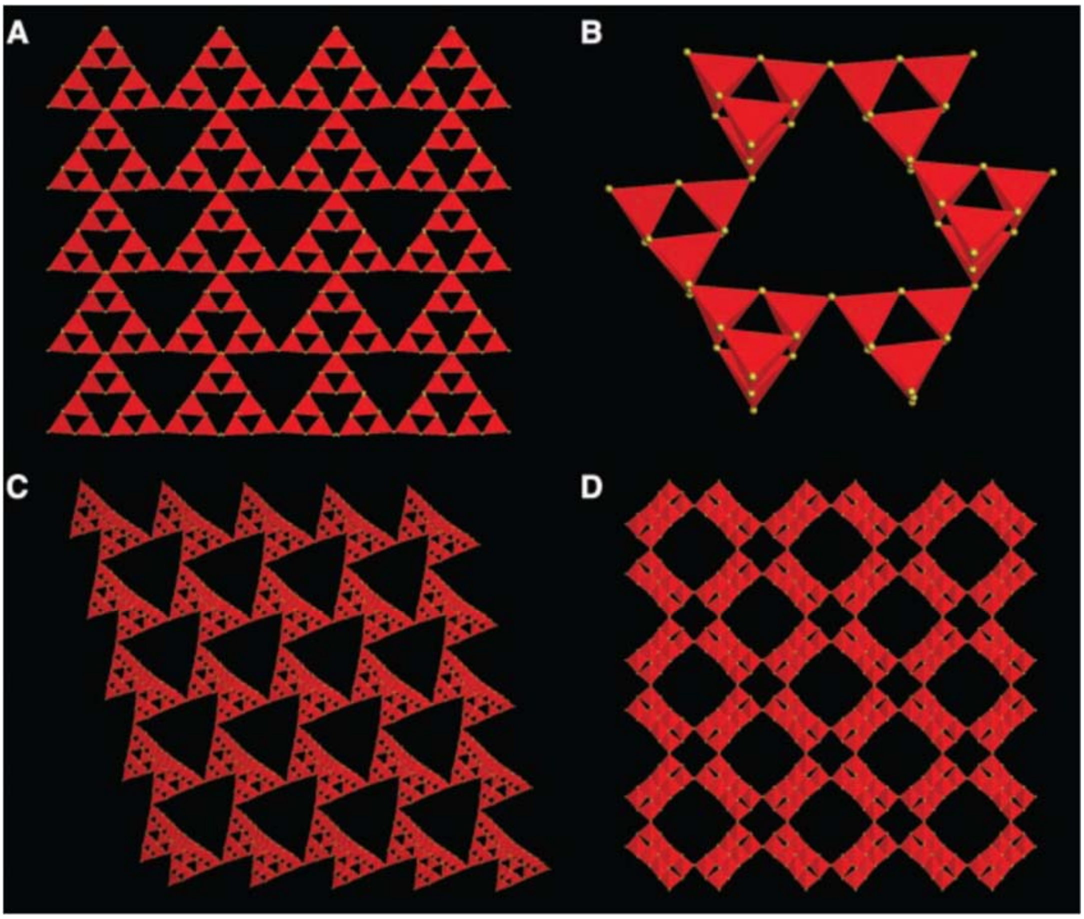

Figure 1.5 Four different 3D structures based on supertetrahedral T2 clusters. a). six-membered rings in supersodalite type UCR-20; b). Six-membered rings in single diamond type UCR-21; c). augmented-augmented diamond type of UCR-22; d). CrB_4 type of UCR-23.

With only tetravalent metal cations in the Tn cluster, the largest supertetrahedral cluster obtained so far was T2. It is because in T2 clusters, all chaocogen anions are μ_2 modes. In comparison, μ_3-chalcogen anion begin to appear in T3 clusters. According to the local charge-density matching principle, tetravalent metal cations cannot satisfy the coordination environment of μ_3 chalcogen anions. However, there is a special case in Sn-X (X=S^{2-} or Se^{2-}) system, where the oxygen atoms can be stuffed in the adamantane cages. As shown in Figure 1.6, in T3 clusters, four oxygen atoms can be located in the center of four adamantane cages, thus alleviating the total electrostatic bond strengths from the Sn^{4+} on the μ_3 chalcogen anion. The first such case in the literature was reported by John B. Parise in 1994.[48] The basic building block was $[Sn_{10}S_{20}O_4]^{8-}$ "stuffed" T3 cluster. Through the corner sharing by two adjacent clusters, two interwoven nets gave the cristobalite type structure with the formula of $[Sn_{10}S_{18}O_4]^{4-}$. The isolated form of "stuffed" T3 cluster also exists, with a formula of $[Cs_8Sn_{10}S_{20}O_4]\cdot 13H_2O$. Very recently, our group synthesized a "stuffed" T3 selenide cluster, which was $[Sn_{10}Se_{20}O_4]^{8-}$ and denoted as OCF-61-SnOSe.[49] In OCF-62-SnOSe, four T3 clusters assembled into one T2 cluster, if each T3 cluster is treated as one artificial tetrahedral atom. The name of this cluster was T3,2, called as super-supertetrahedral cluster. These T3,2 clusters joined together through the corner sharing mode, giving the resulting 2D (4,4) net.

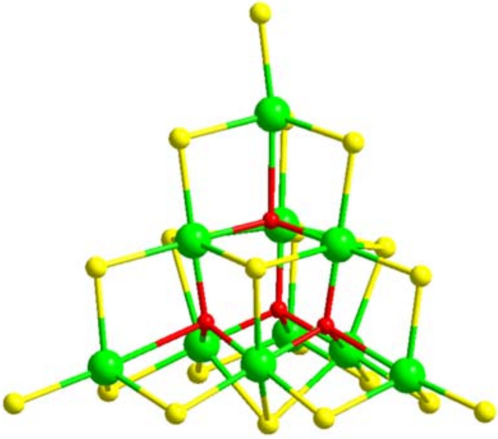

Figure 1.6 Stick and ball representation of oxygen stuffed T3 $[Sn_{10}S_{20}O_4]^{8-}$ cluster. Yellow balls represent S^{2-}, red balls represent O^{2-} and green balls represent Sn^{4+}.

Regular T3 clusters can be easily synthesized when the tetravalent metal cations were replaced by trivalent metal cations since the relatively low charge on metal cations such as In^{3+} can make μ_3-chalcogen anion possible. John B. Parise reported the first T3 cluster in 1998, where T3 $[In^{10}S^{20}]^{10-}$ clusters assembled into two-interpenetrating diamond superlattice, which was also called double diamond net.[50] Later on, O. M. Yaghi reported several open frameworks based on this T3 clusters.[51, 52] Here, it is worth mentioning that in metal oxide open framework, there are always some metal cations with a valence ≥ 4. In addition, two AlO_4 or InO_4 tetrahedron cannot share one O^{2-} in zeolites. But these limitations can be eliminated in metal chalcogenide frameworks. In this area, our group extended T3 clusters beyond In-S systems, synthesized quite a few frameworks in Ga-S, Ga-Se and In-Se systems.[33, 53, 54] Several new topologies and new connection modes had also been successfully explored. It is worth mentioning that the nonaqueous solutions was the key factor leading to the formation of Ga-S clusters.

When divalent or monovalent metal cations are incorporated into In-S system, larger clusters such as T4 and T5 can be formed. From T4 clusters, there will be a T(n-4) cluster in the core of Tn cluster. (Here, T0 cluster is a chalcogen anion) For example, in T4 cluster, there is a tetrahedrally coordinated chalcogen anion in the core position, which needs to be charge-balanced by four divalent metal cations bonding to it in order to achieve the local charge-density matching. O. M. Yaghi firstly reported a T4 cluster, $[Cd_4In_{16}S_{35}]^{14-}$, proving the approach mentioned above was a right way to obtain large clusters.[55] Later on, our group reported a special case of T5 cluster, which was synthesized from In-S composition. In order to achieve the local charge density matching, the core In^{3+} atoms were missing in the clusters, which was called coreless T5 cluster.[56] Li also reported a similar example, coreless $[In_{28}Cd_6S_{54}]^{12-}$ T5 cluster, in which the core position was unoccupied.[57] Then our group reported the first regular T5 cluster through the combination of tetravalent and monovalent metal cations- $[Cu_5In_{30}S_{54}]^{13-}$, which could assemble into 2D (4,4) net or 3D two interpenetrating zinc blende superlattice.[58] So far, the largest cluster synthesized is T5 cluster, no matter in superlattice or isolated form.[59, 60] The isolated form was realized through the superbase route.

In the supertetrahedral clusters, there are few cases where more than two metal cations, especially with different valences, co-exist in one cluster. The only reported cases were OCF-5 and OCF-40 in Sn-Ga-Zn-Se composition, both of which were made of T4 clusters. However, metal cations with different valences were distributed in different sites of the same cluster due to the local charge matching. For instance, Sn^{4+} was located at corner sites and Zn^{2+} was bonded to the core Se^{2-} site. The remaining metal sites were occupied by Ga^{3+}.

1.3.3 Assembly of Supertetrahedral Clusters into 3D Open Framework

If the linkage mode of corner chaocogen anion is bridging bicoordinated, each Tn clusters can be identified as four-connected artificial atom in zeolite type structure. However, the multi-coordinated mode of chalcogen anion (up to 4) could result in more types of structure beyond zeolite type. The rigid angle of M-X-M limit the number of topologies developed in metal chalcogenide frameworks. Up to now, there are only around ten topologies appeared, such as diamond, double diamond, ABW, sodalite, CrB_4, Cubic C3N4, UCR-1, ICF-24, ICF-25 and qzh.

It is well worth mentioning that when the cluster sizes are T4 and T5, most of the structures are diamond and double diamond types. Other topologies such as sodalite and CrB_4 can only be realized thorough the assembly of T2 or T3 clusters.

In addition, different sizes of clusters can be joined together. For example, UCR-19 possess the double diamond type structure made of alternate T3 and T4 clusters.[33] Another double diamond type structure made of T3 and coreless T5 clusters can be seen in UCR-15.[56] In OCF-42, alternate T2 and T4 clusters are joined together, also giving the double diamond type structure.[61]

1.3.4 Applications of Metal Chalcogenide Open Frameworks

In addition to synthesize the new types of structures during the past few years. There were some applications explored in this field.

Similar to the zeolite, the highly negative host framework endows them with good ion exchange property. The protonated amine molecules in the channel can be exchanged out by the alkali metal cations such as Cs^+, thus revealing the porous nature of the framework. For example, in UCR-20-GaGeS-TAEA, the protonated TAEA molecules can be exchanged out completely by Cs^+. The resulting porous framework shows type I isotherm towards nitrogen adsorption, which is the characteristic of the microporous material. The BET surface is 599 cm^2/g.[45] The extra-frameworks species Cs^+ can be replaced by K^+ through a further cation exchange which is denoted as K@RWY. K^+ in K@RWY can then be exchanged out by Cs^+,[62] showing excellent selectivity, high capacity, good stability in acidic or alkaline solution and excellent resistance to γ- and β-irradiation towards the capture of the radioactive waste Cs^+, as shown in Figure 1.7.

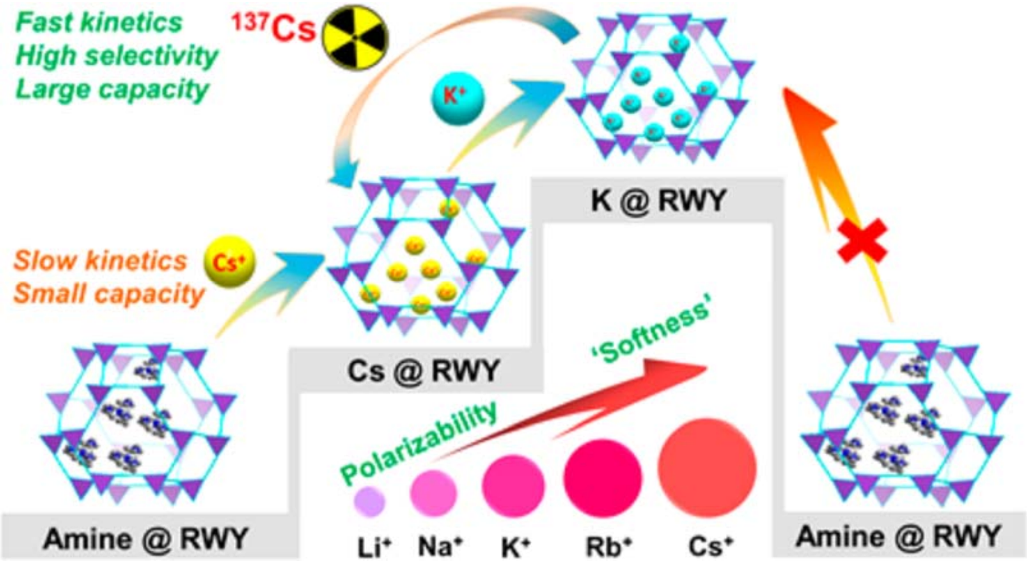

Figure 1.7 Schematic illustration of UCR-20 serving for selective trap of Cs^+ through step-by-step cation exchange.

Mercouri G. Kanatzidis reported an oxygen "stuffed" T4 clusters, $[In_4Sn_{16}O_{10}S_{34}]^{12-}$, different from the oxygen "stuffed" T3 Sn-S clusters appeared before. Due to the soft Lewis basic property of S^{2-}, this framework exhibited highly selective trapping heavy metal cations such as Pb^{2+}, Cd^{2+}, Hg^{2+} from aqueous solutions containing high concentrations of Na^+, Ca^{2+}, NH_4^+, Mg^{2+}, Zn^{2+}, CO_3^{2-}, PO_4^{3-} and CH_3COO^-.[63]

Our group synthesized a series of hydrated metal chalcogenide open frameworks using the inorganic metal cations as the charge-balanced species in aqueous solutions.[64] It is worth mentioning that some of the uncommon clusters can be synthesized with this strategy. For example, $[In_4Se_8]^{4-}$ T2 clusters, which cannot be synthesized from the amine-directed solutions, can be realized in inorganic system, possibly because of the high charge density of the inorganic cations. Due to the existence of hydrated inorganic cations in the channel, these materials exhibit the fast-ion conductivity at room temperature and at moderate or high humidity. For example, in ICF-21 InSe-Na, the ion conductivity at 21°C under 100% relative humidity is 3.4×10^{-2} $\text{ohm}^{-1}\text{cm}^{-1}$. In another case, ICF-22 InS-Li shows the conductivity of 1.1×10^{-2} $\text{ohm}^{-1}\text{cm}^{-1}$ at 24°C under 31.7% relative humidity. Those values are among the highest conductivity in crystalline porous materials.

Due to the semiconducting properties, these materials also show quite promising application in photocatalytic hydrogen evolution. Due to the porous properties, there should be more available active sites in the channel. In porous semiconducting materials, the electrons or holes do not need to travel a long distance in order to reach the external surface of the materials, thus reducing the possibility of electron hole combinations. One early study in our group showed that ICF-5 CuInS-Na[65] could exhibit hydrogen evolution of 18 $\mu\text{mol h}^{-1}\ \text{g}^{-1}$ under visible light irradiation when 0.5M Na_2S was applied as the sacrificial agent. However, the poor stability of this material limited its practical applications.

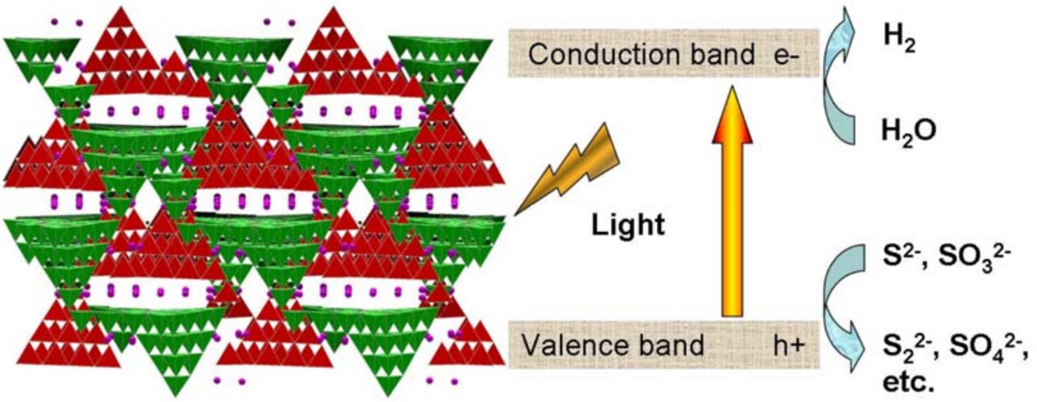

Figure 1.8 Schematic illustration of photocatalytic mechanism in metal chalcogenide open frameworks.

Recently our group reported a new super-sodalite type framework made of T2 clusters, denoted as CPM-120-ZnGeS-AEM,[46] which was analogous to UCR-20-GaGeS-TAEA. However, in the new framework, the ratio of Ge^{4+} to Zn^{2+} was almost 4:1, thus mimicking the high-silica zeolites, such as ZSM-5. In industrial production, ZSM-5 is a star material and is a critical catalyst for petroleum catalysis and cracking. This germanium-rich super-sodalite type framework has high thermo- and chemical-stability. For example, it can be stable up to 610 °C in nitrogen and 310 °C in air. This highly stable material possesses a quite broad range of applications such as selective gas adsorption, ion conductivity, phtotelectrochemical catalysis and photocatalytic hydrogen production. In the area of selective gas adsorption, at 1 atm, CO_2 uptake was 98 cm^3 g^{-1} at 273K and 73 cm^3 g^{-1} at 298K. The most exciting application was its function as photocatalyst for water splitting. When Na_2S-Na_2SO_3 was applied as the sacrificial reagent, the hydrogen production was

200μmol h^{-1}/(0.1g) under UV-vis light irradiation. Such excellent performance could be maintained for at least 200 hours, demonstrating the excellent resistance to photocorrosion.

Metal chalcogenide open framework was also applied as electrocatalyst. Wu and co-worked reported an interrupted zeolite-analogue metal chalcogenide functioning as oxygen reduction reaction (ORR) electrocatalyst.[66] In this structure, there were two basic building blocks: $[In_4Se_{10}]^{8-}$ and $[In_4Se_9O]^{8-}$. $[In_4Se_{10}]^{8-}$ cluster connected to four $[In_4Se_{10}]^{8-}$ clusters and each $[In_4Se_9O]^{8-}$ cluster connected to three $[In_4Se_{10}]^{8-}$ clusters. In $[In_4Se_9O]^{8-}$ cluster, three corners were occupied by the Se^{2-} with the remaining one occupied by a water molecule. This specific indium site bonding to the water molecule was responsible for the excellent ORR performance. Due to the tricoordinated charteristic, Bi^{3+} could precisely replace the position of In^{3+} bonding to a water. However, Bi doped framework showed the low ORR performance, further proving the exact active sites for ORR in the framework. This example also illustrates that in the crystalline porous material, the active site or the host-guest interaction can be precisely determined due to the well-fined structure.

Except the supertetrahedral cluster based metal chalcogenide frameworks, other metal chalcogenides materials were also synthesized. For example, Dehnen and co-workers synthesized a “zeoball” shaped polyanion with Sn-Ge-Se composition, showing the ability to trap I_2 molecuels with the subsequent I-I bond cleavage.[67] Mercouri G. Kanatzidis with co-workers also reported a series of layer structure for selectively trapping radioactive species from seawater.[68]

1.4 Contributions from This Work

The past several decades witnessed the rapid development of metal chalcogenide open frameworks, especially the frameworks based on the tetrahedral clusters. These semiconducting molecular clusters can be identified as the artificial tetrahedral atoms in zeolite type structures. Because of the tunable chemical composition and controllable size of these clusters, lots of new structures have emerged. However, exploring the structural feature with the aim to seek for the potential or practical applications is less developed. In this thesis, due to the high thermal and chemical stability and permanent porosity of T2 cluster based supersodalite type frameworks, they were selected as the platform to explore the potential applications of metal chalcogenide materials.

In Chapter 2, based on the bimetallic ternary CPM-120-ZnGeS-AEM, we explored the dramatic effect of tuning chemical composition on the crystallization process or the structural type. The result showed that valence and ionic diameters of the dopant metal cations were the key factor in the assembly of T2 clusters. Through tuning the chemical composition with different atomic ratio in T2 clusters, tunable band gaps have been successfully realized. These crystalline porous materials also show some promising properties. CO_2 uptake of CPM-120-ZnGaGeS-Cs at 298K is 4.32mmol cm^{-3} at 1 atm, comparable to some other ideal CO_2 adsorbents. The excellent photocatalytic hydrogen evolution performance reveals these synthesized porous semiconductors as promising photocatalysts. The studies here build a bridge between the molecular semiconducting clusters and the resulting frameworks, providing a systematic investigation on the structural retention and alternation of zeolitic porous chalcogenides.

One of the significant advantages of porous semiconductor over traditional solid-state semiconductors is its integration of porosity and semiconducting property. In chapter 3, the zeolitic porous chalcogenide, CPM-120-ZnGaGeS-Cs, is proved to function as the selective porous photocatalyst. In photocatalytic reaction, the more active sites the reactant can utilize, the higher efficiency the photocatalyst possess. Due to the anionic host framework, the charge-balanced species Cs^+ can be exchanged out by other cationic molecules. So the cationic model-Rhodamine B, can diffuse into the cavities of the material through cation exchange process, thus utilizing the active sites inside the pore to perform the photocatalysis. While for the anionic model, Methyl Orange (MO^-), the access into the cavities is denied due to the charge mismatch. As a result, only the active sites on the external surface of material can be used for photocatalytic reaction of anionic MO^-, resulting in the low photocatalytic rates. This study demonstrates a promising platform for the development of selective photocatalytic materials.

In addition, the Cs^+ in the channel of zeolitic porous chalcogenide can also be replaced by other alkali metal cations. In chapter 4, the intrinsic advantages of a special family of porous chalcogenides for CO_2 adsorption in terms of extraordinarily high selectivity, large uptake capacity, and robust structure due to the unique integration of the chalcogen-soft surface, high porosity, all-inorganic crystalline framework, and the tunable charge-to-volume ratio of exchangeable cations are well demonstrated. Particularly, K@RWY has the superior CO_2/N_2 selectivity with the N_2 adsorption even undetected at either 298 K or 273 K. It also has a large uptake capacity of 6.3 mmol/g (141 cm^3/g) of CO_2 at 273 K and 1 atm with an isosteric heat (35.0 - 41.1 kJ mol^{-1}).

The sulfur-rich nature of metal chalcogenide material provides an opportunity to develop other materials with high density of doped sulfur atoms. In Chapter 5, different carbon- and nitrogen-containing cationic molecules are introduced into sodalite cage through the cation exchange. The resulting materials can be transformed into heteroatom-doped carbon matrix through calcination and acid treatment. Among them, Fe, N, S doped carbon materials show the excellent ORR performance. The onsite potential in 0.1M KOH is comparable to 20% Pt/C and the half-wave potential is even more positive than that of 20% Pt/C. The robust metal chalcogenide framework not only provides a sulfur rich environment, but also provides a highly porous substrate. This work paves a new way to develop high-performance non-precious metal electrocatalysts for oxygen reduction based on the metal chalcogenide open framework.

1.5 Reference

(1) Corma, A.; Nemeth, L. T.; Renz, M.; Valencia, S. *Nature*, 2001, **412**, 423.

(2) Sumida, K.; Rogow, D. L.; Mason, J. A.; McDonald, T. M.; Bloch, E. D.; Herm, Z. R.; Bae, T.-H.; Long, J. R. *Chem. Rev.*, 2012, **112**, 724-781.

(3) Sherry, H. S.; Walton, H. F. *The Journal of Physical Chemistry*, 1967, **71**, 1457-1465.

(4) Shekhah, O.; Liu, J.; Fischer, R. A.; Wöll, C. *Chem. Soc. Rev.*, 2011, **40**, 1081-1106.

(5) Davis, M. E. *Nature*, 2002, **417**, 813.

(6) Li, Y.; Yu, J. *Chem. Rev.*, 2014, **114**, 7268-7316.

(7) Wei, Y.; Parmentier, T. E.; de Jong, K. P.; Zecevic, J. *Chem. Soc. Rev.*, 2015, **44**, 7234-7261.

(8) Verboekend, D.; Nuttens, N.; Locus, R.; Van Aelst, J.; Verolme, P.; Groen, J. C.; Perez-Ramirez, J.; Sels, B. F. *Chem. Soc. Rev.*, 2016, **45**, 3331-3352.

(9) Feng, P.; Bu, X.; Stucky, G. D. *Nature*, 1997, **388**, 735.

(10) Bu, X.; Feng, P.; Stucky, G. D. *Science*, 1997, **278**, 2080.

(11) Cheetham, A. K.; Férey, G.; Loiseau, T. *Angew. Chem. Int. Ed.*, 1999, **38**, 3268-3292.

(12) Cahill, C. L.; Parise, J. B. *J. Chem. Soc., Dalton Trans.*, 2000, 1475-1482.

(13) Bowes, C. L.; Ozin, G. A. *Adv. Mater.*, 1996, **8**, 13-28.

(14) Scott, R. W. J.; MacLachlan, M. J.; Ozin, G. A. *Curr. Opin. Solid State Mater. Sci.*, 1999, **4**, 113-121.

(15) El-Kaderi, H. M.; Hunt, J. R.; Mendoza-Cortés, J. L.; Côté, A. P.; Taylor, R. E.; Keeffe, M.; Yaghi, O. M. *Science*, 2007, **316**, 268.

(16) Côté, A. P.; Benin, A. I.; Ockwig, N. W.; Keeffe, M.; Matzger, A. J.; Yaghi, O. M. *Science*, 2005, **310**, 1166.

(17) Feng, X.; Ding, X.; Jiang, D. *Chem. Soc. Rev.*, 2012, **41**, 6010-6022.

(18) Li, H.; Eddaoudi, M.; O'Keeffe, M.; Yaghi, O. M. *Nature*, 1999, **402**, 276.

(19) Kreno, L. E.; Leong, K.; Farha, O. K.; Allendorf, M.; Van Duyne, R. P.; Hupp, J. T. *Chem. Rev.*, 2012, **112**, 1105-1125.

(20) Lee, J.; Farha, O. K.; Roberts, J.; Scheidt, K. A.; Nguyen, S. T.; Hupp, J. T. *Chem. Soc. Rev.*, 2009, **38**, 1450-1459.

(21) Inokuma, Y.; Yoshioka, S.; Ariyoshi, J.; Arai, T.; Hitora, Y.; Takada, K.; Matsunaga, S.; Rissanen, K.; Fujita, M. *Nature*, 2013, **495**, 461.

(22) Hayes, L. M.; Knapp, C. E.; Nathoo, K. Y.; Press, N. J.; Tocher, D. A.; Carmalt, C. J. *Crystal Growth & Design*, 2016, **16**, 3465-3472.

(23) Zhao, X.; Bu, X.; Wu, T.; Zheng, S.-T.; Wang, L.; Feng, P. *Nature Communications*, 2013, **4**, 2344.

(24) Sing, K. *Pure Appl. Chem.*, 1982, **54**, 2201-2218.

(25) Baerlocher, C.; McCusker, L. B.; Olson, D. H., *Atlas of zeolite framework types*, Elsevier, 2007.

(26) Brunner, G. *Zeolites*, 1990, **10**, 612-614.

(27) Long, R. Q.; Yang, R. T. *J. Am. Chem. Soc.*, 1999, **121**, 5595-5596.

(28) Iwamoto, M.; Yahiro, H.; Tanda, K.; Mizuno, N.; Mine, Y.; Kagawa, S. *The Journal of Physical Chemistry*, 1991, **95**, 3727-3730.

(29) Wilson, S. T.; Lok, B. M.; Messina, C. A.; Cannan, T. R.; Flanigen, E. M. *J. Am. Chem. Soc.*, 1982, **104**, 1146-1147.

(30) Bedard, R.; Wilson, S.; Vail, L.; Bennett, J.; Flanigen, E., in *Proceedings of the 8th International Zeolite Conference*, Elsevier: Amsterdam, 1989, p. 375.

(31) Bu, X.; Zheng, N.; Feng, P. *Chemistry – A European Journal*, 2004, **10**, 3356-3362.

(32) Feng, P.; Bu, X.; Zheng, N. *Acc. Chem. Res.*, 2005, **38**, 293-303.

(33) Zheng, N.; Bu, X.; Feng, P. *J. Am. Chem. Soc.*, 2003, **125**, 1138-1139.

(34) Bu, X.; Zheng, N.; Li, Y.; Feng, P. *J. Am. Chem. Soc.*, 2003, **125**, 6024-6025.

(35) Wang, L.; Wu, T.; Zuo, F.; Zhao, X.; Bu, X.; Wu, J.; Feng, P. *J. Am. Chem. Soc.*, 2010, **132**, 3283-3285.

(36) Wu, T.; Bu, X.; Zhao, X.; Khazhakyan, R.; Feng, P. *J. Am. Chem. Soc.*, 2011, **133**, 9616-9625.

(37) Nellis, D. M.; Ko, Y.; Tan, K.; Koch, S.; Parise, J. B. *J. Chem. Soc., Chem. Commun.*, 1995, 541-542.

(38) Krebs, B.; Voelker, D.; Stiller, K.-O. *Inorg. Chim. Acta*, 1982, **65**, L101-L102.

(39) Krebs, B.; Henkel, G. *Angewandte Chemie International Edition in English*, 1991, **30**, 769-788.

(40) Cahill, C. L.; Parise, J. B. *Chem. Mater.*, 1997, **9**, 807-811.

(41) Yaghi, O. M.; Sun, Z.; Richardson, D. A.; Groy, T. L. *J. Am. Chem. Soc.*, 1994, **116**, 807-808.

(42) Ahari, H.; Garcia, A.; Kirkby, S.; A. Ozin, G.; Young, D.; J. Lough, A. *J. Chem. Soc., Dalton Trans.*, 1998, 2023-2028.

(43) Bowes, C. L.; Lough, A. J.; Malek, A.; Ozin, G. A.; Petrov, S.; Young, D. *Chem. Ber.*, 1996, **129**, 283-287.

(44) MacLachlan, M. J.; Petrov, S.; Bedard, R. L.; Manners, I.; Ozin, G. A. *Angew. Chem. Int. Ed.*, 1998, **37**, 2075-2079.

(45) Zheng, N.; Bu, X.; Wang, B.; Feng, P. *Science*, 2002, **298**, 2366.

(46) Lin, Q.; Bu, X.; Mao, C.; Zhao, X.; Sasan, K.; Feng, P. *J. Am. Chem. Soc.*, 2015, **137**, 6184-6187.

(47) Cahill, C. L.; Ko, Y.; Hanson, J. C.; Tan, K.; Parise, J. B. *Chem. Mater.*, 1998, **10**, 1453-1458.

(48) Parise, J. B.; Ko, Y. *Chem. Mater.*, 1994, **6**, 718-720.

(49) Lin, Q.; Bu, X.; Feng, P. *Chem. Commun.*, 2014, **50**, 4044-4046.

(50) Cahill, C. L.; Ko, Y.; Parise, J. B. *Chem. Mater.*, 1998, **10**, 19-21.

(51) Li, H.; Eddaoudi, M.; Laine, A.; O'Keeffe, M.; Yaghi, O. M. *J. Am. Chem. Soc.*, 1999, **121**, 6096-6097.

(52) Li, H.; Laine, A.; Keeffe, M.; Yaghi, O. M. *Science*, 1999, **283**, 1145.

(53) Bu, X.; Zheng, N.; Wang, X.; Wang, B.; Feng, P. *Angew. Chem. Int. Ed.*, 2004, **43**, 1502-1505.

(54) Wang, C.; Bu, X.; Zheng, N.; Feng, P. *Chem. Commun.*, 2002, 1344-1345.

(55) Li, H.; Kim, J.; Groy, T. L.; O'Keeffe, M.; Yaghi, O. M. *J. Am. Chem. Soc.*, 2001, **123**, 4867-4868.

(56) Wang, C.; Bu, X.; Zheng, N.; Feng, P. *J. Am. Chem. Soc.*, 2002, **124**, 10268-10269.

(57) Su, W.; Huang, X.; Li, J.; Fu, H. *J. Am. Chem. Soc.*, 2002, **124**, 12944-12945.

(58) Bu, X.; Zheng, N.; Li, Y.; Feng, P. *J. Am. Chem. Soc.*, 2002, **124**, 12646-12647.

(59) Wu, T.; Bu, X.; Liao, P.; Wang, L.; Zheng, S.-T.; Ma, R.; Feng, P. *J. Am. Chem. Soc.*, 2012, **134**, 3619-3622.

(60) Xiong, W.-W.; Li, J.-R.; Hu, B.; Tan, B.; Li, R.-F.; Huang, X.-Y. *Chemical Science*, 2012, **3**, 1200-1204.

(61) Wu, T.; Wang, X.; Bu, X.; Zhao, X.; Wang, L.; Feng, P. *Angew. Chem. Int. Ed.*, 2009, **48**, 7204-7207.

(62) Yang, H.; Luo, M.; Luo, L.; Wang, H.; Hu, D.; Lin, J.; Wang, X.; Wang, Y.; Wang, S.; Bu, X.; Feng, P.; Wu, T. *Chem. Mater.*, 2016, **28**, 8774-8780.

(63) Zhang, X.-M.; Sarma, D.; Wu, Y.-Q.; Wang, L.; Ning, Z.-X.; Zhang, F.-Q.; Kanatzidis, M. G. *J. Am. Chem. Soc.*, 2016, **138**, 5543-5546.

(64) Zheng, N.; Bu, X.; Feng, P. *Nature*, 2003, **426**, 428.

(65) Zheng, N.; Bu, X.; Vu, H.; Feng, P. *Angew. Chem. Int. Ed.*, 2005, **44**, 5299-5303.

(66) Lin, J.; Dong, Y.; Zhang, Q.; Hu, D.; Li, N.; Wang, L.; Liu, Y.; Wu, T. *Angew. Chem. Int. Ed.*, 2015, **54**, 5103-5107.

(67) Lin, Y.; Massa, W.; Dehnen, S. *J. Am. Chem. Soc.*, 2012, **134**, 4497-4500.

(68) Feng, M.-L.; Sarma, D.; Qi, X.-H.; Du, K.-Z.; Huang, X.-Y.; Kanatzidis, M. G. *J. Am. Chem. Soc.*, 2016, **138**, 12578-12585.

Chapter 2 Doping in Zeolitic Porous Chalcogenide

2.1 Introduction

Metal chalcogenides have received lots of attention during the past two decades due to their promising optic or electric properties by integrating porosity and semiconductivity.[1-20] Among these materials, supertetrahedral T*n* cluster, which is actually the tetrahedrally shaped fragments of zinc blend lattice, is a common building block for constructing porous frameworks.[21-29] As a well-defined molecular cluster, these small semiconducting building units can assemble into three-dimensional superlattice by sharing the corner chalcogen atom, thus building a bridge between semiconducting nanoclusters and covalent superlattices.[30, 31]

Tuning the chemical composition on nanoclusters has been devoted to synthesizing chalcogenides with new structures for a long time. Employing metal cations with different valences is one of the most widely used methods to broaden the family member of this material. Binary, such as M_2^{3+}/X^{2-}, and ternary, such as $M_1^{4+}/M_2^{3+}/X^{2-}$, $M_1^{4+}/M_3^{2+}/X^{2-}$, $M_2^{3+}/M_3^{2+}/X^{2-}$ and $M_1^{3+}/M_4^{+}/X^{2-}$ (M_1^{4+}= Ge^{4+} or Sn^{4+}; M_2^{3+}= Ga^{3+} or In^{3+}; M_2^{2+}= Zn^{2+}, Cd^{2+}, Mn^{2+}, Co^{2+} or Fe^{2+}; M_4^{+}= Cu^{+} and X^{2-}= S^{2-} or Se^{2-}) open framework chalcogenides have been well researched. Recently, quaternary chalcogenide with $M_1^{4+}/M_2^{3+}/M_3^{2+}/X^{2-}$ composition has been synthesized, such as covalently bonding T4 cluster based OCF-5 and isolated T4 cluster based OCF-40.[32, 33] In these large clusters, the positions of different metal cations are not interchangeable in these quaternary clusters due to the local charge matching. For example, in OCF-40-ZnGaSnSe, tin is located at corner sites and zinc is bonded to the core sulfur site, while gallium occupy the corner, edge and face sites. It is also worth noting that when built of T4 and T5 cluster, most of the structures are single or double diamond type, possibly because of the rigid M-X-M angle (105° ~115°) and the favorable phases of single or double diamond type structure from the thermodynamic perspective.

Because of high chemical and thermal stability, the zeotype frameworks can exhibit promising optic or electric properties with long durability,[34-36] which need to be paid more attention. If the size of the cluster is controlled to T2 and T3, various kinds of zeotype structures can be obtained. For example, sodalite and CrB_4 topology can be realized in $M^{4+}/M^{3+}/X^{2-}$ and $M^{4+}/M^{2+}/X^{2-}$ (M^{4+}=Ge^{4+} and Sn^{4+}, M^{3+}=Ga^{3+} and In^{3+}, M^{2+}=Zn^{2+} and Cd^{2+}, X^{2-}= S^{2-} and Se^{2-}) T2 and M^{3+}/S^{2-} (M3+=In^{3+} and Ga^{3+}) T3 cluster.[9, 37] Recently, even an interrupted In-Se based T2 cluster (3-conneted and 4 connected supertetrahedral clusters) can form a zeolite analogue.[38]

Compared with T3 cluster made of only trivalent metal cations, the chemical composition of T2 clusters can be variable and is worth studying. In the existing T2 cluster, only bimetallic ternary chalcogenide clusters exist ($M^{4+}/M^{3+}/X^{2-}$ and $M^{4+}/ M^{2+}/X^{2-}$). Modification on the chemical composition of cluster can change not only the resulting covalent superlattices, but also the optic or electric properties. As mentioned above, quaternary supertetrahedral cluster only exists in T4 clusters, just resulting in diamond type superlattices. Other quaternary chemical compositions of chalcogenide cluster, especially in the zeolitic porous chalcogenides, have not been well explored yet.

Although quaternary supertetrahedral clusters with metal cations of different valences exist, there are almost no quaternary supertetrahedral clusters with different metal cations of the same valence. In $M_1^{4+}/M_2^{3+}/M_3^{2+}/X^{2-}$ quaternary T4 cluster, metal cations with different valences can be distributed in different sites of the same cluster due to the local charge matching. If a quaternary supertetrahedral cluster is made of different metal cations among which at least two kinds possess the same valence, those metal cations will be located in the equivalent sites of the cluster. This situation will lead to the difficulty in crystallizing process due to the large difference of radius between different metal cations, such as Ge^{4+} and Sn^{4+}, or Zn^{2+} and Cd^{2+}. However, if realized, this will make us have a further understanding of these well-defined nanoclusters. In addition, broadening the family member of quaternary supertetrhedral cluster is also an effective method for band gap engineering.

In this study, we adopt a series of highly stable chalcogenides with tunable structures, electronic and optic properties by controlling the chemical compositions based on a bimetallic zeolitic porous chalcogenide built of T2 cluster (Scheme 2.1). We introduce four new quaternary T2 cluster – $Zn^{2+}/Ga^{3+}/Ge^{4+}/S^{2-}$, $Zn^{2+}/In^{3+}/Ge^{4+}/S^{2-}$, $Zn^{2+}/Ge^{4+}/Sn^{4+}/S^{2-}$ and $Zn^{2+}/Cd^{2+}/Ge^{4+}/S^{2-}$ by doping a ternary T2 cluster with a third metal cation. Here, modifying the chemical composition can result in two effects: optimization of crystallization process and alternation of the phase. The size and morphology of the crystals can be modulated with the help of gallium due to the charge and radius matching. The introduction of metal cations with radius mismatching would induce the structure to transform from super-sodalite to super-diamond type. Both of these studies - improving the crystallization or changing the phase - are controlled through the modification of nanoclusters and have been rarely reported in crystalline porous chalcogenide. Those materials with different chemical compostions show the tunable band gap, gas adsorption and photocatalytic hydrogen evolution properties. In the following part, the super-sodalite type structures based on supertetrahedral T2 cluster are collected as CPM-120 and super-diamond type structures based on supertetrahedral T2 cluster are collected as CPM-121, if there is no special denotation.

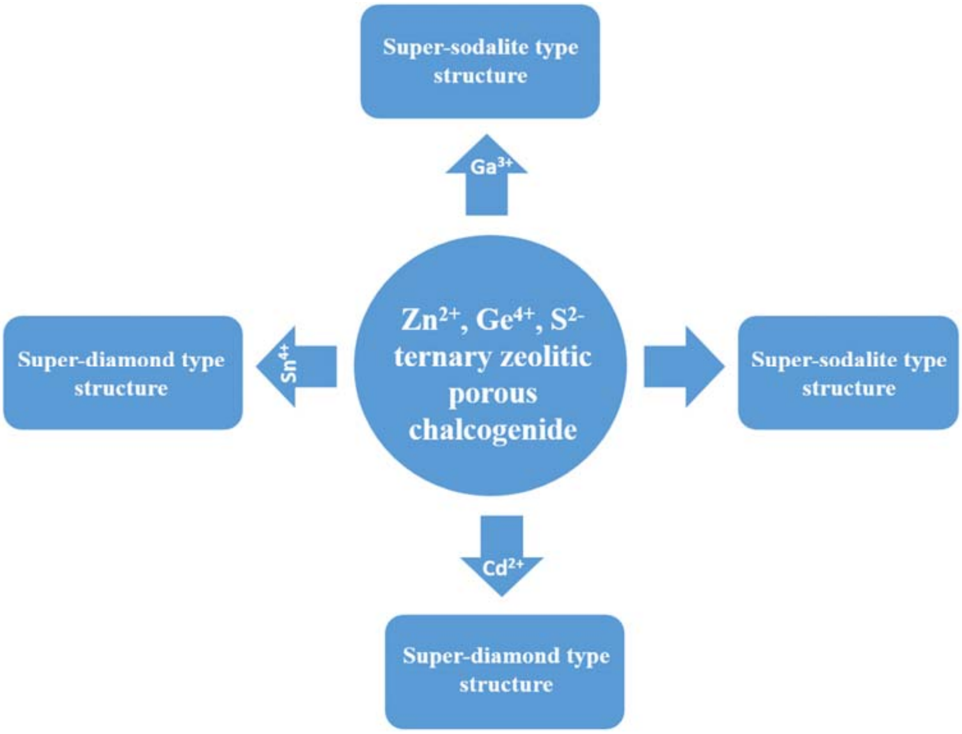

Scheme 2.1 Illustration of the effects of modification of the chemical composition of chalcogenide supertetrahedral T2 nanocluster on the as-synthesized frameworks.

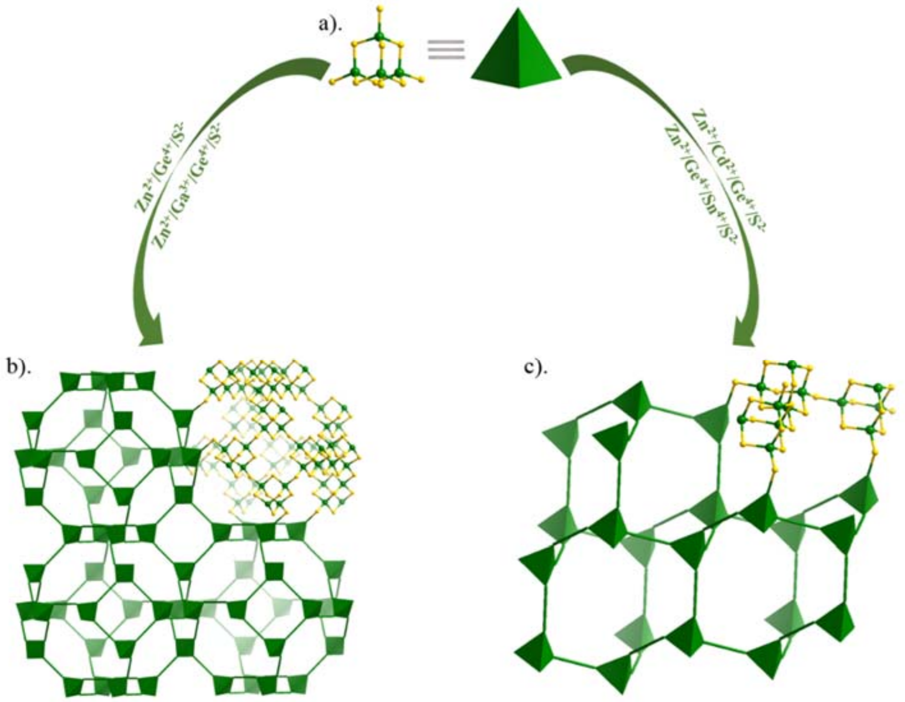

Figure 2.1 Chalcogenide supertetrahedral T2 cluster (a) self-assemble into super-sodalite type structure (b) and super-diamond type structure (c) through different chemical composition. Green balls represent tetravalent germanium and tin cations, trivalent gallium cations and divalent zinc and cadmium cations. Yellow balls represent sulfur anions.

2.2 Experimental Section

2.2.1 Chemicals and General Methods

All chemicals and solvents used in these synthetic studies were commercially available and used as purchased without further purification. Germanium dioxide (GeO_2, 99.999%), gallium nitrate hydrate ($Ga(NO_3)_3 \cdot xH_2O$, 99.9998%), tin(IV) oxide (SnO_2, 99.9%) and zinc nitrate hexahydrate ($Zn(NO_3)_2 \cdot 6H_2O$, 98%) were purchased from Acros. Cadmium nitrate tetrahydrate ($Cd(NO_3)_2 \cdot 4H_2O$, 98.5%), N-(2-aminoethyl)-morpholine

(AEM, 98%+) and sulfur powder (S, 100mesh, 99.5%) was purchased from Alfa Aesar. Powder X-ray Diffraction (PXRD) data were performed a Bruker D8 Advance powder diffraction meter with CuKα radiation (40 kV, 40 mA, λ = 1.5418 Å). The simulated powder patterns were calculated using single-crystal X-ray diffraction data of CPM-120-ZnGeS and CPM-121-ZnGeS processed by the Mercury 2.3 program provided by the Cambridge Crystallographic Data Centre, respectively. Solid-state diffuse reflectance spectra were recorded on Shimadzu UV-3101PC spectrophotometer using $BaSO_4$ powder as 100% reflectance reference. The adsorption spectra were calculated from reflectance spectra by using the Kubelka-Munk function. Scanning electron microscopy (SEM) images and energy dispersive spectroscopy (EDS) data were carried out on Philips FEI XL30 field emission scanning electron microscope (FESEM) equipped with PGT-IMIX PTS EDS detector, or on Nova Nano-SEM450 (Schottky field emission scanning electron microscope) integrated with EDS allowing to perform qualitative and quantitative chemical analysis and image capture. EDS data acquisition was performed with an accelerating voltage of 20 kV and 60 s accumulation time. Microscopic images were performed on Leica MZIII Pursuit. Gas sorption isotherms were measured on a Micromeritics ASAP 2020 surface-area and pore-size analyzer up to 1 atm of gas pressure by the static volumetric method. All gases used were of 99.99% purity, and the impurity trace water was removed by passing the gases through the molecular sieve column equipped in the gas line. The gas sorption isotherms for N_2 were measured at 77 K. The gas sorption isotherms of CO_2 were measure at 273K and 298K. The gas sorption isotherms of CH_4 and C_2H_2 were measure at 273K.The sample was degassed at 100 °C overnight before measurement.

2.2.2 Synthetic Methods

Synthesis of CPM-120-ZnGaGeS-AEM with improved morphology

CPM-120-ZnGeS-AEM was first synthesized according to our previous report. In details, 125mg GeO_2 (1.20mmol), 90mg $Zn(NO_3)_2 \cdot 6H_2O$ (0.30mmol), 260mg S (8.125mmol) and 3.0mL AEM were mixed thoroughly in a 23mL Teflon-lined stainless autoclave and stirred for 1 hour. After heating the sealed reaction mixture at 190 °C for 12 days, around 150mg of large block crystals with trace amount of small pale yellow rhombic-dodecahedral crystals were obtained. The powder impurities can be washed away using methanol. The pure crystals were obtained by filtering and washing with extra methanol. In order to improve the morphology and repeatability, $Ga(NO_3)_3 \cdot xH_2O$ was employed here. Specifically, 25, 51, 77, 102, 117 and 127mg $Ga(NO_3)_3 \cdot xH_2O$ were added to different autoclaves to explore the morphology change. Here, when 117mg of $Ga(NO_3)_3 \cdot xH_2O$ was added to the reaction pot, small pale yellow rhombic-dodecahedral crystals can be obtained without other shapes of crystals. Continue adding $Ga(NO_3)_3 \cdot xH_2O$ to the reaction pot can lead to tiny crystals or crystalline powder and bad repeatability. Through exploration of synthetic methods, the phase purity was supported by Powder x-ray diffraction (PXRD). The presence and ratio of Zn/Ga/Ge/S were confirmed by energy-dispersive-X-ray (EDX) spectroscopy.

Table 2.1 Summary of exploration for synthesis of Ga-doped CPM-120-ZnGeS-AEM with enhance morphology.

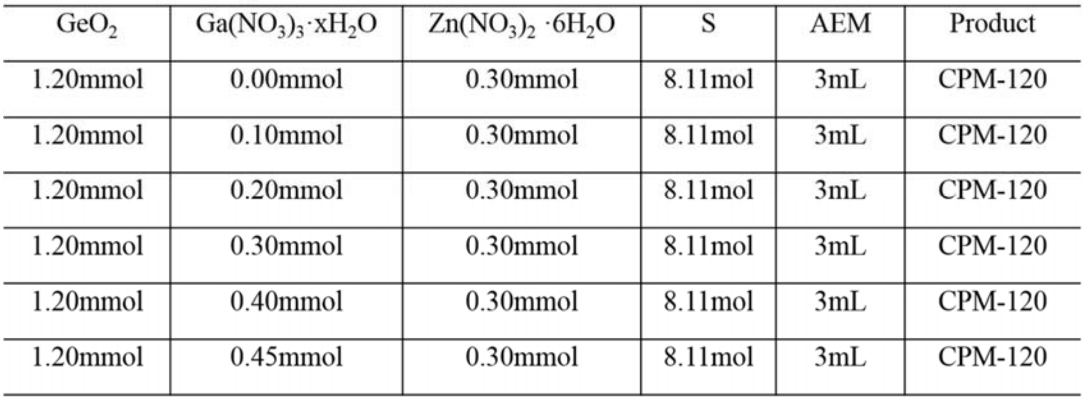

GeO_2	$Ga(NO_3)_3 \cdot xH_2O$	$Zn(NO_3)_2 \cdot 6H_2O$	S	AEM	Product
1.20mmol	0.00mmol	0.30mmol	8.11mol	3mL	CPM-120
1.20mmol	0.10mmol	0.30mmol	8.11mol	3mL	CPM-120
1.20mmol	0.20mmol	0.30mmol	8.11mol	3mL	CPM-120
1.20mmol	0.30mmol	0.30mmol	8.11mol	3mL	CPM-120
1.20mmol	0.40mmol	0.30mmol	8.11mol	3mL	CPM-120
1.20mmol	0.45mmol	0.30mmol	8.11mol	3mL	CPM-120

Synthesis of CPM-121-ZnGeSnS-AEM

The pure phase of CPM-121-ZnGeSnS-AEM with diamond type structure can be obtained by a fixed molar ratio of GeO_2 and SnO_2. Otherwise, the mixture of sodalite type and diamond type compounds would be obtained. In order to synthesize the pure diamond type compound, two methods were employed. The phase purity can be supported by Powder x-ray diffraction (PXRD). The presence and ratio of Zn/Ge/Sn/S were confirmed by energy-dispersive-X-ray (EDX) spectroscopy.

Method I: 1.20 mmol GeO_2, 0.30 mmol $Zn(NO_3)_2 \cdot 6H_2O$, 260mg S and 3mL AEM were fixed amounts and added to the 23mL Teflon-lined stainless autoclave, various amount of SnO_2 powder were added (0.12mmol, 0.24mmol, 0.36mmol, 0.48mmol, 0.60mmol, 0.72mmol, 0.84mmol, 0. 96mmol, 1.08mmol and 1.20mmol). After mixed thoroughly and stirring for 1 hour, the sealed autoclaves were heated at 190 °C for 12 days. The impurity powders can be washed away using methanol. The pure crystalline powder were obtained by filtering and washing with extra methanol. The phase purity can be conformed through the comparison of PXRD pattern with simulated one. Among them, the pure phase of CPM-121-ZnGeSnS can be obtained when added 0.24mmol tin precursor, with most of others are the mixture of sodalite and diamond type compounds.

Table 2.2 Summary of exploration for synthesis of Sn-doped T2 based chalcogenide framework based on CPM-120-ZnGeS-AEM through *Method I*, as mentioned below.

Code#	GeO_2	SnO_2	$Zn(NO_3)_2 \cdot 6H_2O$	S	AEM	Product
3-1	1.20mmol	0.12mmol	0.30mmol	8.11mol	3mL	Mixture of CPM-120 and CPM-121
3-2	1.20mmol	0.24mmol	0.30mmol	8.11mol	3mL	CPM-121
3-3	1.20mmol	0.36mmol	0.30mmol	8.11mol	3mL	Mixture of CPM-120 and CPM-121
3-4	1.20mmol	0.48mmol	0.30mmol	8.11mol	3mL	Mixture of CPM-120 and CPM-121
3-5	1.20mmol	0.60mmol	0.30mmol	8.11mol	3mL	Mixture of CPM-120 and CPM-121
3-6	1.20mmol	0.72mmol	0.30mmol	8.11mol	3mL	Mixture of CPM-120 and CPM-121
3-7	1.20mmol	0.84mmol	0.30mmol	8.11mol	3mL	Mixture of CPM-120 and CPM-121
3-8	1.20mmol	0.96mmol	0.30mmol	8.11mol	3mL	Mixture of CPM-120 and CPM-121
3-9	1.20mmol	1.08mmol	0.30mmol	8.11mol	3mL	Mixture of CPM-120 and CPM-121
3-10	1.20mmol	1.20mmol	0.30mmol	8.11mol	3mL	Mixture of CPM-120 and CPM-121

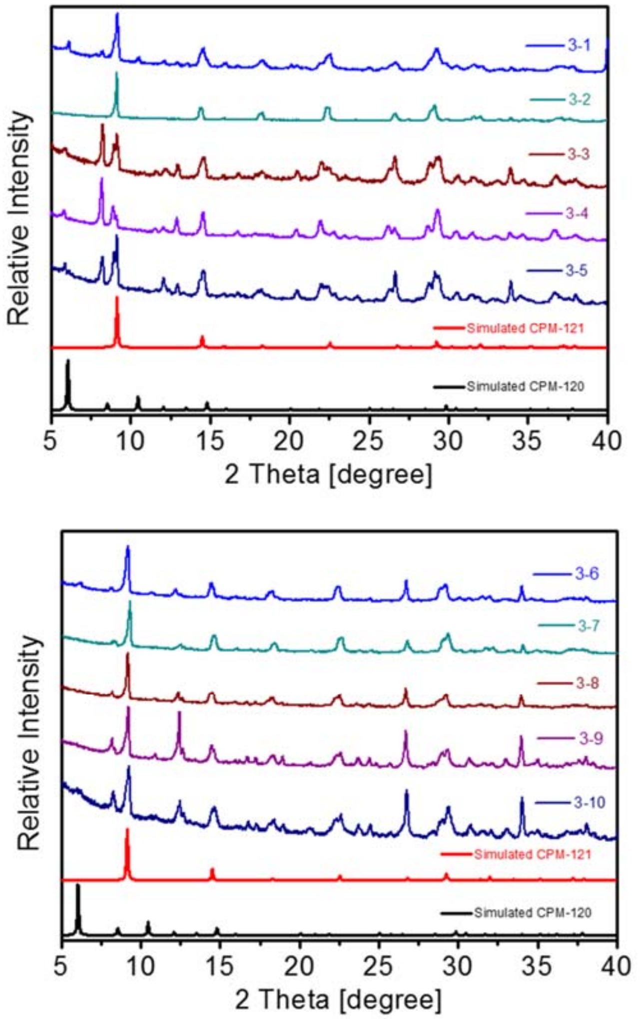

Figure 2.2 PXRD patterns of the as-synthesized product for synthesis of Sn-doped T2 based chalcogenide framework based on CPM-120-ZnGeS-AEM through *method I*. The code number adopted here is the same as those in Table 2.2.

Method II: The total molar amount of GeO_2 and SnO_2 was fixed and that is 1.20mmol. The molar ratio of GeO_2 to SnO_2 changed from 9:1 to 1:9. (These are 9:1, 8:2, 7:3, 6:4, 5:5, 4:6, 3:7, 2:8 and 1:9, respectively). The amount of other precursor remained the same as before, and those are 0.30 mmol $Zn(NO_3)_2 \cdot 6H_2O$, 260mg S and 3mL AEM. After mixing them in 23mL Teflon-lined stainless autoclaves by stirring for 1 hour, the autoclaves was heated in a 190 °C oven for 12 days. The impurity powders in the autoclaves can be washed away using methanol. The pure crystalline powder were obtained by filtering and washing with extra methanol. The phase purity can be conformed through the comparison of PXRD pattern with simulated one. Among them, the pure phase of CPM-121-ZnGeSnS can be obtained when the ratio of GeO_2: SnO_2 is 9:1, with most of others are the mixture of sodalite and diamond type compounds.

Table 2.3 Summary of exploration for synthesis of Sn-doped T2 based chalcogenide framework based on CPM-120-ZnGeS-AEM through *Method II* as mentioned below.

Code#	GeO_2	SnO_2	$Zn(NO_3)_2 \cdot 6H_2O$	S	AEM	Product
4-1	1.08mmol	0.12mmol	0.30mmol	8.11mol	3mL	CPM-121
4-2	0.96mmol	0.24mmol	0.30mmol	8.11mol	3mL	Mixture of CPM-120 and CPM-121
4-3	0.84mmol	0.36mmol	0.30mmol	8.11mol	3mL	Mixture of CPM-120 and CPM-121
4-4	0.72mmol	0.48mmol	0.30mmol	8.11mol	3mL	Mixture of CPM-120 and CPM-121
4-5	0.60mmol	0.60mmol	0.30mmol	8.11mol	3mL	Mixture of CPM-120 and CPM-121
4-6	0.48mmol	0.72mmol	0.30mmol	8.11mol	3mL	Impure CPM-121
4-7	0.36mmol	0.84mmol	0.30mmol	8.11mol	3mL	Impure CPM-121
4-8	0.24mmol	0.96mmol	0.30mmol	8.11mol	3mL	Impure CPM-121
4-9	0.12mmol	1.08mmol	0.30mmol	8.11mol	3mL	Impure CPM-121
4-10	0.00mmol	1.20mmol	0.30mmol	8.11mol	3mL	Unknown

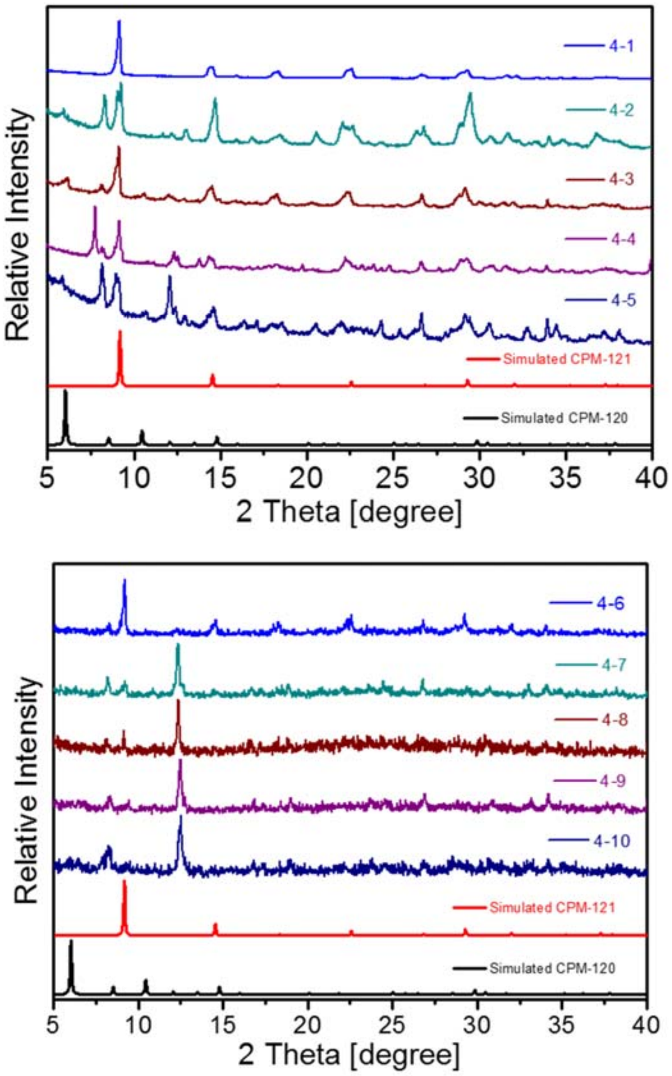

Figure 2.3 PXRD patterns of the as-synthesized product for synthesis of Sn-doped T2 based chalcogenide framework based on CPM-120-ZnGeS-AEM through *method II*. The code number adopted here is the same as those in Table 2.3.

Synthesis of CPM-121-ZnCdGeS-AEM

125mg GeO_2 (1.20mmol), 50mg $Zn(NO_3)_2 \cdot 6H_2O$ (0.17mmol), 40mg $Cd(NO_3) \cdot 4H_2O$ (0.13mmol), 200mg-220mg S (6.25 to 8.125mmol) and 3.0mL AEM were mixed thoroughly in a 23mL Teflon-lined stainless autoclave and stirred for 1 hour. After heating the sealed reaction mixture at 190 °C for 12 days, the colorless tiny octahedral shaped crystals (but not suitable for single crystal X-ray analysis) can be obtained by washing away impurities using methanol. The phase purity was supported by Powder x-ray diffraction (PXRD). The presence and ratio of Zn/Cd/Ge/S were confirmed by EDX spectroscopy.

Photocatalytic hydrogen production

The experiments were performed in a closed gas circulation system. Typically, 50mg of the sample was added to 120mL Na_2S-Na_2SO_3 (0.25M-0.1M) aqueous solutions with stirring. After degassing the whole system for 1 hour, a 300W Xe lamp was applied to the reaction container through the quartz plate. The produced gas was introduced by the carrier gas (Argon) to and analyzed by the gas chromatography instrument (Shimadzu GC-8A) equipped with a thermal conductivity detector (TCD).

2.3 Results and Discussion

2.3.1 First Trimetallic Zeolitic Porous Chalcogenide

The large block-shaped crystals of CPM-120-ZnGeS-AEM can be synthesized under solvothermal reaction of GeO_2, $Zn(NO_3)_2 \cdot 6H_2O$ and S in AEM, as reported previously. CPM-120-ZnGeS-AEM is made of T2 clusters, each of which shares the corner sulfur atom, joining together to give three-dimensional super-sodalite type structure (Figure 2.1b). The atomic ratio between Zn^{2+} and Ge^{4+} is 1.21:2.79, as determined by SEM-EDS and ICP-OES. There is no “precise” morphology for the description of the shapes of the crystal.

Only a small amount of dodecahedron shaped crystals can be observed under optical microscope. Here, it is worth noting that germanium and zinc occupy the equivalent position in T2 cluster.

The irregular shapes of the crystals may be attributed to the distinctively different charges between tetravalent germanium cations and divalent zinc cations. According to the Pauling's electrostatic valence rule, the valence of the anion should be exactly or nearly equal to the sum of the electrostatic bond strength to it from the cations surrounding it. In this case, the bi-coordinated negative-charged sulfur atoms in the framework are charge-balanced by the metal cations surrounding them, which is zinc and germanium. From this perspective, the positive charge of each metal cations contributed to the adjacent sulfur is not equivalent. This would lead to the different M-S bonds. Moreover, the total valence of +1.5 contributed from germanium and zinc could be too low for the S^{2-}. These possible factors may have some effects on the uniform crystallization of the crystal.

In order to optimize the crystallization and improve the morphology, a possible way is to minimize the charge difference. Following this guideline, gallium stands out as the common valence of its cation is trivalent, building a bridge between tetravalent germanium and divalent zinc. After doped with gallium, the super-sodalite type structure based on $[Zn_{0.76}Ga_{0.70}Ge_{2.54}]^{2.22-}$ T2 cluster with rhombic-dodecahedral morphology can be obtained.

It is also worth mentioning that this is the first case of trimetallic zeolitic porous chalcogenide. This is also the first example in open framework chalcogenide that tetravalent, trivalent and divalent metal cations exist in the same supertetrahedral cluster and occupy equivalent positions. Although previous reports show some structures formed by metal cations of these three valences, their positions in the clusters cannot be changed due to the local charge density matching, as mentioned above. This is because the tetra-coordinated sulfur anion in the core position of T4 cluster cannot bond to tetravalent cation, otherwise it will obey local charge matching. However, in T2 cluster, the bi-coordinate sulfur anion can bond to divalent, trivalent or tetravalent metal cations, thus providing a general platform to tune the optic or electronic properties of as-synthesized products and study the doping effect.

2.3.2 Optimization of Crystallization Process

Several batches of experiments with different gallium amounts were performed to explore the best ratio for the ideal crystallization process. The experimental details and atomic ratio in the as-synthesized product are summarized in Table 2.1. $Ga(NO_3)_3 \cdot xH_2O$ was chosen as the gallium source due to two considerations: 1). the soluble salt can be easily dissolved through the reaction pot, further helping the uniform crystallization process; 2). Instead of using gallium metal, there is no need for the redox reaction to occur in order to form trivalent gallium cations as the original valence from the precursor is already trivalent, minimizing the possibility of synthesis of by-products.

Indeed, increasing the amount of gallium precursor would help to improve the morphology of the crystal, transiting from irregular block shape to regular rhombic-dodecahedron shape, with a large extent. PXRD patterns of all of the crystals from all batches matched well with the simulated pattern of super-sodalite type CPM-120 (Figure 2.4). The SEM pictures and optical images in Figure 2.5 of the CPM-120 samples show a development from large irregular crystals to rhombic-dodecahedron-shaped crystals with increasing gallium amount. It clearly shows the outline of rhombic-dodecahedron pattern for almost all of the crystals when the adding amount increased to 0.30 mmol. Continuing increasing the adding amount of gallium can further improve the morphology with a large extent. When the adding amount reached 0.45 mmol, the transparent pale yellow rhombic-dodecahedron-shaped crystals with distinct edges can be obtained (Here, the crystal synthesized with 0.45 mmol Ga^{3+} added is denoted as CPM-120-ZnGaGeS-AEM). Continuing increasing the amount can only produce the crystalline powder. The uniform dodecahedron-shaped crystal CPM-120-ZnGaGeS-AEM can be successfully obtained from almost all of the autoclaves.

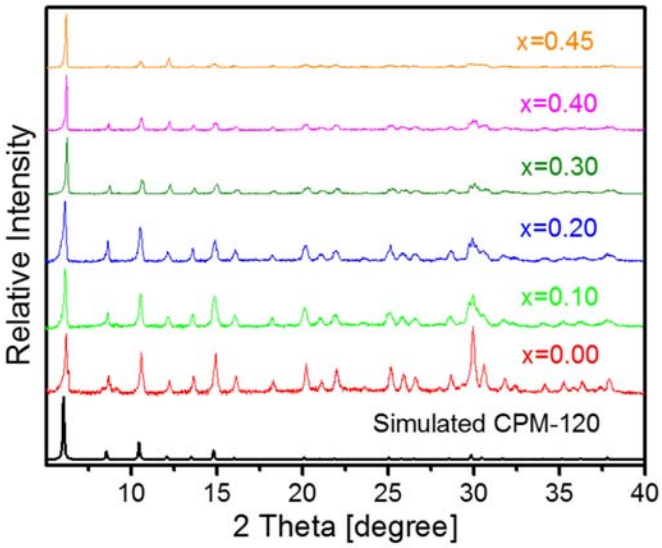

Figure 2.4 PXRD patterns of as-synthesized CPM-120 with different amounts of Ga^{3+} as the precursor. X represents the amount of Ga^{3+} added to the reaction.

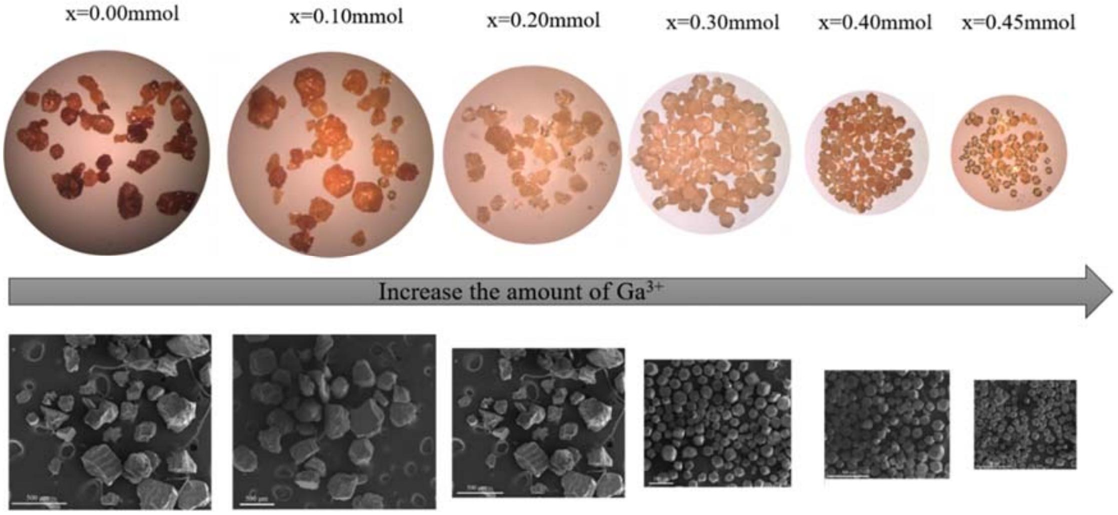

Figure 2.5 Optical (top) and SEM (bottom) images of crystals synthesized from different amounts of Ga^{3+} precursors. X here represents the amount of Ga^{3+} precursor.

As CPM-120 can be obtained when different amounts of gallium were added, it is interesting to study the atomic ratio of Ge^{4+}, Ga^{3+} and Zn^{2+} of the crystals synthesized from different batches. The atomic ratio of Zn^{2+}, Ga^{3+} and Ge^{4+} in the framework was summarized in Table 2.4. In CPM-120-ZnGeS-AEM, the ratio of Zn^{2+} to Ge^{4+} is 1.21:2.79. Addition of 0.10mmol Ga^{3+} salts as the precursor can lead the atomic ratio of Zn^{2+}:Ga^{3+}:Ge^{4+} to 1.21:0.24:2.55. It seems that such a small amount of Ga^{3+} can mainly lead to the replacement of the position of Ge^{4+}. In CPM-120-ZnGeS-AEM, the T2 cluster is $[Zn_{1.21}Ge_{2.79}S_8]^{2.42-}$, indicating that there are 2.18 protonated AEM cations surrounding around each T2 cluster. However, when 0.10 mmol Ga^{3+} were added as the precursor, the chemical composition of formed T2 cluster in the as-synthesized product is $[Zn_{1.21}Ga_{0.24}Ge_{2.55}S_8]^{2.66-}$, meaning that it needs more protonated AEM molecules as the charge-balancing species filling in the cages of the framework. Possibly the driving force for the replacement of Ge^{4+}, rather than Zn^{2+}, by Ga^{3+} is the spare spaces in the cages which can be filled by more protonated AEM molecules. However, continuing increasing the amount of gallium would replace mainly zinc cations, leading to the formed T2 cluster less negative. Finally, the chemical composition of T2 cluster is $[Zn_{0.76}Ga_{0.70}Ge_{2.54}]^{2.22-}$ when the adding amount of gallium reaches 0.45mmol. Perhaps the fact that gallium mainly replace the position of zinc is because less negative cluster can form the stable framework.

Table 2.4 Experimental details for the exploration of Ga-doped CPM-120-ZnGeS with structure type, atomic ratio, chemical composition and band gap for the as-synthesized product.

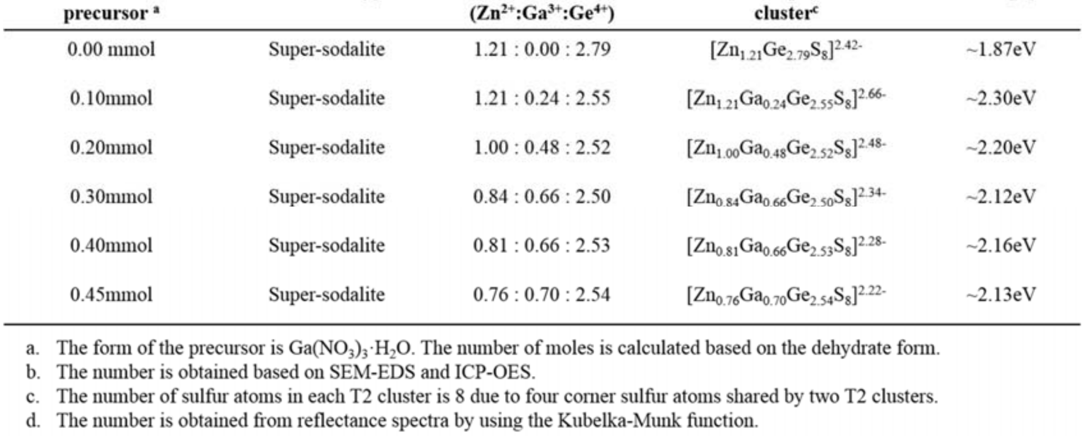

Amount of Ga^{3+} precursor [a]	Structural type	Atomic ratio[b] (Zn^{2+}:Ga^{3+}:Ge^{4+})	Chemical composition of T2 cluster[c]	Band gap[d]
0.00 mmol	Super-sodalite	1.21 : 0.00 : 2.79	$[Zn_{1.21}Ge_{2.79}S_8]^{2.42-}$	~1.87eV
0.10mmol	Super-sodalite	1.21 : 0.24 : 2.55	$[Zn_{1.21}Ga_{0.24}Ge_{2.55}S_8]^{2.66-}$	~2.30eV
0.20mmol	Super-sodalite	1.00 : 0.48 : 2.52	$[Zn_{1.00}Ga_{0.48}Ge_{2.52}S_8]^{2.48-}$	~2.20eV
0.30mmol	Super-sodalite	0.84 : 0.66 : 2.50	$[Zn_{0.84}Ga_{0.66}Ge_{2.50}S_8]^{2.34-}$	~2.12eV
0.40mmol	Super-sodalite	0.81 : 0.66 : 2.53	$[Zn_{0.81}Ga_{0.66}Ge_{2.53}S_8]^{2.28-}$	~2.16eV
0.45mmol	Super-sodalite	0.76 : 0.70 : 2.54	$[Zn_{0.76}Ga_{0.70}Ge_{2.54}S_8]^{2.22-}$	~2.13eV

a. The form of the precursor is $Ga(NO_3)_3 \cdot H_2O$. The number of moles is calculated based on the dehydrate form.
b. The number is obtained based on SEM-EDS and ICP-OES.
c. The number of sulfur atoms in each T2 cluster is 8 due to four corner sulfur atoms shared by two T2 clusters.
d. The number is obtained from reflectance spectra by using the Kubelka-Munk function.

2.3.3 Effects of gallium and indium on the crystallization process

Besides the reason of the charge, another possible reason for uniform crystallization is the closed radius of these three metal cations. The reason for choosing trivalent gallium, rather than trivalent indium, is its ionic radius, which is closed to these of Zn^{2+} and Ge^{4+}. Otherwise the large radius difference may not be able to allow uniform crystallization due to different M-S bond lengths.

In super-sodalite structured CPM-120 consisting of T2 clusters, all of the metal positions are crystallographically equivalent. The M-S bond should be the same. If doped with indium, although building a bridge between tetravalent germanium and divalent zinc, the large radius difference make them hard to occupy the equivalent positions in the superlattices.

In order to prove this, indium salts was added to the reaction batches. The experimental details are similar to the gallium case. As the above estimation, neither of the batches can result in pure or uniform CPM-120 crystals. However, when the amount of indium precursor reaches 0.30mmol, pure super-diamond type structure (CPM-121) can be obtained by matching the PXRD with the simulated one. (Figure 2.6)

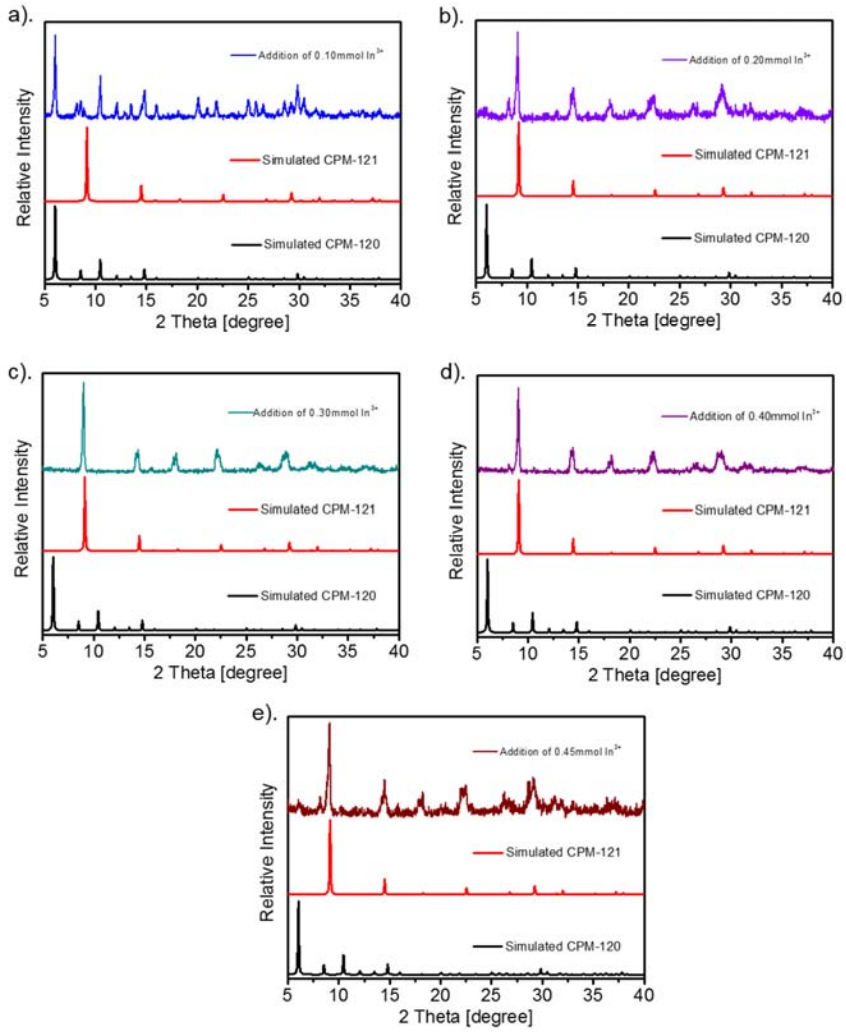

Figure 2.6 PXRD patterns of the as-synthesized product when different amounts of In^{3+} was added as the precursor when synthesizing CPM-120-ZnGeS-AEM.

Up to now, the super-sodalite type T2 cluster based chalcogenide can be fulfilled in three different combinations of metal cations, and they are M_1^{4+}/M_2^{3+}, M_1^{4+}/M_3^{2+} and $M_1^{4+}/M_2^{3+}/M_3^{2+}$. Here it is worth noting that tetravalent metal cation is a necessary element building T2 based super-sodalite type chalcogenide. Possibly this is because M_2^{3+}/M_3^{2+} chemical composition usually result in the formation of larger clusters such as T4 and T5, otherwise there are too many negative charges in the forming T2 clusters which would not be stable or there are no enough spaces for the charge-balancing protonated amines to fill into the cages. In the above case, by the help of the modulator Ga^{3+}, the morphology can be largely improved while maintaining the structure of the framework. In comparison, the introduction of indium cations with large radius will lead to the super-diamond type structure.

2.3.4 Structural Alternation from Super-sodalite to Super-diamond Type

Such a general platform endows an opportunity to study other doping effects. In order to tune band structure of this T2 cluster based material, we explore if other metal cations can be incorporated into this framework or other analogues. Our first try to complete replace germanium completely with tin under the same reaction conditions fails, producing the unknown amorphous powder. Rational tuning of reaction conditions cannot result in the successful formation of any structures, possibly because of the rich coordination chemistry of tin. In a number of cases, tin prefer forming the layer structures when reacting with chalcogen species.

Cooperative crystallization method has been proven successful in the synthesis of other crystalline porous materials. Inspired by this method and the introduction of indium as mentioned above, the cooperative crystallization of germanium and tin can be fulfilled by adopting this T2 cluster. Possessing the similar radius, the introduction of tin should result in the similar results as indium, which is the phase alternation.

Several batches of experiments have been designed, targeting the synthesis of this material with germanium and tin co-existing (see details in Table 2.2 and 2.3 in Experimental Section). After optimizing the ratio of germanium and tin, pure crystalline powder of CPM-121 can be synthesized (denoted as CPM-121-ZnGeSnS-AEM here) as expected. The as-synthesized compounds has been conformed pure by matching the PXRD pattern with the simulated CPM-121 type structure (Figure 2.7).

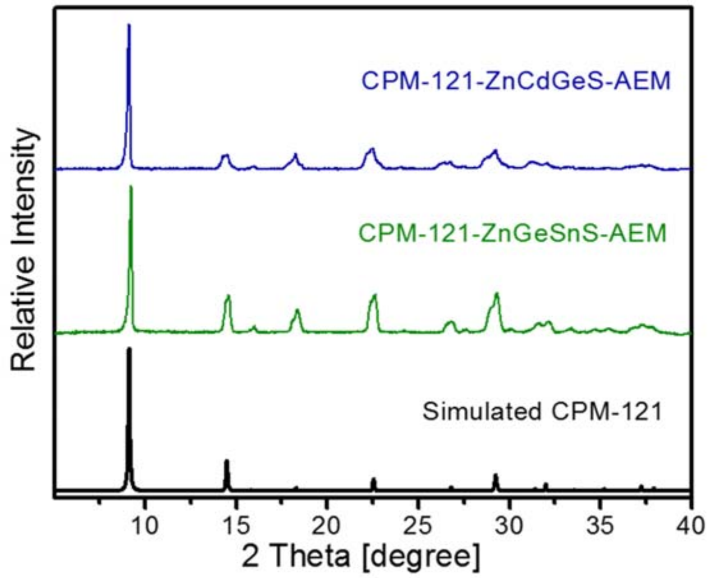

Figure 2.7 PXRD patterns of as-synthesized CPM-121-ZnGeSnS-AEM and CPM-121-ZnCdGeS-AEM.

It is also interesting to note that co-crystallization of germanium and tin in one material, even in one cluster, is quite rare in open framework chalcogenide. To the best of our knowledge, this is the first example in open framework chalcogenide that germanium and tin co-exist in supertetrahedral cluster. Dehnen and co-workers reported a Ge-Sn coexisting selenide before. In that case, the framework is based on two secondary building blocks: $[Ge_3Se_9]^{6-}$ and $[Sn_6Se_{18}]^{12-}$, which means that germanium and tin crystallize in different building units of the framework. However, in our case, germanium and tin co-crystallize in the same building block.

In the structure of CPM-121-ZnGeSnS, T2 clusters connect together to give a diamond type structure through sharing four corner sulfur anions (Figure 2.1c). The introduction of tin to the T2 cluster further proves the phase alternation occcurs when metal cations with different radius were incorporated into this trimetallic T2 clusters. Here, possible reasons were proposed to demonstrate the phase alternation: 1) as is well known, sodalite-type structure is more stable than diamond type, when based on the same composition and building blocks. Tin or indium possesses much larger radius when compared with zinc and germanium. As mentioned above, distinctive radius difference between metal cations at the equivalent positions is not favorable for the crystallization process, possibly resulting in other relatively less stable structures or kinetic product; 2) sodalite-type structure contains four-membered and six-membered rings while diamond type structure possesses only six-membered rings. The angles inside the six-membered rings should be more flexible than that in four-membered rings. When tin or indium was introduced, M-S-M bond between two T2 clusters would be smaller than that when there are only germanium and zinc, possibly better fitting to the relatively flexible six-membered rings. These two explanations can well demonstrate that when metal cations of larger radius was introduced, relatively less stable diamond-type structure containing only six-membered rings can be formed.

Another case was also performed to prove that the phase alternation in the trimetallic porous chalcogenide was induced by the radius difference. Cadmium was tried to incorporate into the cluster. Similar to the case of incorporation of tin, the initial try of complete replacement of zinc by cadmium cannot lead to the target material. Interestingly, the pure colorless octahedral shaped crystals can be obtained when decreasing the amount of sulfur added to the reaction through the co-crystallization of zinc and cadmium. Unfortunately, the dimension of the crystals is so tiny that it is not suitable for the single crystal analysis. The PXRD pattern conformed the product is diamond structured CPM-121 by matching with the simulated one (Figure 2.7). SEM-EDS result shows that the crystal contains germanium, zinc and cadmium (denoted as CPM-121-ZnCdGeS-AEM here).

There is only one previous report about zinc and cadmium co-existing open framework chalcogenide based on supertetrahedral cluster. In that case, zinc and cadmium also exist in one T2 cluster but the 3D structure is an augmented-diamond type.

Table 2.5 Structure type, atomic ratio, chemical composition and band gap of CPM-121-ZnGeSnS-AEM and CPM-121-ZnCdGeS-AEM.

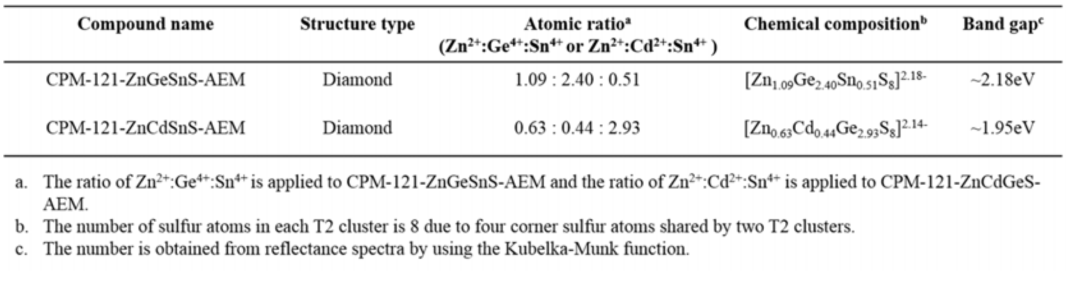

Compound name	Structure type	Atomic ratio[a] (Zn^{2+}:Ge^{4+}:Sn^{4+} or Zn^{2+}:Cd^{2+}:Sn^{4+})	Chemical composition[b]	Band gap[c]
CPM-121-ZnGeSnS-AEM	Diamond	1.09 : 2.40 : 0.51	$[Zn_{1.09}Ge_{2.40}Sn_{0.51}S_8]^{2.18-}$	~2.18eV
CPM-121-ZnCdSnS-AEM	Diamond	0.63 : 0.44 : 2.93	$[Zn_{0.63}Cd_{0.44}Ge_{2.93}S_8]^{2.14-}$	~1.95eV

a. The ratio of Zn^{2+}:Ge^{4+}:Sn^{4+} is applied to CPM-121-ZnGeSnS-AEM and the ratio of Zn^{2+}:Cd^{2+}:Sn^{4+} is applied to CPM-121-ZnCdGeS-AEM.
b. The number of sulfur atoms in each T2 cluster is 8 due to four corner sulfur atoms shared by two T2 clusters.
c. The number is obtained from reflectance spectra by using the Kubelka-Munk function.

The details of the chemical composition about these two super-diamond type frameworks were summarized in Table 2.5. In CPM-121-ZnGeSnS-AEM, the atomic ratio of Zn: Ge: Sn is 1.09: 2.40: 0.51. If compared with T2 clusters in CPM-120-ZnGeS-AEM, it seems that tin cations will mainly replace germanium with slightly replacing zinc due to the charge matching. The chemical composition here is $[Zn_{1.09}Ge_{2.40}Sn_{0.51}]^{2.18-}$. The same situation occurs in CPM-121-ZnCdGeS. Most of divalent cadmium cations occupy the position of zinc, while the left occupy the position of germanium, leading the final atomic ratio of Zn: Cd: Ge to 0.63: 0.44: 2.93 with the chemical composition $[Zn_{0.63}Cd_{0.44}Ge_{2.93}]^{2.14-}$. No matter tin or cadmium cations were added to the crystallizing process, the atomic ratio of divalent to tetravalent metal cations are almost the same in the resulting cluster. In CPM-121-ZnGeSnS sample, the ratio of M^{2+}: M^{4+} is 1.09: 2.91, while this ratio is 1.07: 2.93 in the sample of CPM-121-ZnCdGeS.

2.3.5 Tunable Band Gaps

The electronic band gaps of solid-state semiconductor is highly influenced by the chemical composition and structure. Generally, continuous incorporation of one species to the framework will lead to one direction shift on the band gap spectrum (blue shift or red shift). However, in our work, the fact that gallium replace different positions (germanium or zinc) in CPM-120 will lead to red shift and blue shift, which will assign different chemical compositions to different positions through a particular band gap range.

As shown in Figure 2.8, while CPM-120-ZnGeS-AEM possesses a band gap of ~1.90eV, the replacement of germanium by gallium will result in a blue shift (addition of 0.10mmol Ga^{3+} gives the band gap of ~2.30eV). The following red shift of the band gap result from the fact that gallium mainly replace the position of zinc (2.20eV, 2.12eV, 2.16eV and 2.13eV, respectively). The trend of this series of band gap matches well with the elemental ratio in the structure. It is worth mentioning that in the frameworks, the conduction band is mainly tuned as it is dominated by metal cations.

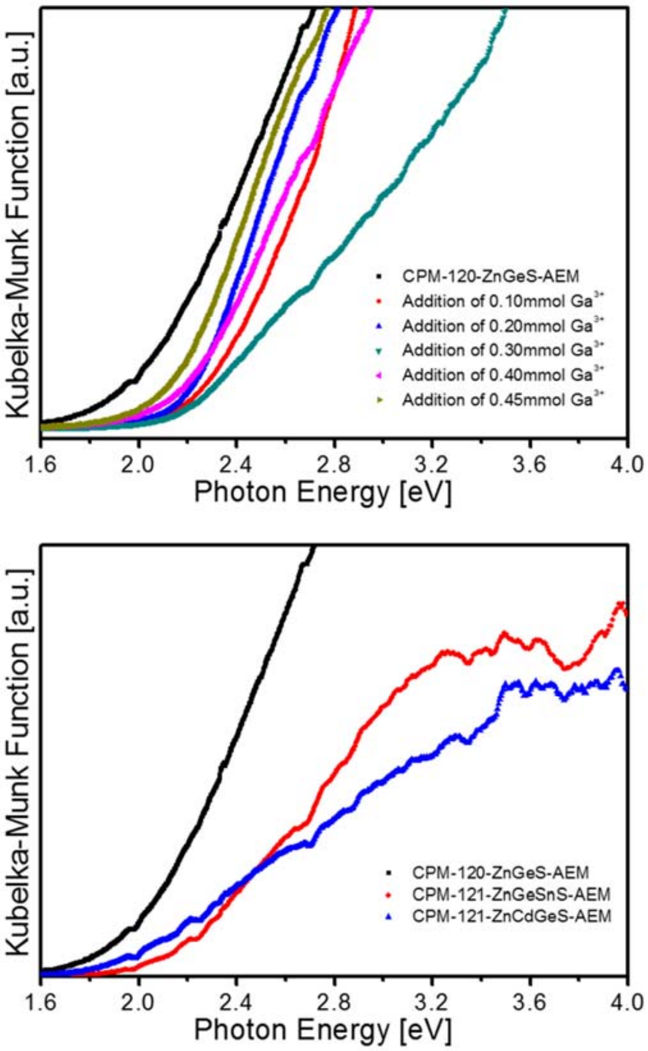

Figure 2.8 top: Normalized solid-state UV-vis adsorption spectra of CPM-120-ZnGeS-AEM with gallium-doped analogues; bottom: Normalized solid-state UV-vis adsorption spectra of CPM-120-ZnGeS-AEM, CPM-121-ZnGeSnS-AEM and CPM-121-ZnCdGeS-AEM.

It is well known that the structure type have a large effect on the band gap. When tin or cadmium is introduced, the formed CPM-121 possess the band gaps of 2.18eV (Sn-doped) and 1.95eV (Cd-doped), respectively (Figure 2.8, bottom). If the as-synthesized structure is still sodalite type, no matter Sn- or Cd-doped, the band gap should have a red shift. However, the formed products possess larger band gap than that of CPM-120-ZnGeS. This can well demonstrate that generally, the band gap of diamond-type structure here is larger than that of sodalite-type if the chemical composition with their atomic ratio is the same.

2.3.6 Cation Exchange and Gas Adsorption

The bulky protonated AEM cations occupy the void space of the channel, which can be ion-exchanged out by Cs^+. However, Cs^+-exchanged product in different crystal structure shows different stability. PXRD patterns show that after Cs^+ exchange, CPM-120-ZnGaGeS-AEM remains the crystallinity (Cs^+ exchanged produce is denoted as CPM-120-ZnGaGeS-Cs here). However, there is no more peaks in CPM-121, no matter what chemical composition the framework is(Sn-doped or Cd-doped). This indicates that the super-sodalite type structure is much more stable than super-diamond type in nature after cation exchange. TGA results shows that CPM-120-ZnGaGeS-Cs can be stable up to 600°C in inert gas atmosphere (Figure 2.9). From the nitrogen adsorption (Figure 2.10), it reveals the highly porous nature of the framework. The material shows type I sorption isotherms with the BET surface area of 467.19m^2 g^{-1}. The volumetric carbon dioxide adsorption also shows quite promising ability for capture of carbon dioxide. As shown in

Figure 2.11, at 273K, the volumetric CO_2 adsorption is 5.86 mmol/cm^3 at 1 bar. While at 298K, the volumetric CO_2 uptake is 4.45 mmol cm^{-3} at 1 bar, which is comparable to some ideal CO_2 adsorbers of MOF materials, such as Mg_2(dobpdc) and HKUST-1. The isosteric heat of adsorption is ~29 kJ mol^{-1} at low coverage. IAST (Ideal Adsorbed Solution Theory) results show that the selectivity of CO_2/CH_4 (15/85) is as high as 51.40:1. This high selectivity can be attributed to the strong interaction between acidic CO_2 molecules and basic sulfur atoms in the framework.

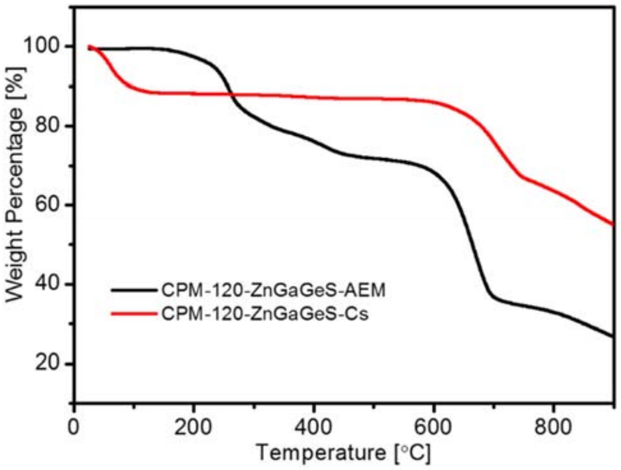

Figure 2.9 TGA for CPM-120-ZnGaGeS-AEM and CPM-120-ZnGaGeS-Cs.

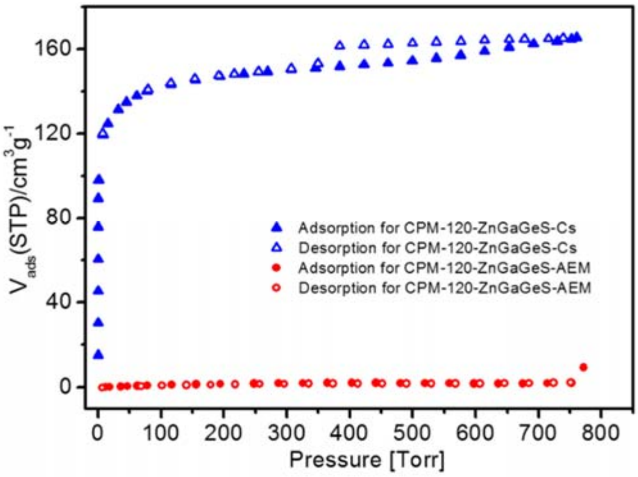

Figure 2.10 N_2 sorption isotherms (77K) for CPM-120-ZnGaGeS-AEM and CPM-120-ZnGaGeS-Cs.

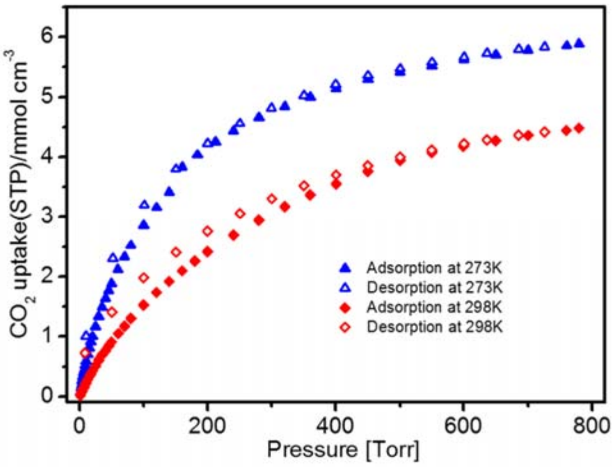

Figure 2.11 CO_2 sorption isotherms (273K and 298K) for CPM-120-ZnGaGeS-Cs.

2.3.7 Hydrogen Evolution

As the semiconductor materials, all of them show promising photocatalytic hydrogen production properties. The photocatalysis were performed in the closed gas circulation system, attached with gas chromatography (GC) with thermal conductivity detector (TCD). The sacrificial reagent used here is Na_2S-Na_2SO_3 (0.25M-0.10M) in degassed aqueous solutions. Under UV-vis light irradiation, the photocataytic hydrogen production is 70.86, 56.53 and 47.50 μmol h^{-1}/50mg for CPM-121-ZnCdGeS, CPM-120-ZnGaGeS and CPM-121-ZnGeSnS, respectively (Figure 2.12). This indicates that incorporation of Cd^{2+} into the Zn^{2+}/Ge^{4+} T2 cluster can enhance the performance of photocatalytic hydrogen production, possibly due to the enhancement of charge-hole separation ability.

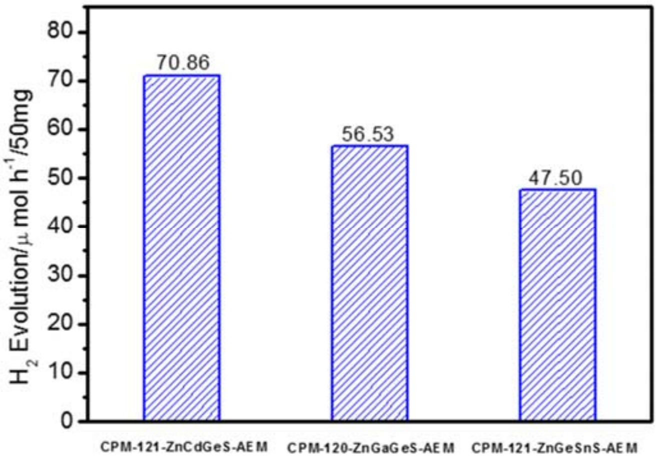

Figure 2.12 Photocatalyic H_2 evolution of CPM-121-ZnCdGeS-AEM, CPM-120-ZnGaGeS-AEM and CPM-121-ZnGeSnS-AEM in Na_2S-Na_2SO_3 (0.25M-0.10M) degassed aqueous solutions without loading any co-catalyst under UV-vis light illumination.

2.4 Conclusion

Based on the platform of bimetallic ternary open framework chalcogenide CPM-120-ZnGeS, the dramatic effect of tuning of chemical composition is well demonstrated.

Optimization of crystallization or phase alternation can be obtained through employing metal cations with different charges or/and radius. Through the atomic ratio, the precise replacement can be determined. One interesting discovery is that the doped Ga^{3+} will replace the position of Ge^{4+} first and then replace Zn^{2+}, thus assigning different doping extent to various band gaps. The cooperative crystallization was firstly proved successful in crystalline chalcogenide materials. Those crystalline porous materials can function as effective photocatalysts for hydrogen evolution. In addition, CPM-120-ZnGaGeS shows quite promising carbon capture ability.

2.5 Reference

(1) Krebs, B.; Voelker, D.; Stiller, K.-O. *Inorg. Chim. Acta*, 1982, **65**, L101-L102.

(2) Wang, C.; Li, Y.; Bu, X.; Zheng, N.; Zivkovic, O.; Yang, C.-S.; Feng, P. *J. Am. Chem. Soc.*, 2001, **123**, 11506-11507.

(3) Lin, Y.; Massa, W.; Dehnen, S. *J. Am. Chem. Soc.*, 2012, **134**, 4497-4500.

(4) Zhang, X.-M.; Sarma, D.; Wu, Y.-Q.; Wang, L.; Ning, Z.-X.; Zhang, F.-Q.; Kanatzidis, M. G. *J. Am. Chem. Soc.*, 2016, **138**, 5543-5546.

(5) Manos, M. J.; Kanatzidis, M. G. *J. Am. Chem. Soc.*, 2009, **131**, 6599-6607.

(6) Zhang, Q.; Chung, I.; Jang, J. I.; Ketterson, J. B.; Kanatzidis, M. G. *J. Am. Chem. Soc.*, 2009, **131**, 9896-9897.

(7) Bag, S.; Kanatzidis, M. G. *J. Am. Chem. Soc.*, 2010, **132**, 14951-14959.

(8) Fang, L.; Iyer, R. G.; Tan, G.; West, D. J.; Zhang, S.; Kanatzidis, M. G. *J. Am. Chem. Soc.*, 2014, **136**, 11079-11084.

(9) Li, H.; Laine, A.; Keeffe, M.; Yaghi, O. M. *Science*, 1999, **283**, 1145.

(10) Li, H.; Eddaoudi, M.; Laine, A.; O'Keeffe, M.; Yaghi, O. M. *J. Am. Chem. Soc.*, 1999, **121**, 6096-6097.

(11) Zheng, N.; Bu, X.; Feng, P. *J. Am. Chem. Soc.*, 2003, **125**, 1138-1139.

(12) Cook, B. A.; Kramer, M. J.; Harringa, J. L.; Han, M.-K.; Chung, D.-Y.; Kanatzidis, M. G. *Adv. Funct. Mater.*, 2009, **19**, 1254-1259.

(13) Trikalitis, P. N.; Rangan, K. K.; Bakas, T.; Kanatzidis, M. G. *Nature*, 2001, **410**, 671-675.

(14) Yu, H.; Brock, S. L. *ACS nano*, 2008, **2**, 1563-1570.

(15) Kanatzidis, M. G.; Huang, S. P. *Inorg. Chem.*, 1989, **28**, 4667-4669.

(16) Yao, Q.; Arachchige, I. U.; Brock, S. L. *J. Am. Chem. Soc.*, 2009, **131**, 2800-2801.

(17) Bag, S.; Trikalitis, P. N.; Chupas, P. J.; Armatas, G. S.; Kanatzidis, M. G. *Science*, 2007, **317**, 490.

(18) Mohanan, J. L.; Arachchige, I. U.; Brock, S. L. *Science*, 2005, **307**, 397.

(19) Lei, Z.; You, W.; Liu, M.; Zhou, G.; Takata, T.; Hara, M.; Domen, K.; Li, C. *Chem. Commun.*, 2003, 2142-2143.

(20) Zheng, N.; Bu, X.; Vu, H.; Feng, P. *Angew. Chem. Int. Ed.*, 2005, **44**, 5299-5303.

(21) Cahill, C. L.; Parise, J. B. *Chem. Mater.*, 1997, **9**, 807-811.

(22) Cahill, C. L.; Ko, Y.; Parise, J. B. *Chem. Mater.*, 1998, **10**, 19-21.

(23) Cahill, C. L.; Ko, Y.; Hanson, J. C.; Tan, K.; Parise, J. B. *Chem. Mater.*, 1998, **10**, 1453-1458.

(24) Vaqueiro, P.; Romero, M. L.; Rowan, B. C.; Richards, B. S. *Chemistry – A European Journal*, 2010, **16**, 4462-4465.

(25) Ruzin, E.; Dehnen, S. *Z. Anorg. Allg. Chem.*, 2006, **632**, 749-755.

(26) Zimmermann, C.; Anson, C. E.; Weigend, F.; Clérac, R.; Dehnen, S. *Inorg. Chem.*, 2005, **44**, 5686-5695.

(27) Vaqueiro, P.; Romero, M. L. *Inorg. Chem.*, 2009, **48**, 810-812.

(28) Santner, S.; Dehnen, S. *Inorg. Chem.*, 2015, **54**, 1188-1190.

(29) Vaqueiro, P.; Romero, M. L. *J. Am. Chem. Soc.*, 2008, **130**, 9630-9631.

(30) Feng, P.; Bu, X.; Zheng, N. *Acc. Chem. Res.*, 2005, **38**, 293-303.

(31) Bu, X.; Zheng, N.; Feng, P. *Chemistry – A European Journal*, 2004, **10**, 3356-3362.

(32) Wu, T.; Bu, X.; Zhao, X.; Khazhakyan, R.; Feng, P. *J. Am. Chem. Soc.*, 2011, **133**, 9616-9625.

(33) Wu, T.; Wang, L.; Bu, X.; Chau, V.; Feng, P. *J. Am. Chem. Soc.*, 2010, **132**, 10823-10831.

(34) Zheng, N. F.; Bu, X. G.; Wang, B.; Feng, P. Y. *Science*, 2002, **298**, 2366-2369.

(35) Lin, Q.; Bu, X.; Mao, C.; Zhao, X.; Sasan, K.; Feng, P. *J. Am. Chem. Soc.*, 2015, **137**, 6184-6187.

(36) Hu, D.; Zhang, Y.; Lin, J.; Hou, Y.; Li, D.; Wu, T. *Dalton Transactions*, 2017, **46**, 3929-3933.

(37) Bu, X.; Zheng, N.; Wang, X.; Wang, B.; Feng, P. *Angew. Chem. Int. Ed.*, 2004, **43**, 1502-1505.

(38) Lin, J.; Dong, Y.; Zhang, Q.; Hu, D.; Li, N.; Wang, L.; Liu, Y.; Wu, T. *Angew. Chem. Int. Ed.*, 2015, **54**, 5103-5107.

Chapter 3 Selective Ion Exchange and Photocatalysis by Zeolite-Like Semiconducting Chalcogenide

3.1 Introduction

Selectivity to pre-defined characteristics of reaction species is one of the most important considerations in the design of advanced catalysts. A great progress has been made in the design of conventional heterogeneous catalysts with high selectivity.[1-4] For example, zeolites, which are a family of highly useful solid acid catalysts, can exhibit high selectivity with respect to the size and shape of reactants, intermediates, and products, due to their uniform pore size.[5-7] In comparison, similarly selective photocatalysts are few, which is because heterogeneous photocatalysts are predominantly non-porous materials such as TiO_2 and CdS.[8-10] So far, research on photocatalysts has been mostly centered on features such as band structures, morphologies, and co-catalysts.[11-24] The selectivity of photocatalysts has received much less attention, likely due to the difficulty in designing semiconducting photocatalysts with structural and topological properties similar to those of zeolites.[25-31]

In the past two decades, we and others have made a dramatic progress in the synthesis of open-framework metal chalcogenides,[32-49] which is one series of crystalline porous materials[50-54] with semiconducting property, uniform porosity and high surface area. A common basic structural building unit is the supertetrahedral cluster, denoted as Tn cluster, where n is the number of metal sites along each edge of the cluster. These supertetrahedral clusters can replace tetrahedrally coordinated Si^{4+}/Al^{3+} sites in zeolites to form 3-D open-framework materials, thus mimicking zeolite connectivity. The highly porous property has endowed them with unique properties and applications, such as gas sorption, ion exchange, ionic conductivity, and photocatalytic production of H_2. [55-63]

Most traditional photocatalysts are based on non-porous materials.[64-67] The photo-generated electron-hole pairs in such dense solids may have to travel a relatively long distance in order to reach target reactants on the surface. This can not only be detrimental to the reaction kinetics, but also contributes to a greater degree of electron-hole recombination. With crystalline porous semiconductors,[68] redox chemistry can occur within the internal pore space, which can contribute to reduced probability for electron-hole recombination and high photocatalytic efficiency. It may also be possible to permit or block the access of reactants to the internal pores based on their size or charge, leading to differing photocatalytic rates of different species and high selectivity.

In this work, we select a zeolite-like semiconducting chalcogenide, CPM-120-ZnGaGeS-AEM (denoted as **1-AEM** here, CPM=Crystalline Porous Material and AEM=4-(2-aminoethyl)morpholine), as the platform for the study of selective photocatalysis. The bulky protonated AEM cations here can be exchanged with Cs^+, which gives the structural analogue, named as **1-Cs** here. In the following, we show the dramatic effect of porosity, charge of the framework, and ion-exchange properties of **1-Cs** and **1-AEM** on the selective adsorption and photocatalytic reactions of dye molecules.

3.2 Experimental Section

3.2.1 Chemicals

Germanium dioxide (GeO_2, 99.999%), gallium nitrate hydrate ($Ga(NO_3)_3\cdot xH_2O$, 99.9998%) and zinc nitrate hexahydrate ($Zn(NO_3)_2\cdot 6H_2O$, 98%) were purchased from Acros. N-(2-aminoethyl)-morpholine (AEM, 98%+) and sulfur powder (S, 100mesh, 99.5%) were purchased from Alfa Aesar. All chemicals were used as purchased without further purification. TiO_2 with self-doped Ti^{3+} was synthesized according to the literature.[3c]

3.2.2 Preparation of CPM-120-ZnGaGeS-AEM

125mg GeO_2, 117mg $Ga(NO_3)_3\cdot xH_2O$, 90mg $Zn(NO_3)_2\cdot 6H_2O$, 260mg S and 3.0mL AEM were mixed thoroughly in a 23mL Teflon-lined stainless autoclave and stirred for 1 hour. After heating the sealed reaction mixture at 190 °C for 12 days, around 150mg of small pale yellow rhombic-dodecahedral crystals were obtained. The powder impurities can be washed away using methanol. The pure crystals were obtained by filtering and washing with extra methanol. The phase purity was supported by Powder x-ray diffraction (PXRD). The presence and ratio of Zn/Ga/Ge/S were confirmed by energy dispersive spectroscopy (EDS).

3.2.3 General Characterization

Powder X-ray Diffraction (PXRD) data were performed a Bruker D8 Advance powder diffraction meter with CuKα radiation (40 kV, 40 mA, λ = 1.5418 Å). The simulated powder pattern was calculated using single-crystal X-ray diffraction data of CPM-120-ZnGeS and processed by the Mercury 2.3 program provided by the Cambridge Crystallographic Data Centre. Thermogravimetric analysis (TGA) was performed on a TA Instruments TGA Q500 in the temperature range of 30°C to 1000°C under nitrogen flow with a heating rate of 5°C /min. Scanning electron microscopy (SEM) images and energy dispersive spectroscopy (EDS) data were carried out on Philips FEI XL30 field emission scanning electron microscope (FESEM) equipped with PGT-IMIX PTS EDS detector, or on Nova Nano-SEM450 (Schottky field emission scanning electron microscope) integrated with EDS allowing to perform qualitative and quantitative chemical analysis and image capture. EDS data acquisition was performed with an accelerating voltage of 20 kV and 60 s accumulation time. Microscopic images were performed on Leica MZIII Pursuit. Solid-state diffuse reflectance spectra were recorded on Shimadzu UV-3101PC spectrophotometer. The adsorption spectra were calculated from reflectance spectra by using the Kubelka-Munk function. Gas sorption isotherms were measured on a Micromeritics ASAP 2020 surface-area and pore-size analyzer up to 1 atm of gas pressure by the static volumetric method. Nitrogen gases used were of 99.99% purity, and the impurity trace water was removed by passing the gases through the molecular sieve column equipped in the gas line. The gas sorption isotherms for N_2 were measured at 77 K. All of the samples were degassed at 150 °C overnight before measurement.

3.2.4 Ion-exchange Experiment with Cs^+

CPM-120-ZnGaGeS-AEM was immersed in 20mL 1M CsCl aqueous solution in a glass vial. The vial was then transferred in an 80 °C oven. During the exchange, the CsCl solution was refreshed every 12 hours. After 2 days, the crystals was filtered and washed with water to remove any residual Cs^+ cations on the surface.

3.2.5 Ion-exchange Experiment with Organic Ions

Typically, the experiments were carried out by immersing the CPM-120 materials in the aqueous solutions containing ionic organic species. The solution was kept still during the entire ion-exchange process. 12mg samples were immersed in 10mL 2.5×10^{-5} M organic aqueous solution. The upper clear solution was taken out for UV-vis absorbance measurement at 0h, 2h, 4h, 6h, 8h, 12h, 24h, 48h, 72h and 96h. After each measurement, the solution was poured back to the original solution to avoid the loss of the sample. The absorbance maximum of original organic solution (before ion-exchange) was normalized and the percentage of organic remaining in the solution is calculated by comparing the maximum absorbance wavelength with the original organic solution.

3.2.6 Photocatalytic Activity Test

The photocatalytic activities of CPM-120-ZnGaGeS-AEM and CPM-120-ZnGaGeS-Cs were evaluated by their capability to decompose substrates including RhB^+ and MO^- under visible or UV-vis light irradiation. To carry out photocatalysis tests for the decomposition of RhB^+ and MO^-, 50mg samples were immersed in 100mL 10ppm RhB^+

or MO^- aqueous solution. Before irradiation, the solution was stirred in the dark for 60 min to reach the adsorption-desorption equilibrium. Then, the solution was irradiated using a 300 W xenon lamp with or without a 420nm cutoff filter. The extent of degradation at different irradiation times was determined by the UV−vis absorption measurement of 2 mL of the solution after the removal of the catalyst by centrifugation at 6000 rpm for 10 min. The extent of photocatalytic activity is expressed as A/A0, where A is the absorption at each irradiated time interval of the maximum peak of the absorption spectrum and A0 is the absorption when adsorption/desorption equilibrium was achieved after 1 hour stirring in the dark.

3.3 Results and Discussion

3.3.1 Structural Description and Ion-exchange Property

1-AEM is isostructural to CPM-120-ZnGeS-AEM reported previously.[39] **1-AEM** has a super-sodalite-type structure made of T2 clusters (Figure 3.1) and it has high thermal and hydrothermal stability. The chemical composition of the T2 cluster is $[Zn_{0.76}Ga_{0.70}Ge_{2.54}S_8]^{2.22-}$, according to energy dispersive X-ray spectroscopy. These T2 clusters are joined by corner-sharing sulfur atoms to form a 3-D structure. The sodalite cage contains 4- and 6-membered rings. The aperture size of the 6-membered ring is 7.66Å. The framework is negatively charged, leading to the interaction between the negatively charged sulfur atoms of the host framework and the positively charged extra-framework species. In the as-synthesized form of **1-AEM**, protonated AEM cations occupy the void space in the framework and serve as the charge-balancing species. These AEM cations can be completely ion-exchanged by smaller Cs^+ (the Cs^+-exchanged form is denoted as **1-Cs**). While **1-AEM** displays no porosity, **1-Cs** is highly porous. The BET surface areas of **1-Cs** and **1-AEM** determined by the nitrogen adsorption are quite different, as shown in Figures 3.2 and 3.3. The BET surface area of **1-Cs** is 467.19 m^2/g while **1-AEM** possesses a BET surface area of only 7.28 m^2/g. This is because the bulky protonated AEM cations block the accessible pores in **1-AEM**, and the ion-exchange with much smaller Cs^+ cations gives rise to porous **1-Cs**. In addition to the difference in porosity, the ion exchange rates of **1-Cs** and **1-AEM** with dye cations such as RhB^+ are also different (Figure 3.4) and the exchange rate of RhB^+ with **1-Cs** is much faster than that with **1-AEM**. This indicates that the cation exchange with bulky protonated AEM cations is much slower than that with smaller Cs^+ cations. Here it is worth noting that unlike most photocatalysts that have neutral frameworks, **1-AEM** and **1-Cs** have negatively charged frameworks.

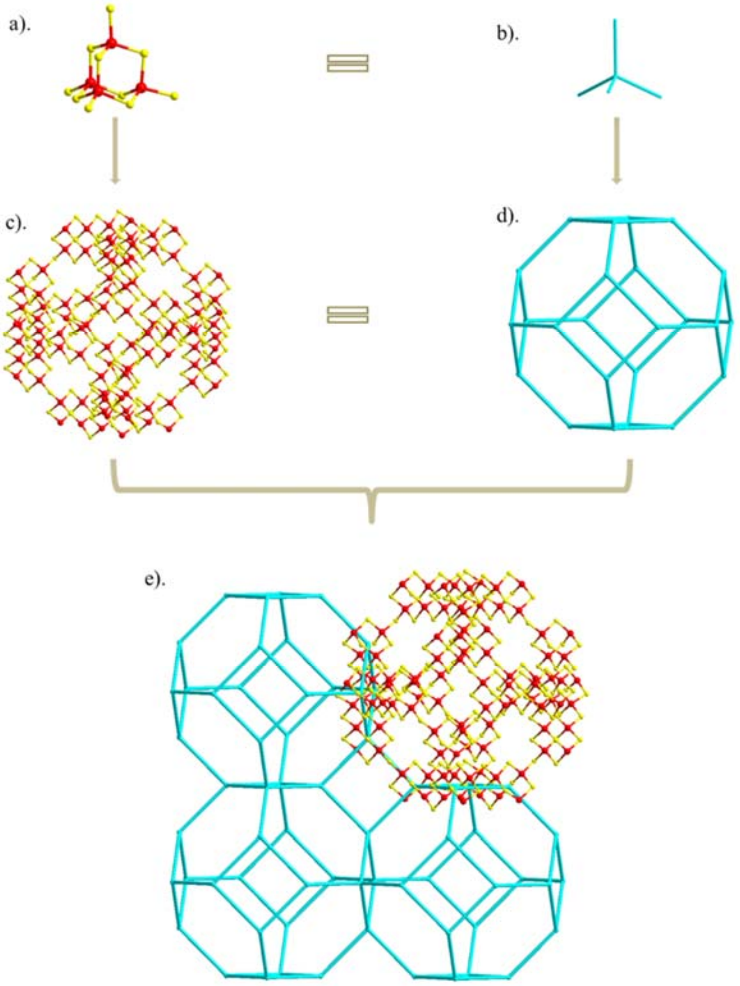

Figure 3.1 Schematic illustration of the self-assembly process from (a) and (b) [M_4S_{10}] T2 cluster to (c) and (d) sodalite cages and finally to (e) the 3D supersodalite network. Red spheres: metal cations (Ge^{4+}, Ga^{3+} and Zn^{2+}); Yellow spheres: S^{2-}.

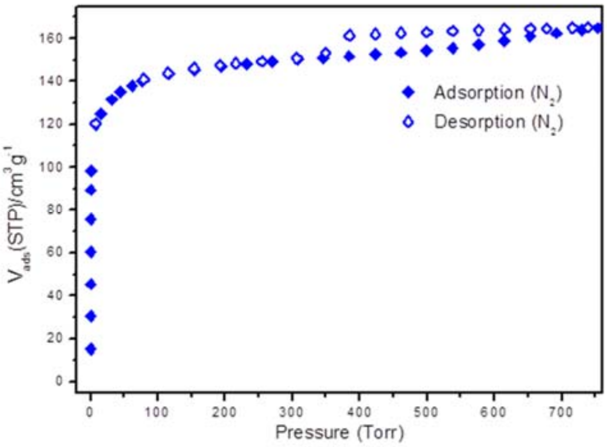

Figure 3.2 Nitrogen adsorption and desorption isotherms for **1-Cs**.

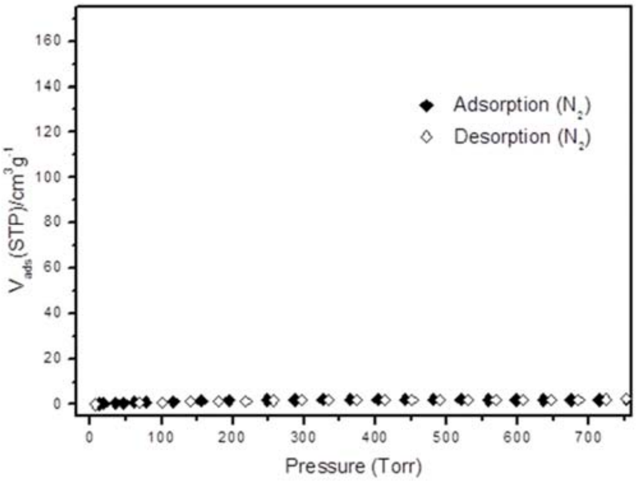

Figure 3.3 Nitrogen adsorption and desorption isotherms for **1-AEM**.

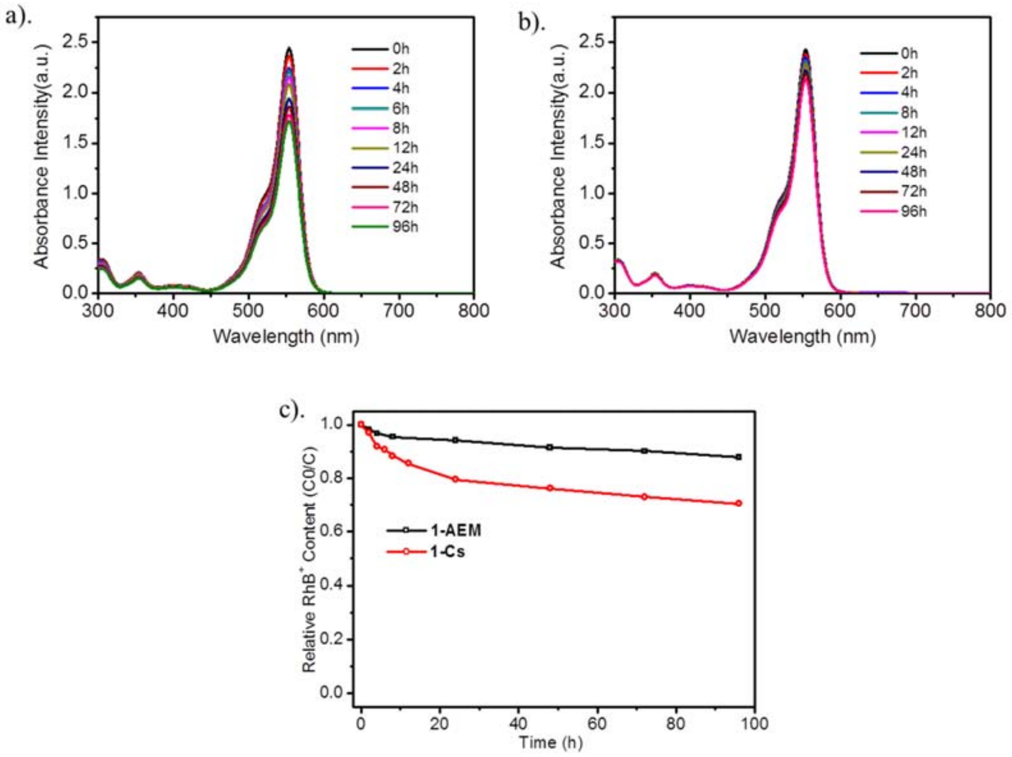

Figure 3.4 UV-vis absorbance of Rhodamine B (**RhB**$^+$) at different time during ion-exchange process with (a) **1-Cs** and (b) **1-AEM** as the host. (c). Percentage of RhB$^+$ remaining in the solution in the presence of **1-AEM** and **1-Cs**, showing the ion-exchange rate in the presence of **1-Cs** is much larger than that in the presence of **1-AEM**.

3.3.2 Charge Selectivity by Open-framework Chalcogenide

For ease of detection, dye molecules are selected as model compounds to study selective properties of our photocatalysts. To study the selectivity with respect to the charge of the dye molecules, a cationic dye molecule (methylene blue, MLB$^+$, 15.1Å × 6.51Å) and an anionic dye molecule (methyl orange, MO$^-$, 14.92Å × 6.28Å) were selected. These two molecules have similar molecular mass and dimensions but opposite charges, which makes them ideal to study the effect of the charge. Here, we firstly demonstrate the charge-dependent selective adsorption using single-component dye solutions. To do this, the same amount of **1-Cs** were immersed in two colored aqueous solutions (blue MLB^+ vs. orange MO^-) for 3 days. Both solutions possess the same volume and concentration of MLB^+ and MO^-. Following the addition of **1-Cs**, the concentrations of two dye molecules in solutions were monitored by UV-vis spectroscopy. It shows that 97% of MLB^+ disappeared from solution and were encapsulated in the pores (through ion-exchange with Cs^+ within the pore). In comparison, for MO^-, almost all remained in the solution (Figure 3.5 a and b) even after 3 days, due to the rejection of MO^- by the negative chalcogenide framework.

We then demonstrate the charge-dependent selective adsorption using mixed dye solutions. To do this, a mixture solution of MLB^+ and MO^- with the same concentration is prepared. Then **1-Cs** crystals with the same amount as that in the first set of experiment were immersed in the mixture. The concentration of MLB^+ underwent a dramatic decrease with time while the concentration of similarly sized MO^- decreased only slightly (Figure 3.5c). The above observation demonstrates that MLB^+ can be selectively encapsulated into the pores of the chalcogenide framework whereas the access by MO^- is denied. The selectivity for cationic organic molecules by this chalcogenide open framework shows that the ion-exchange properties of porous frameworks can be employed to selectively respond to guest species with different charge properties.

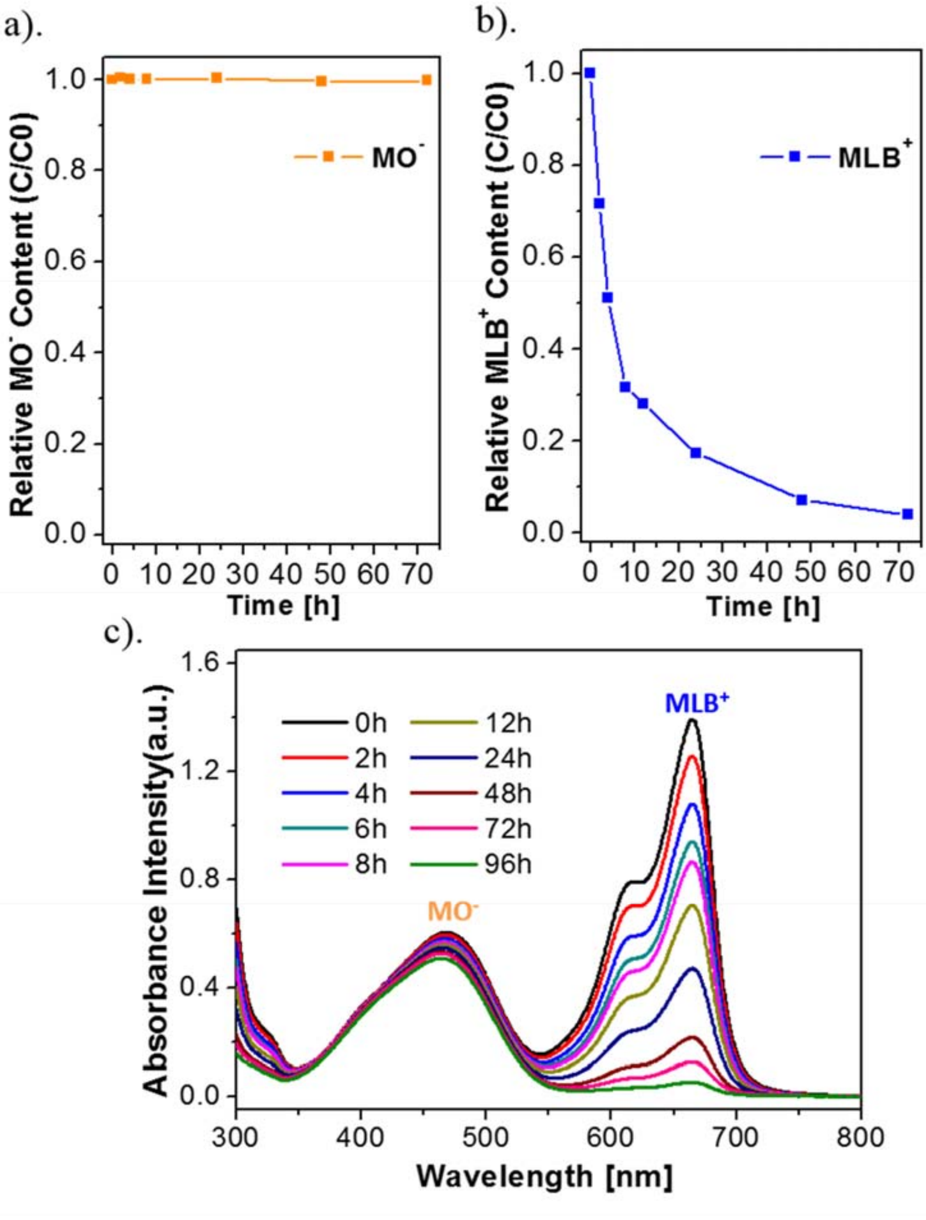

Figure 3.5 a). Relative MO^- content in the presence of **1-Cs** with time. b). Relative MLB^+ content in the presence of **1-Cs** with time. c). UV-vis spectra of equimolar mixture solution of MO^- and MLB^+ in the presence of **1-Cs** with time.

3.3.3 Size Selectivity by Open-framework Chalcogenide

Having demonstrated the selectivity towards the charge of dye species, we next probed the selectivity towards dyes with different sizes, but the same charge. Five cationic molecules with different dimensions were chosen: rhodamine B (RhB^+) > crystal violet (CV^+) > basic fuchsin (BF^+) > phenosafranine (Phf^+) > MLB^+. The molecular structures and dimensions are shown in Figure 3.6. Note that all of them have a charge of +1. These five dyes with same moles were dissolved into five aqueous solution with the same volume and then the same amount of **1-Cs** was immersed into each solution. The ion-exchange process was monitored by UV-Vis spectroscopy periodically. As shown in Figure 3.7, there is a general trend that the ion exchange rate, as well as the extent of exchange, is correlated with the size of dye molecules. The smallest MLB^+ shows the fastest exchange rate and the highest degree of exchange, the bulkiest RhB^+ exhibits the slowest exchange rate and the lowest exchange capacity.

The ion exchange behavior of BF^+ is of particular interest because it deviates from all others. During the first 4 hours, although possessing relatively large size, the exchange rate of BF^+ is even larger than that of MLB^+. However, during the next 8 hours, some of the adsorbed BF^+ molecules are slowly released back to the aqueous solution, leading to an increase in the concentration of BF^+ in the solution. Then, the normal trend resumes as the framework continues to undergo ion exchange with BF^+ molecules, leading to a gradual decrease in the concentration of BF^+ in the solution.

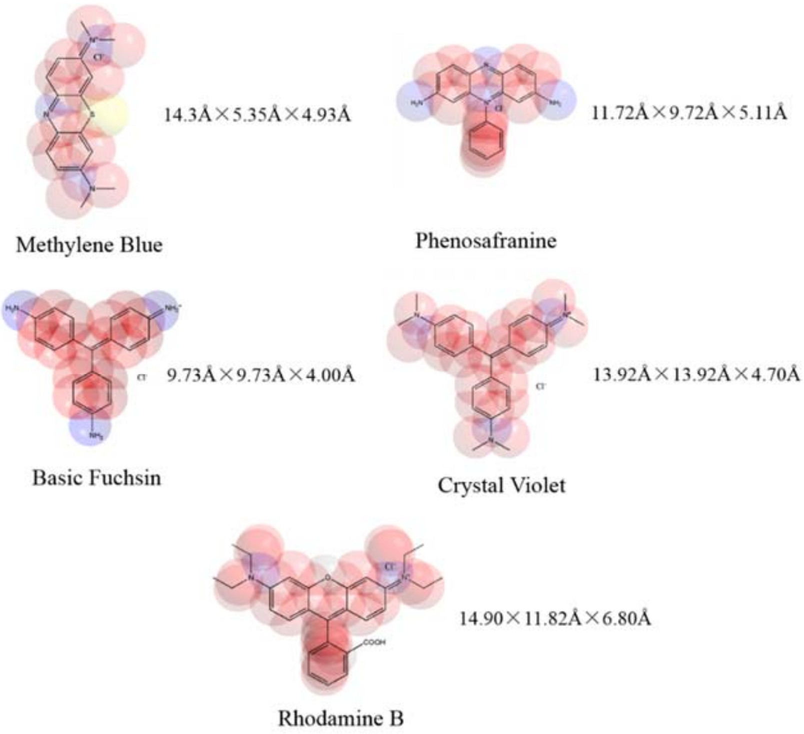

Figure 3.6 Five cationic organic molecules used in this research. The dimensions were measured from 3D molecular models.

Here we propose a possible mechanism for the above observed ion exchange behavior of BF^+. For all other dyes except BF^+, the ion exchange process is slow enough so that there is an adequate amount of time to establish the thermodynamic equilibrium, leading to the thermodynamics-controlled ion-exchange process. On the other hand, the ion exchange process of BF^+ is so fast initially that it shows kinetics-controlled behavior at the beginning. As the pore was being filled up, the ion exchange process slowed sufficiently, which provides the ample time to establish the thermodynamic equilibrium between cationic dyes and Cs^+ cations. In short, the ion exchange process of BF^+ was initially dominated by the kinetics-controlled process, which then gradually changed into the thermodynamics-controlled process.

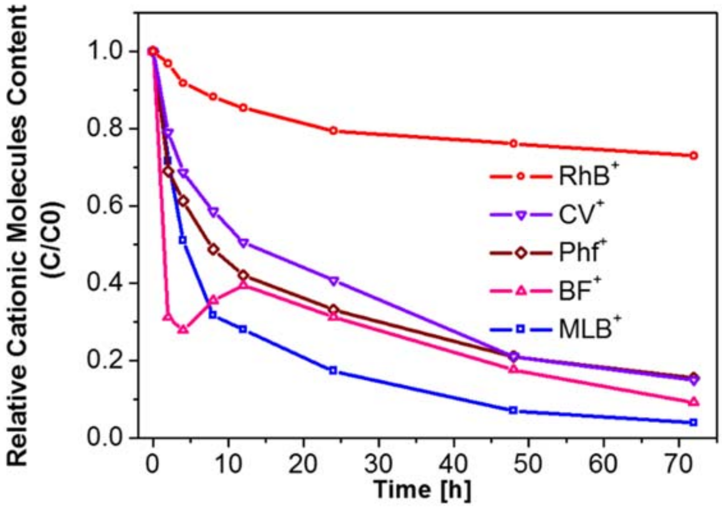

Figure 3.7 Relative content of 5 different sized cationic dyes in aqueous solutions in the presence of **1-Cs** with time.

The unique behavior of BF^+ is related to its different structural features. In all other dyes studied here, the positive nitrogen center is bonded to three alkyl groups, in distinct contrast with BF^+ in which the positive nitrogen site is bonded to only one alkyl group and two hydrogen atoms. This means that BF^+ has a charged, more hydrophilic site that is also capable of forming hydrogen bonding. Since the surface of the chalcogenide framework is highly negative and hydrophilic, it is expected to have much stronger interactions with BF^+, as compared with other cationic dyes. Such stronger interaction is likely responsible for the very fast ion exchange behavior of BF^+ with the chalcogenide framework, contributing to its unusual ion exchange behavior with a transient state of over-saturation in the concentration of exchanged BF^+.

It is worth noting that in their most common conformations, some dimensions of dye molecules chosen here may be larger than the aperture size of super-sodalite cage in **1-Cs**. The successful ion-exchange process with Cs^+, as determined by UV-vis spectra, can be ascribed to the dynamic molecular shapes, as well as possible association and dissociation equilibria of metal-chalcogen bonds in chalcogenide framework. To further confirm that dye cations are ion-exchanged into the internal pore, instead of being adsorbed onto the external particle surface, microscopic images were taken on the intact and crosscut single crystals after ion exchange. Here RhB^+ loaded **1-Cs** crystals were chosen as an example because RhB^+ is the bulkiest among the dye molecules studied. As confirmed by the uniform dyeing throughout the entire crystals, it is clear that RhB^+ stayed inside the crystal after cation exchange (Figure 3.8). To further prove RhB^+ are located inside the cages of the framework as charge balancing species after ion exchange, reversible ion-exchange experiment was performed here. **1-Cs** was firstly immersed in the RhB^+ aqueous solution. The result shows that after 77 days, there are almost no RhB^+ cations left in the solution. Then the crystals were filtered and transferred to 1M CsCl aqueous solution with the same volume. The UV-Vis spectroscopy shows that after 11 days, 52% of RhB^+ was exchanged back to the aqueous solution (Figure 3.9). This process demonstrated that after the first cation exchange, RhB^+ cations were introduced into the cages of the framework. Then the RhB^+ cations in the pores could be exchanged out by Cs^+ cations. The exchanged-out RhB^+

cations exhibit the same characteristic absorbance peak at 554nm, indicating the intactness of RhB^+ during the whole process.

3.3.4 Photocatalytic Activity and Selectivity by Open-framework Chalcogenide

Having demonstrated the charge and size selective adsorption behaviors of dye molecules in the porous semiconducting **1-Cs**, we next seek to study how such selective adsorption affects the photocatalytic activity and selectivity of these metal chalcogenides. In order to probe the effect of porosity on the photocatalytic properties, both porous **1-Cs** and nono-porous **1-AEM** were used as possible catalysts in the photocatalytic experiment involving RhB^+ and MO^-. Here **1-AEM** is deemed non-porous because the direct ion exchange between protonated AEM within the cavities of the framework and organic dye cations in the solution was negligible (Figure 3.4c). The RhB^+ aqueous solution with **1-AEM** was stirred in the dark for 1 hour. Then after 6 hours of visible light irradiation, nearly 80% of RhB^+ was decomposed, as monitored by measuring the characteristic absorption peak of RhB^+ at 554 nm (Figure 3.10b). For anionic MO^-, after 6 hours of UV-vis light irradiation, the concentration of MO^- monitored by UV-vis spectroscopy at 464 nm was decreased by 88% (Figure 3.11b).

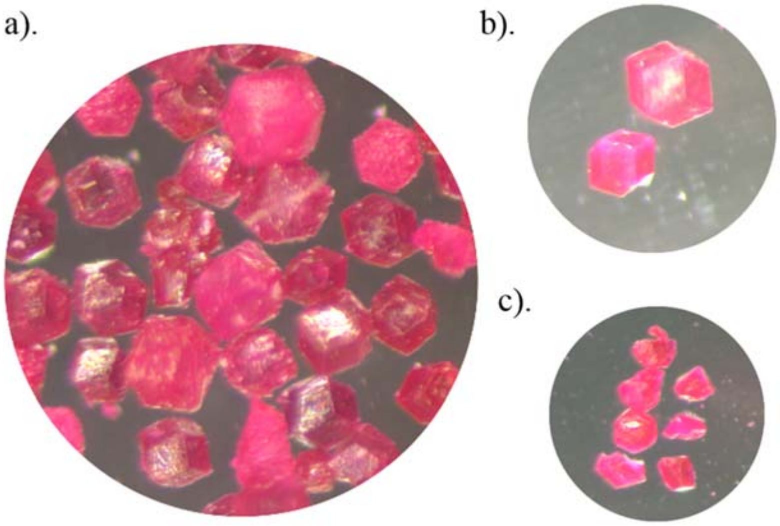

Figure 3.8 Optical microscope images of RhB^+ immersed **CPM-120-ZnGaGeS-Cs**: a). CPM-**120-ZnGaGeS-Cs** crystals; b). two randomly selected crystals; c). inside surface of the above selected crystals.

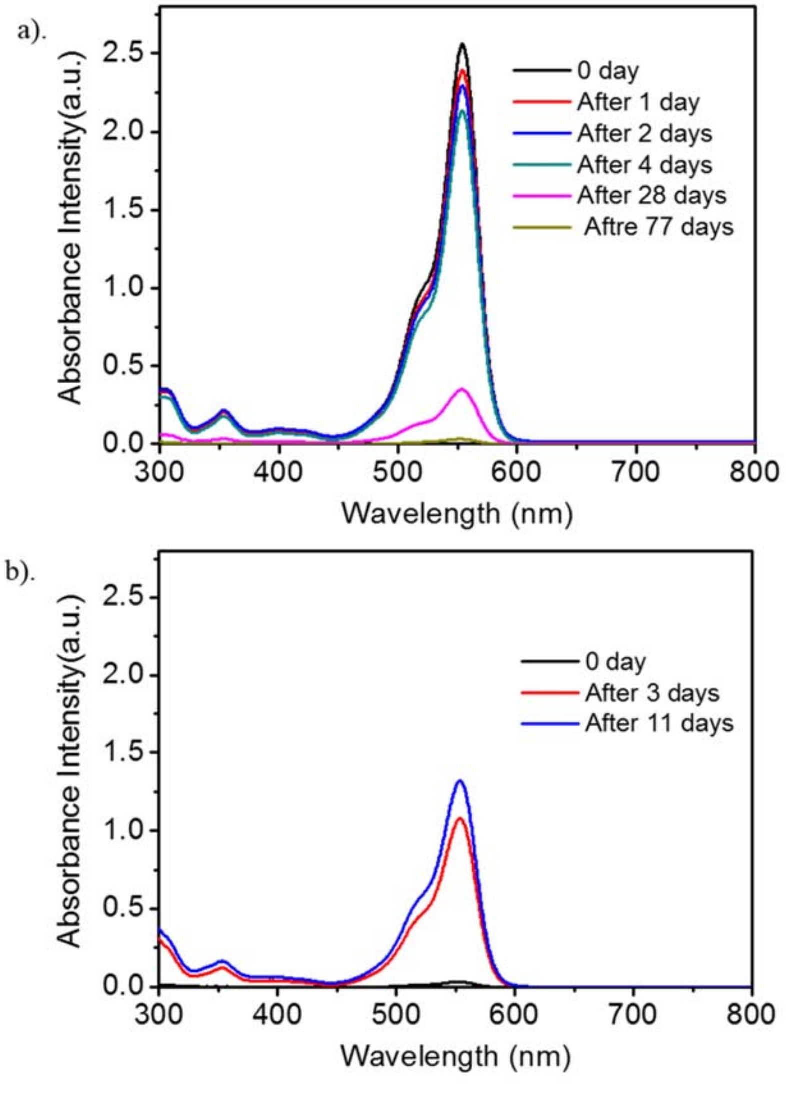

Figure 3.9 a). UV-vis absorbance of Rhodamine B (**RhB$^+$**) at different time during ion-exchange process with **1-Cs** as the host in **RhB$^+$** aqueous solution; b). UV-vis absorbance of Rhodamine B (**RhB$^+$**) at different time during ion-exchange process with **RhB$^+$**@**1-Cs** adduct as the host in 1M CsCl aqueous solution.

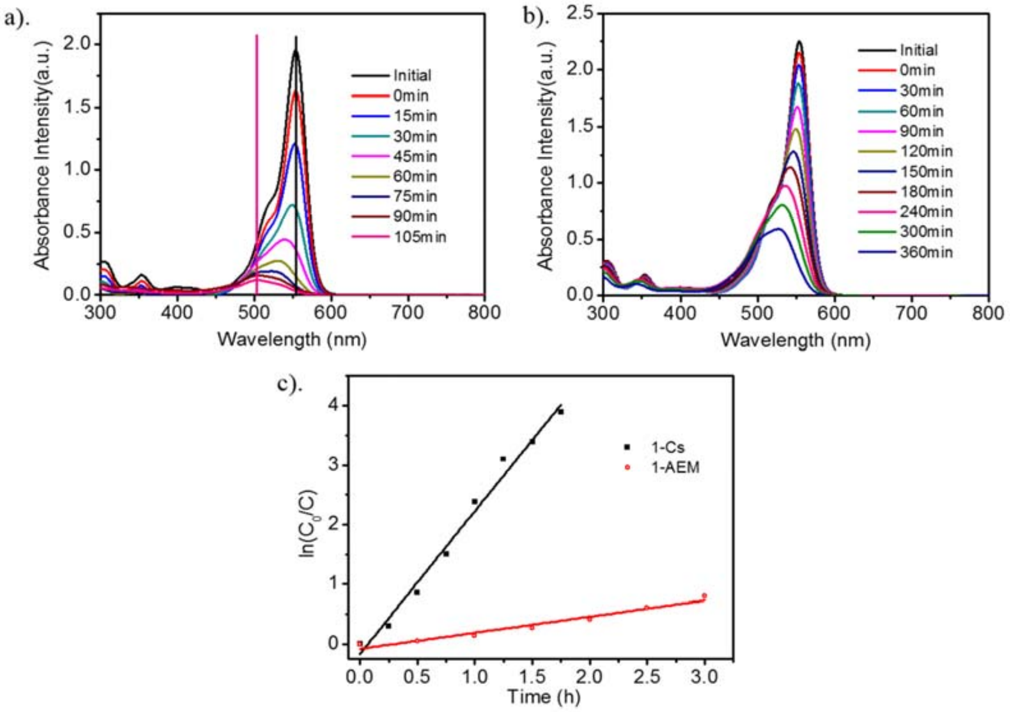

Figure 3.10 UV-vis absorbance of Rhodamine B (**RhB**$^+$) under visible light irradiation at different time in the presence of (a) **1-Cs** and (b) **1-AEM**. (c). Pseudofirst-order plots comparing photocatalytic of activity of RhB$^+$, where $k_{\mathbf{1\text{-}Cs}}$ and $k_{\mathbf{1\text{-}AEM}}$ are the first-order rate constant of **1-Cs** and **1-AEM**, respectively.

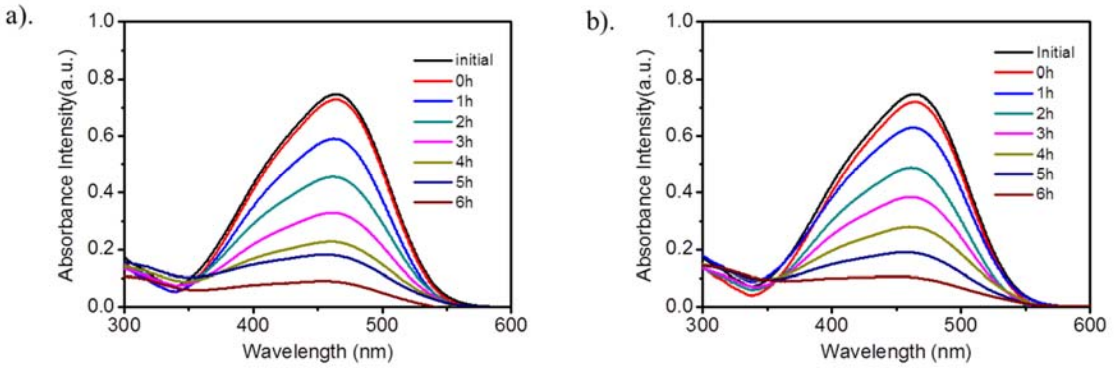

Figure 3.11 UV-vis absorbance of Methyl Orange (**MO**$^-$) under UV-vis light irradiation at different time in the presence of (a) **1-Cs** and (b) **1-AEM**.

A dramatic change in the photocatalytic activity was observed when the porous phase **1-Cs** was used instead of **1-AEM**. The RhB^+ aqueous solution containing **1-Cs** was also stirred in the dark for one hour. Then after 1.5 hours of visible light irradiation, almost all of the RhB^+ were degraded, which was much faster and more complete than that in the presence of **1-AEM** (Figure 3.10 and 3.12). The photocatalyst remained stable after the photocatalytic reaction as demonstrated by PXRD pattern (Figure 3.13 and 3.14). In comparison, the photocatalytic conversion rate of MO^- with **1-Cs** was almost the same as that in **1-AEM** (Figure 3.15). The control experiment showed that only 2% of RhB^+ disappeared after 3 hours under visible light irradiation without any catalysts. The reaction rates of RhB^+ over those two photocatalysts can be fitted to the pseudo first order reaction kinetics equation (Figure 3.10c). The determined rate constant for RhB^+ with **1-Cs** is 2.39 h^{-1}, nine times larger than that in 1-AEM (0.27 h^{-1}). In comparison, the reaction rates of MO^- over those two catalysts are nearly the same.

For comparison, under similar conditions, TiO_2 with self-doped Ti^{3+} was used for photocatalytic decomposition of RhB^+. It is reported that self-doped Ti^{3+} can help enhance the visible light photocatalytic activity. After three hours, only 10% of RhB^+ was decomposed. Even with 400 nm cutoff filter instead of 420 nm, only 21% of RhB^+ was decomposed after 3 hours (Figure 3.16). Those data serve to illustrate that the porous **1-Cs** is a highly efficient photocatalyst. Moreover, the recycling ability of the photocatalytic materials has also been tested. The decomposition amount of RhB^+ on **1-Cs** remained higher than 95% during 4 cycles, showing the good recycling ability and stability of the material (Figure 3.17).

It is quite interesting to emphasize that the positively charged molecule RhB^+ shows quite different photocatalytic activities with 1-**AEM** and **1-Cs**, respectively. There is a nine-fold increase of photocatalytic rate of degradation of RhB^+ in **1-Cs** when compared with **1-AEM**. Although negatively charged molecule MO^- has much smaller dimension than that of RhB^+, it shows almost the same photocatalytic behavior in the presence of non-porous **1-AEM** or porous **1-Cs**. To better understand the observed photocatalytic properties, we compared the optical and physical properties of these two materials (**1-AEM** and **1-Cs**).

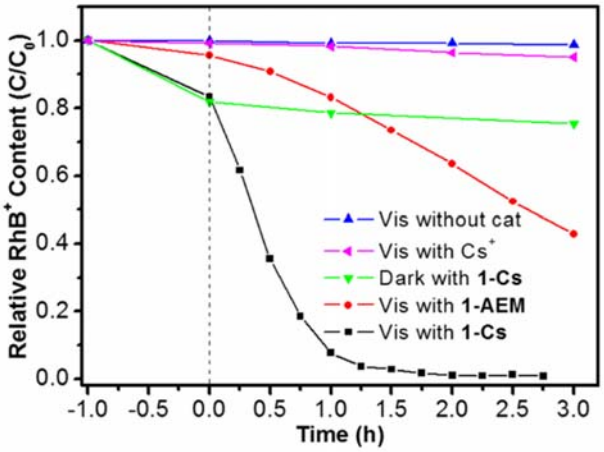

Figure 3.12 Photocatalytic activity of RhB^+ in different conditions with time. When the catalyst (**1-Cs** or **1-AEM**) was added to photocatalytic reaction, the solution was stirred in the dark for 1 hour to reach the adsorption equilibrium (from -1.0 to 0.0 hour period). Vis: Visible light irradiation.

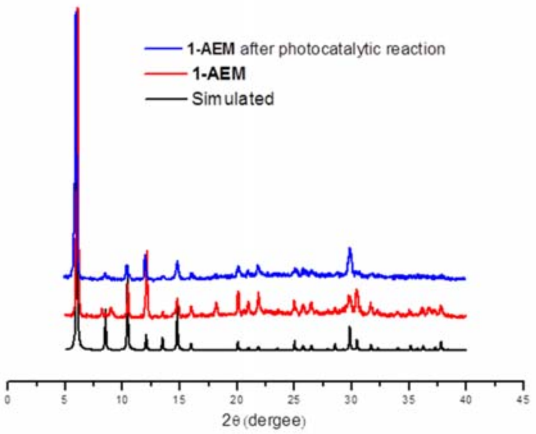

Figure 3.13 Powder XRD patterns for **1-AEM** before and after photocatalytic reactions.

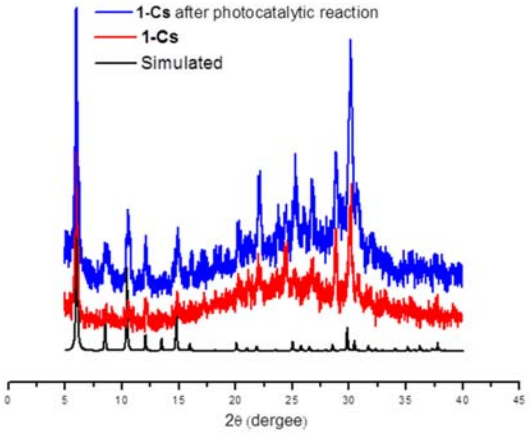

Figure 3.14 Powder XRD patterns for **1-Cs** before and after photocatalytic reactions.

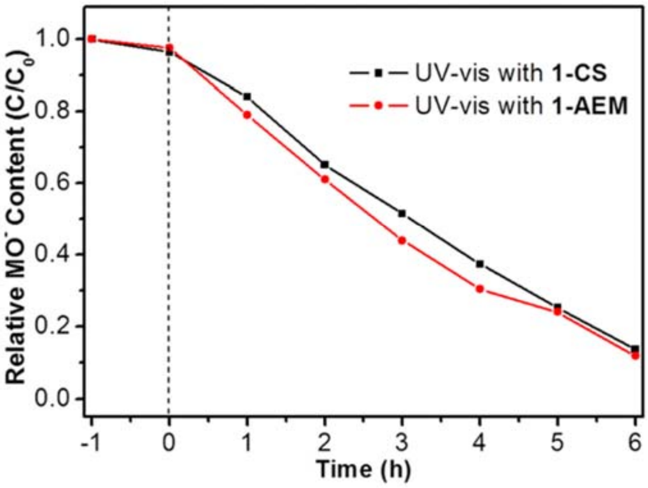

Figure 3.15 Photocatalytic activity of MO^- under different conditions with time. When the catalyst (**1-Cs** or **1-AEM**) was added to photocatalytic reaction, the solution was stirred in the dark for 1 hour to reach the adsorption equilibrium (from -1.0 to 0.0 hour period). UV-Vis: UV-visible light irradiation.

The dramatic difference in photocatalytic activities of **1-Cs** and **1-AEM** with respect to cationic dye molecules is primarily due to the effect of their different porosity, instead of other factors such as stability, the nature of counter cations, or difference in band structures. PXRD patterns of **1-AEM** and **1-Cs** show that before and after ion-exchange all peaks match well with the simulated one (Figure 3.13 and 3.14). A control experiment was carried out to evaluate the impact of Cs^+ on the photocatalytic reaction of RhB^+. The result also illustrates that Cs^+ plays no role in the photocatalytic degradation of RhB^+ (Figure 3.12). From the adsorption edges, **1-AEM** possesses a band gap of 2.13eV while **1-Cs** has a band gap of 2.18eV, determined using Kubelka−Munk methods (Figure 3.18). The transition is likely the result of charge transfer from the S^{2-} dominated valence band to the metal cation dominated conduction band. It is apparent that the extra-framework cations (protonated AEM or Cs^+) have little influence on the band gap. The morphologies and particle size of two photocatalytic materials are almost the same before and after the ion exchange, as shown from scanning electron microscopy (SEM) images (Figure 3.19, 3.20 and 3.21).

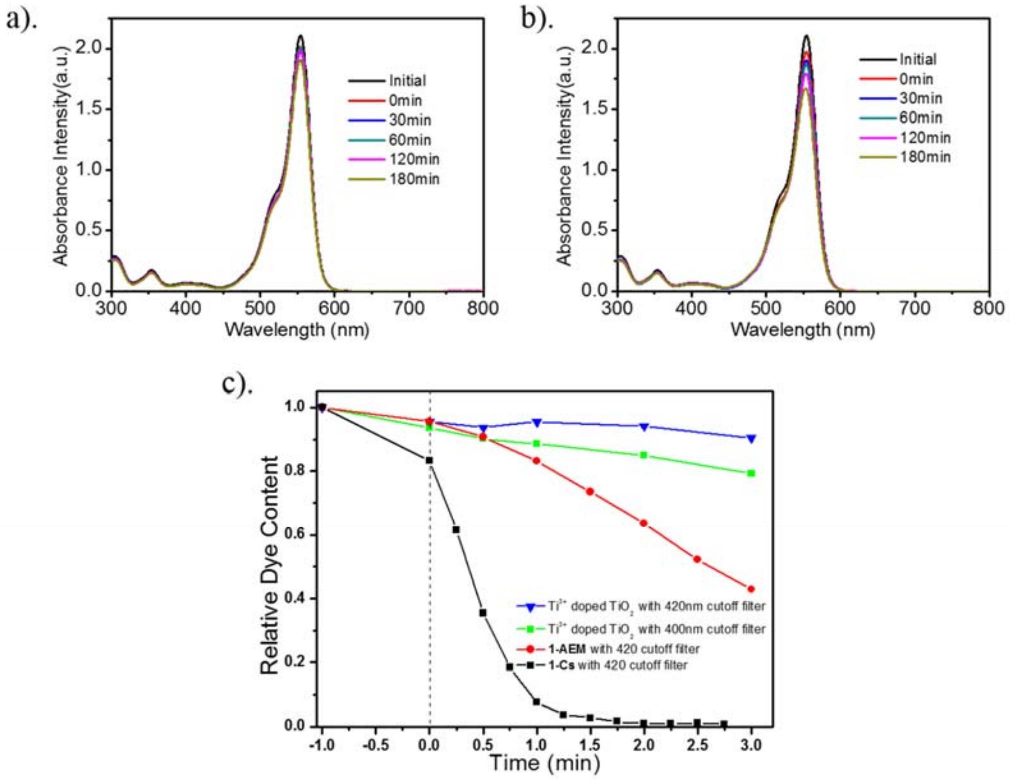

Figure 3.16 Photocatalytic activity of RhB^+ in different conditions with time. When the catalyst (Ti^{3+} doped TiO_2, **1-Cs** or **1-AEM**) was added to photocatalytic reaction, the solution was stirred in the dark for 1 hour to reach the adsorption equilibrium (from -1.0 to 0.0 hour period).

During the photocatalytic process of RhB^+ in the presence of **1-Cs**, the position of maximum absorbance peak of RhB^+ solution shifts from 554 nm to 504 nm after 1.5 hours of visible light irradiation (Figure 3.10a). Such dramatic hypsochromic shift of RhB^+ is attributed to a step-by-step diethylation of $-N(Et)_2$ on RhB^+. In open-framework chalcogenide, the anionic sulfur is balanced by the positively charged nitrogen of $-N(Et)_2$ group from RhB^+ after ion-exchange. In addition, S 3p orbitals make a great contribution to the valance band, which accumulates the photogenerated holes and induces the diethylation.

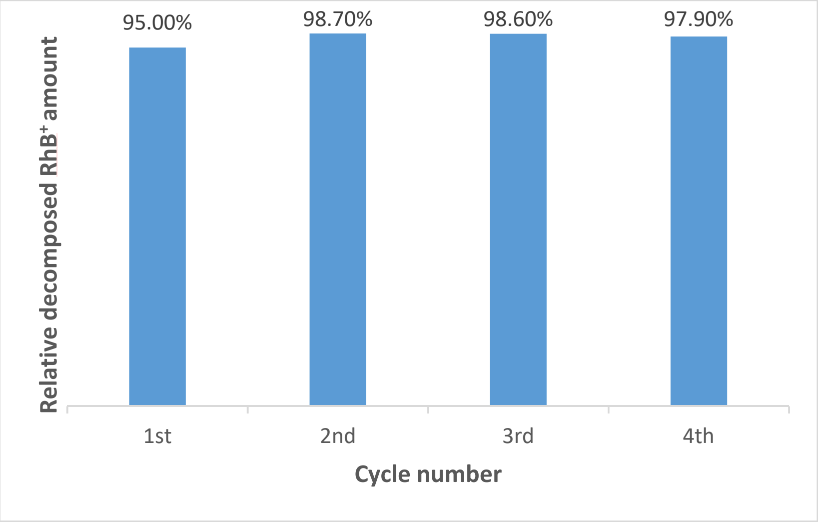

Figure 3.17 Recycling ability of **1-Cs** for the photocatalytic reaction of 10ppm RhB^+ aqueous solution.

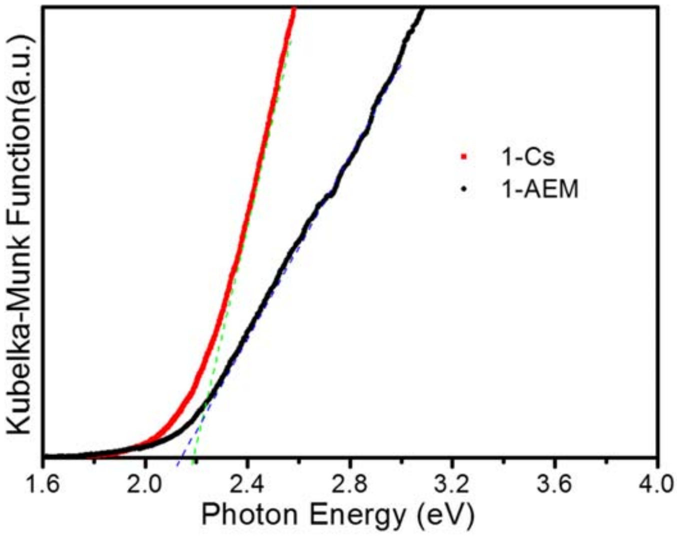

Figure 3.18 Normalized solid-state UV-vis absorption spectra of **1-AEM** and **1-Cs**.

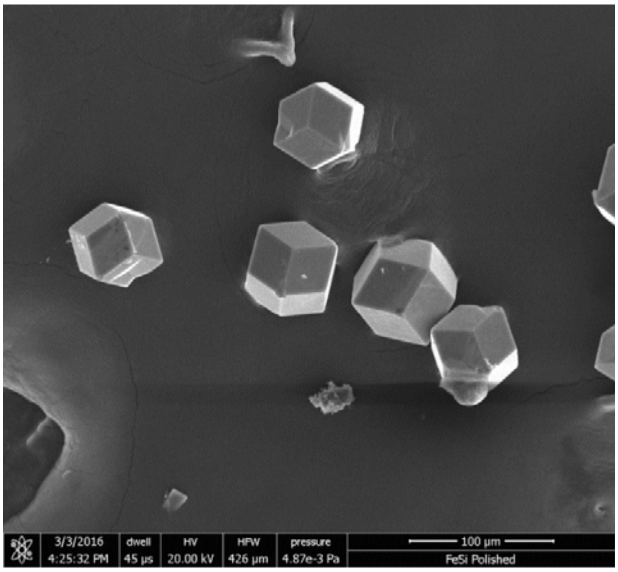

Figure 3.19 SEM image of **1-AEM**.

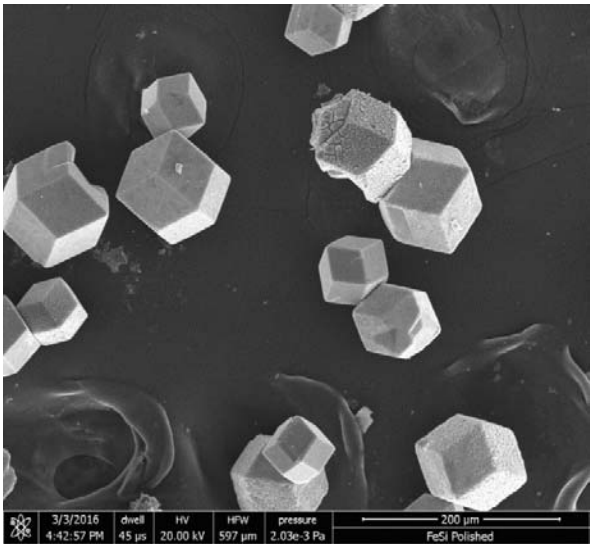

Figure 3.20 SEM image of **1-Cs**.

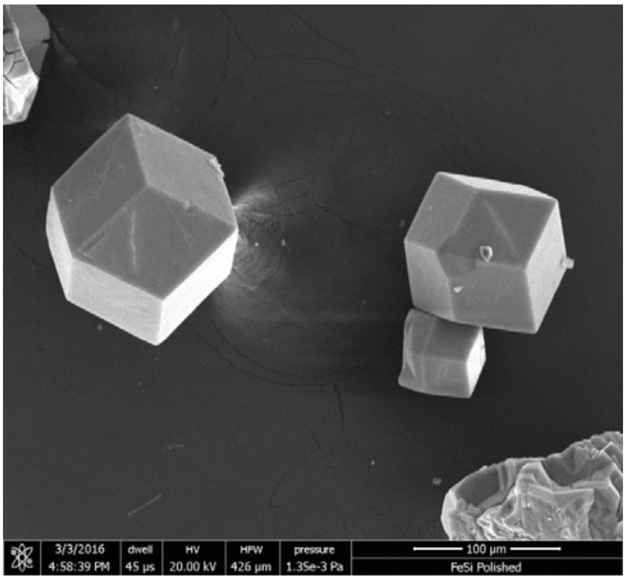

Figure 3.21 SEM image of **1-Cs** after photocatalytic reaction.

The dramatically different photocatalytic activity of RhB^+ and MO^- over **1-AEM** and **1-Cs** can be ascribed to the structural properties of the framework. As the framework is negatively charged, RhB^+ can diffuse into the pores through cation exchange with Cs^+ in

1-Cs and utilize the active sites inside the pore. In **1-AEM**, due to the bulky protonated AEM cations, the cation exchange between RhB^+ and AEM^+ is slow. Thus, less active sites are utilized and the photocatalytic rate is much slower than that over **1-Cs**. While for negatively charged MO^-, it cannot diffuse into the pores of framework due to electrostatic repulsion. As a result, only the active sites on the external surface of chalcogenide crystals can be used for photocatalytic reaction of anionic MO^-, resulting in the low photocatalytic rates in both **1-AEM** and **1-Cs**. Figure 3.22 shows the schematic illustration of different photocatalytic activities on **1-Cs**.

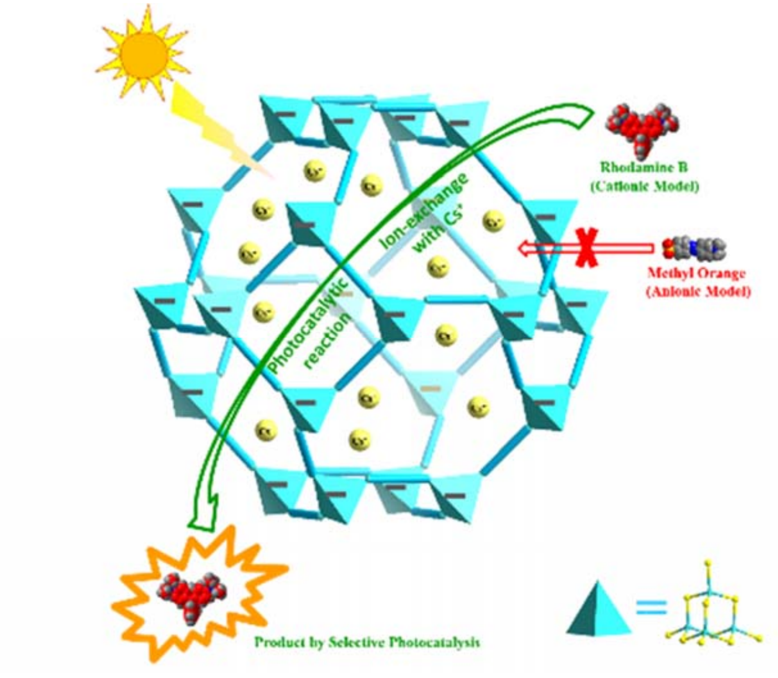

Figure 3.22 Schematic illustration of different photocatalytic activities on **1-Cs** towards cationic or anionic dye molecules.

3.4 Conclusion

In summary, this work demonstrates that open-framework chalcogenides can be used as efficient and selective porous photocatalytic materials for the decomposition of organic species in aqueous solutions. The porous chalcogenides, uniquely combining uniform porosity and semiconductivity, exhibit both size and charge selectivity in ion-exchange processes. By comparing photocatalytic activities of porous **1-Cs** and non-porous **1-AEM**, we show that the porosity contributes dramatically to the photocatalytic properties. This study demonstrates a promising platform for the development of charge and size selective photocatalytic materials.

3.5 References

(1) Zaera, F. *Chem. Soc. Rev.* **2013**, *42*, 2746.

(2) Kuo, C.-H.; Tang, Y.; Chou, L.-Y.; Sneed, B. T.; Brodsky, C. N.; Zhao, Z.; Tsung, C.-T. *J. Am. Chem. Soc.* **2012**, *134*, 14345.

(3) Na, K.; Choi, K. M.; Yaghi, O. M.; Somorjai, G. A. *Nano Lett.* **2014**, *14*, 5979.

(4) Christopher, P.; Linic, S. *J. Am. Chem. Soc.* **2008**, *130*, 11264.

(5) Csicsery, S. M. *Zeolites* **1984**, *4*, 202.

(6) Corma, A.; Fornes, V.; Pergher, S. B.; Maesen, Th. L. M.; Buglass, J. G. *Nature* **1998**, *396*, 353.

(7) Zhang, R.; Liu, N.; Lei, Z.; Chen, B. *Chem. Rev.*, **2016**, *116*, 3658.

(8) Fujishima, A.; Honda, K. *Nature* **1972**, *238*, 37.

(9) Han, Z.; Qiu, F.; Eisenberg, R.; Holland, P. L.; Krauss, T. D. *Science* **2012**, *338*, 1321.

(10) Zuo, F.; Wang, L.; Wu, T.; Zhang, Z.; Borchardt, D.; Feng, P. *J. Am. Chem. Soc.*, **2010**, *132*, 11856.

(11) Asahi, R.; Morikawa, T.; Irie, H.; Ohwaki, T. *Chem. Rev.* **2014**, *114*, 9824.

(12) Liu, J.; Liu, Y.; Liu, N.; Han, Y.; Zhang, X.; Huang, H.; Lifshitz, Y.; Lee, S.-T.; Zhong, J. Kang, Z. *Science* **2015**, *347*, 970.

(13) Liao, L.; Zhang, Q.; Su, Z.; Zhao, Z.; Wang, Y.; Li, Y.; Lu, X.; Wei, D.; Feng, G.; Yu, Q.; Cai, X.; Zhao, J.; Ren, Z.; Fang, H.; Robles-Hernandez, F.; Baldelli, S.; Bao, J. *Nature Nanotech.* **2014**, *9*, 69.

(14) Maeda, K.; Domen, K. *J. Phys. Chem. Lett.* **2010**, *1*, 2655.

(15) Gao, J.; Miao, J.; Li, P.-Z.; Teng, W. Y.; Yang, L.; Zhao, Y.; Liu, B.; Zhang, Q. *Chem. Commun.* **2014**, *50*, 3786.

(16) Kumar, S.; Surendar, T.; Baruah, A.; Shanker, V. *J. Mater. Chem. A* **2013**, ***1***, 5333.

(17) Iwashina, K.; Iwase, A.; Ng, Y. H.; Amal, R.; Kudo, A. *J. Am. Chem. Soc.* **2015**, *137*, 604.

(18) Asai, R.; Nemoto, H.; Jia, Q.; Saito, K.; Iwase, A.; Kudo, A. *Chem. Commun.* **2014**, ***50***, 2543.

(19) Ye, L.; Liu, J.; Jiang, Z.; Peng, T.; Zan, L. *Applied Catalysis B: Environmental* **2013**, *142*, 1.

(20) Gao, M.-Y.; Wang, F.; Gu, Z.-G.; Zhang, D.-X.; Zhang, L.; Zhang, J. *J. Am. Chem. Soc.* **2016**, *138*, 2556.

(21) Fang, W.-H.; Zhang, L.; Zhang, J. *J. Am. Chem. Soc.* **2016**, *138*, 7480.

(22) Liu, J.-X.; Gao, M.-Y.; Fang, W.-H.; Zhang, L.; Zhang, J. *Angew. Chem. Int. Ed.* **2016**, *55*, 5160.

(23) Gu, Z.-G.; Fu, H.; Neumann, T.; Xu, Z.-X.; Fu, W.-Q.; Wenzel, W.; Zhang, L.; Zhang, J.; Wöll, C. *ACS Nano* **2016**, *10*, 977.

(24) Jiang, Z.; Liu, J.; Gao, M.; Fan, X.; Zhang, L.; Zhang, J. *Adv. Mater.* **2017**, *29*, 1603369.

(25) Liu, M.; Wang, L.; Lu, G.; Yao, X.; Guo, L. *Energy Environ. Sci.* **2011**, *4*, 1372.

(26) Zhang, D.; Li, G.; Li, H.; Lu, Y. *Chem. –Asian J.* **2013**, *8*, 26.

(27) Zhang, K.; Guo, L. *Catal. Sci. Technol.* **2013**, *3*, 1672.

(28) Ikeda, S.; Kobayashi, H.; Ikoma, Y.; Harada, T.; Torimoto, T.; Ohtani, B.; Matsumura, M. *Phys. Chem. Chem. Phys.* **2007**, *9*, 6319.

(29) Zhan, S.; Chen, D.; Jiao, X.; Song, Y. *Chem. Commun.* **2007**, 2043.

(30) Zhang, G.; Choi, W.; Kim, S. H.; Hong, S. B. *J. Hazard. Mater.* **2011**, *188*, 198.

(31) Zhang, J.; Fu, W.; Xi, J.; He, H.; Zhao, S.; Lu, H.; Ji, Z. *J. Alloys Compd.* **2013**, *575*, 40.

(32) Bu, X.; Zheng, N.; Feng, P. *Chem. –Eur. J.* **2004**, *10*, 3356.

(33) Feng, P.; Bu, X.; Zheng, N. *Acc. Chem. Res.* **2005**, *38*, 293.

(34) Bu, X. H.; Zheng, N. F.; Li, Y. Q.; Feng, P. Y. *J. Am. Chem. Soc.* **2002**, *124*, 12646.

(35) Zheng, N. F.; Bu, X. H.; Feng, P. Y. *J. Am. Chem. Soc.* **2003**, *129*, 1138.

(36) Wu, T.; Khazhakyan, R.; Wang, L.; Bu, X.; Zheng, S.-T.; Chau, V.; Feng, P. *Angew. Chem. Int. Ed.* **2011**, *50*, 2536.

(37) Wang, L.; Wu, T.; Zuo, F.; Zhao, X.; Bu, X.; Wu, J.; Feng, P. *J. Am. Chem. Soc.* **2010**, *132*, 3283.

(38) Li, H. L.; Laine, A.; O'Keeffe, M.; Yaghi, O. M. *Science* **1999**, *283*, 1145.

(39) Lin, Q.; Bu, X.; Mao, C.; Zhao, X.; Sasan, K.; Feng, P. *J. Am. Chem. Soc.* **2015**, *137*, 6184.

(40) Zheng, N. F.; Bu, X. H.; Wang, B.; Feng, P. Y. *Science* **2002**, *298*, 2366.

(41) Vaqueiro, P.; Romero, M. L. *Chem. Commun.* **2007**, 3282.

(42) Vaqueiro, P.; Romero, M. L. *J. Am. Chem. Soc.* **2008**, *130*, 9630.

(43) Vaqueiro, P.; Romero, M. L.; Rowan, B. C.; Richards, B. S. *Chem. –Eur. J.* **2010**, *16*, 4462.

(44) Xiong, W.-W.; Miao, J.; Ye, K.; Wang, Y.; Liu, B.; Zhang, Q. *Angew Chem Int. Ed.* **2015**, *54*, 546.

(45) Nie, L.; Zhang, Y.; Ye, K.; Han, J.; Wang, Y.; Ganguly, R.; Li, Y.; Xu, R.; Yan, Q.; Zhang, Q. *J. Mater. Chem. A* **2015**, *3*, 19410.

(46) Xiong, W.-W.; Athersh, E. U.; Ng, Y. T.; Ding, J.; Wu, T.; Zhang, Q. *J. Am. Chem. Soc.* **2013**, *135*, 1256.

(47) Li, H. L.; Eddaoudi, M.; Laine, A.; O'Keeffe, M.; Yaghi, O. M. *J. Am. Chem. Soc.* **1999**, *121*, 6096.

(48) Yaghi, O. M.; Sun, Z.; Richardson, D. A.; Groy, T. L. *J. Am. Chem. Soc.* **1994**, *116*, 807.

(49) Li, H. L.; Kim, J.; Groy, T. L.; O'Keeffe, M.; Yaghi, O. M. *J. Am. Chem. Soc.* **2001**, *123*, 4867.

(50) Lu, J; Li, X.-X.; Qi, Y.-J.; Niu, P.-P.; Zheng, S.-T. *Angew. Chem. Int. Ed.* **2016**, *55*, 13793.

(51) Li, Z.; Li, X.-X.; Yang, T.; Cai, Z.-W.; Zheng. S.-T. *Angew. Chem. Int. Ed.* **2017**, *56*, 2664.

(52) Sun, Y.-Q.; Wan, F.; Li, X.-X.; Lin, J.; Wu, T.; Zheng, S.-T.; Bu, X.; *Chem. Commun.* **2016**, *52*, 10125.

(53) Zhang, S.-Y.; Shi, W.; Cheng, P.; Zaworotko, M. J. *J. Am. Chem. Soc.* **2015**, *137*, 12203.

(54) Zhou, J.; Li, H.; Zhang, H.; Li, H.; Shi, W.; Cheng, P. *Adv. Mater.* **2015**, *27*, 7072.

(55) Lin, J.; Dong, Y.; Zhang, Q.; Hu, D.; Li, N.; Wang, L.; Liu, Y.; Wu, T. *Angew. Chem. Int. Ed.* **2015**, *54*, 5103.

(56) Lin, Y.; Massa, W.; Dehnen, S. *J. Am. Chem. Soc.* **2012**, *134*, 4497.

(57) Nie, L.; Zhang, Y.; Ye, K.; Han, J.; Wang, Y.; Rakesh, G.; Li, Y.; Xu, R.; Yan, Q.; Zhang, Q. *J. Mater. Chem. A* **2015**, *3*, 19410.

(58) Zhang, X.; Wang, Q.; Ma, Z.; He, J.; Wang, Z.; Zheng, C.; Lin, J.; Huang, F. *Inorg. Chem.* **2015**, *54*, 5301.

(59) Biswas, K.; Chung, I.; Song, J.-H.; Malliakas, C. D.; Freeman, A. J.; Kanatzidis, M. G. *Inorg. Chem.* **2013**, *52*, 5657.

(60) Ding, N.; Kanatzidis, M. G. *Nat. Chem.* **2010**, *2*, 187.

(61) Manos, M. J.; Chrissafis, K.; Kanatzidis, M. G. *J. Am. Chem. Soc.* **2006**, *128*, 8875.

(62) Manos, M. J.; Iyer, R. G.; Quarez, E.; Liao, J. H.; Kanatzidis, M. G. *Angew. Chem. Int. Ed.* **2005**, *44*, 3552.

(63) Tsamourtzi, K.; Song, J.-H.; Bakas, T.; Freeman, A. J.; Trikalitis, P. N.; Kanatzidis, M. G. *Inorg. Chem.* **2008**, *47*, 11920.

(64) Tanaka, A.; Hashimoto, K.; Kominami, H. *J. Am. Chem. Soc.* **2014**, *136*, 586.

(65) Miseki, Y.; Kusama, H; Sugihara, H.; Sayama, K. *J. Phys. Chem. Lett.* **2010**, *1*, 1196.

(66) Pan, X.; Yang, M.-Q.; Fu, X.; Zhang, N.; Xu, Y.-J. *Nanoscale*, **2013**, *5*, 3601.

（67） Wang, M.; Ioccozia, J.; Sun, L.; Lin, C.; Lin, Z.; *Energy Environ. Sci.* **2014**, *7*, 2182.

（68） Zheng, N. F.; Bu, X. H.; Vu, H.; Feng, P. Y. *Angew. Chem. Int. Ed.* **2005**, *44*, 5299.

Chapter 4 Cation-Exchanged Zeolitic Chalcogenides for CO_2 Adsorption

4.1 Introduction

The increasing level of atmospheric CO_2, largely correlated to the combustion of fossil fuels, is currently a very pressing environmental concern.[1] Among the few and yet viable strategies that can deal with the emission of CO_2 is carbon capture and storage (CCS).[2] Currently, the most mature and commercially available technology for CCS is 'wet scrubbing' methods based on chemical reactions between CO_2 and amines in aqueous solutions.[3] Though this technology is straightforward to apply, the high energy demand for the regeneration of the amines is a major problem.[4] Alternatively, capture of CO_2 based on porous solid adsorbents has the potential to perform such capture at a much reduced energy penalty and has therefore received much attention in recent years.[5]

Many different porous solid materials have been investigated, including oxide-based zeolites,[6-9] aluminophosphates,[10-12] porous carbons,[13, 14] porous organics,[15, 16] and metal-organic frameworks (MOFs).[17-22] Generally, the practical CO_2 adsorption requires the sorbents to possess large uptake capacity, high selectivity, facile recyclability, and also the excellent stability (especially when exposed to water vapor). Unfortunately, it seems that the 'perfect' sorbents that can satisfy all the requirements still remain elusive. For example, the well-developed zeolite 13x is very stable and has a high selectivity but its uptake capacity is relatively low.[23] On the contrary, MOF-74s, a very popular series of MOFs, have the record-high uptake capacity and a high selectivity of CO_2 over N_2.[24] However, the presence of water vapor can reduce their gas uptake capacity significantly and can degrade or even destroy the crystal structure, restricting their practical use.[25, 26] It is thus very important to search new sorbent materials.

Recently, chalcogenide porous materials including chalcogels and zeolitic chalcogenides have attracted a widespread attention in the field of CO_2 adsorption because of their inorganic frameworks and the soft surface of electron-rich chalcogenide atoms.[27-30] The polarizability of porous chalcogenides is therefore much higher than that of oxide frameworks and porous organics, rendering a strong affinity towards highly polarizable species, such as CO_2 (polarizability (α): α (CO_2) = 2.51 cm^{-3}), based on the hard and soft acid-base theory (HSAB).[31, 32] For examples, Kanatzidis et al. found that mesoporous germanium-rich chalcogenide frameworks exhibited excellent selectivity for separating hydrogen from carbon dioxide and methane.[33] We also found that the Cs^+-exchanged form of a zeolitic chalcogenide analogue (CPM-120) showed CO_2 adsorption with high capacity and affinity (98 cm^3/g at 273 K, isosteric heat of 40.05 $kJ \cdot mol^{-1}$).[30] These results demonstrate that porous chalcogenides have the potential to act as excellent CO_2 adsorbing materials that integrate the stability with high selectivity for CO_2 over other gases.

Here, we focus our study on the charge-balancing cations in the channel of the frameworks. We show that this is an effective strategy to improve the CO_2 adsorption. In fact, the impact of charge-balancing inorganic cations on gas adsorption is known in both zeolites and MOFs.[34-37] However, this strategy has not been realized in porous chalcogenides, which is probably due to the rather limited exchange (highly selective for ‘soft’ cations) in porous chalcogenides arising from their ‘soft’ character.[38] Recently, targeting the nuclear waste remediation, we developed a strategy based on amine-Cs-K ion exchange and reverse K-Cs ion exchange in 3D zeotype chalcogenides (UCR-20, denoted as RWY in the database of zeolite structures).[39] In this work, we systematically synthesized a series of cation-exchanged zeolitic chalcogenides (M@RWY) and extensively studied their capacity and selectivity for CO_2 capture. The results showed that the K^+-exchanged RWY had the best performance for CO_2 adsorption.

4.2 Experimental Section

4.2.1 Synthesis

The pre-ion-exchanged solid samples of UCR-20-GaGeS ($[Ga_xGe_{4-x}S_8]^{x-}$, also named as PA@RWY) were synthesized according to the literature method.[38]

4.2.2 Stepwise Ion-Exchange Strategy

The stepwise ion-exchange strategy consists of following steps.

Step 1: The protonated amines (PA) were firstly exchanged out by ‘soft’ Cs^+. Typically, 500 mg of pristine RWY crystals are soaked in 100 mL CsCl aqueous solution (1 M) in a glass vial, which was sealed and subsequently put in an 85ºC oven. The CsCl solution was refreshed once during treatment. After 48 h, the crystals (named as Cs@RWY) were washed by deionized water and ethanol for several times, and dried in vacuum. The process can be described as follows:

$$\mathrm{Cs^{+} + PA@RWY \xrightarrow{85°C} Cs@RWY + PA^{+}}$$

$$\mathrm{(PA = \ protonated\ amines)} \qquad (1)$$

Step 2A: 100 mg of Cs@RWY crystals were immersed into 100 mL of RbCl solution (1 M) at room temperature. The solution was refreshed once with a total time of around 48 h to remove Cs^{+} ions in the channels of RWY. Subsequently, the samples (named as Rb@RWY) were washed by deionized water and ethanol, and dried in vacuum oven. The ion-exchange process can be described as follows:

$$\mathrm{Rb^{+} + Cs@RWY \overset{RT}{\rightarrow} Rb@RWY + Cs^{+}} \qquad (2A)$$

Step 2B: 100 mg of Cs@RWY crystals were immersed into 100 mL of KCl solution (2 M) at room temperature. The solution was refreshed once with a total time of around 48 h to remove Cs^{+} ions in the channels of RWY. Subsequently, the crystals (named as K@RWY) were washed by deionized water and ethanol for several times, and dried in vacuum oven. The ion-exchange process was expressed as:

$$\mathrm{K^{+} + Cs@RWY \overset{RT}{\rightarrow} K@RWY + Cs^{+}} \qquad (2B)$$

Step 3: 100 mg of K@RWY crystals were immersed into 100 mL of MCl_x solution (M = Na^{+}, Mg^{2+}, Ca^{2+}, Sr^{2+}) at room temperature. The solution was refreshed twice with a total time of around 48 h to remove K^{+} ions in the channels of RWY completely. Subsequently, the samples (named as M@RWY) were washed by deionized water and ethanol, and dried in vacuum oven. The ion-exchange process was expressed as:

$$\mathrm{M^{x+} + K@RWY \overset{RT}{\rightarrow} M@RWY + K^{+}} \qquad (3)$$

4.2.3 Gas Adsorption Experiments

The CO_2 and N_2 adsorption isotherms of cation-exchanged samples were recorded using a Micromeritics ASAP 2020 Physisorption Analyzer. The cation-exchanged samples were dried in the vacuum oven for 4 h and were further degassed for 10 h at 373 K. CO_2 adsorption isotherms were recorded at 273 K, 298 K, 313 K, and the temperature of experiments was controlled by a Dewar flask.

4.2.4 Evaluation of CO_2 Capture Performance

To evaluate the CO_2 capture performance of the ion-exchanged zeolitic RWY materials, measured CO_2 and N_2 isotherms were fit with adsorption models. Simple adsorption models, such as the single-site Langmuir (SSL) model, often do not adequately describe CO_2 adsorption on heterogeneous surfaces. As such, a dual-site Langmuir (DSL) model was employed to describe the CO_2 adsorption of ion-exchanged RWY zeolite materials over the entire pressure range:

$$N = N_A + N_B = \frac{N_{A,sat} k_A p}{1 + k_A p} + \frac{N_{B,sat} k_B p}{1 + k_B p} \tag{5}$$

where N is the quantity adsorbed, p is the pressure of bulk gas at equilibrium with adsorbed phase, $N_{A,sat}$ and $N_{B,sat}$ are the saturation loadings for sites A and B, and k_A and k_B are the Langmuir parameters for sites A and B, respectively.

To estimate the CO_2/N_2 separation performance of Cs@RWY under conditions relevant to CO_2 capture, ideal adsorbed solution theory (IAST) was used to calculate the selectivity of CO_2 over N_2.[40] The detailed methodology for calculating the amount of CO_2

and N_2 adsorption from a mixture is described elsewhere.[41] The accuracy of the IAST procedure has already been established for adsorption of a wide variety of gas mixtures in many different zeolites. The adsorption selectivity is defined as:

$$selectivity = \frac{q_A / q_B}{p_A / p_B} \qquad (6)$$

where q_i is the uptake quantity and p_i is the partial pressure of component i.

The isosteric heats of adsorption for CO_2 were calculated using the DSL isotherm fits at 273 K and 298 K. The isosteric heat of CO_2 adsorption was calculated by following the Clausius-Clapeyron equation.

4.3 Results and Discussion

4.3.1 Preparation of Cation-Exchanged Samples through Stepwise Ion-Exchange Strategy

The structure of RWY is constructed from supertetrahedral T2 ($[Ga_xGe_{4-x}S_{10}]$) clusters with sodalite topology by treating the clusters as nodes (Figure S1). Disordered positively-charged amines, protonated tris (2-dimethyl- aminoethyl) amine (TAEA), located in the channels. The pristine zeolitic chalcogenides (amine@RWY) showed negligible gas adsorption due to the pore blockage by the bulky templating amines.

To investigate the effect of the charge-balancing cations on the gas adsorption properties of the porous zeolitic chalcogenides, the protonated amine in pristine RWY was post-synthetically exchanged with Cs^+, Rb^+, K^+, Na^+, Sr^{2+}, Ca^{2+}, and Mg^{2+}, which afforded

Cs@RWY, Rb@RWY, K@RWY, Na@RWY, Sr@RWY, Ca@RWY, and Mg@RWY, respectively. The experiments were performed by immersing the crystals in the aqueous solutions of various hydrated metal salts. Notably, extra ion-exchange processes are needed in order to make more complete exchange except with the use of Cs^+. This could be because RWY framework with 'soft' character has strong affinity towards 'soft' cations (e.g., Cs^+) and weak affinity towards 'hard' cations (e.g., K^+). For example, we can obtain nearly fully Cs^+ activated samples (Cs@RWY) through a single-step ion-exchange process (The exchange degree is calculated by the reduction of protonated amines based on the content of N from CHN elemental analysis, as shown in Table 4.1). In comparison, only 61% of organic amines can be directly exchanged out by K^+ and 48% by Na^+.[38] Actually, the Cs^+ ions in Cs@RWY can be nearly fully expelled from RWY with excess K^+ but not with Na^+ due to the relatively small polarizability of Na^+. The fully Na^+ activated samples (Na@RWY) could only be obtained from K@RWY with two successive steps as Cs@RWY→K@RWY→Na@RWY, shown in Scheme 4.1.

Table 4.1 Elemental analyses of pristine RWY, Cs@RWY, Rb@RWY and K@RWY.

Elements (wt.)	N (%)	C (%)	H (%)
Pristine RWY	10.33	15.55	3.839
Cs@RWY	0.391	0.935	2.047
Rb@RWY	0.000	0.657	2.231
K@RWY	0.000	0.439	2.695

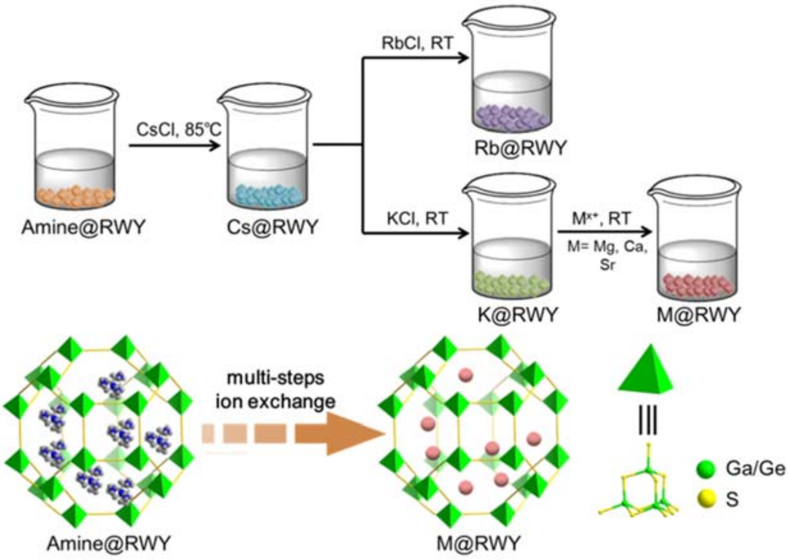

Scheme 4.1 Stepwise ion-exchange processes for various cation-exchanged samples.

Through the stepwise ion-exchange processes as shown in Scheme 4.1, a series of cation-exchanged samples were successfully synthesized including Cs@RWY, Rb@RWY, K@RWY, Na@RWY, Mg@RWY, Ca@RWY, and Sr@RWY. The ion-exchange processes were demonstrated to be basically complete based on the fact that EDS experiments cannot detect any residual of the original cations. The contents of Cs in Rb@RWY and K@RWY were further analyzed by ICP-MS by digesting the samples. The results indicated that the exchange degrees for Rb@RWY and K@RWY were 93.8% and 97.3%, respectively. The PXRD peaks of the pristine samples and as-exchanged samples can be well indexed with those in the simulated one, indicating that all the samples have the pure phase and the exchanged samples maintained the parent framework after ion-exchange processes (Figure 4.1). The unit cells from SCXRD also indicated the shrink of the lattice from pristine RWY to Cs@RWY, Rb@RWY, to K@RWY, following the order of the balanced species' size. Notably, the diffraction peaks for the divalent metal cation exchanged samples have an obvious shift towards larger angle, compared with those of other samples. This is reasonable because by replacing monovalent cations with divalent cations, the amount of cations as the charge-balancing species in the framework is reduced by half. The higher charge and smaller number of the cations are responsible for the shrinkage of the crystal lattice. Unfortunately, due to the bad quality of the divalent-cations-exchanged crystals, it cannot be demonstrated directly by SCXRD analysis.

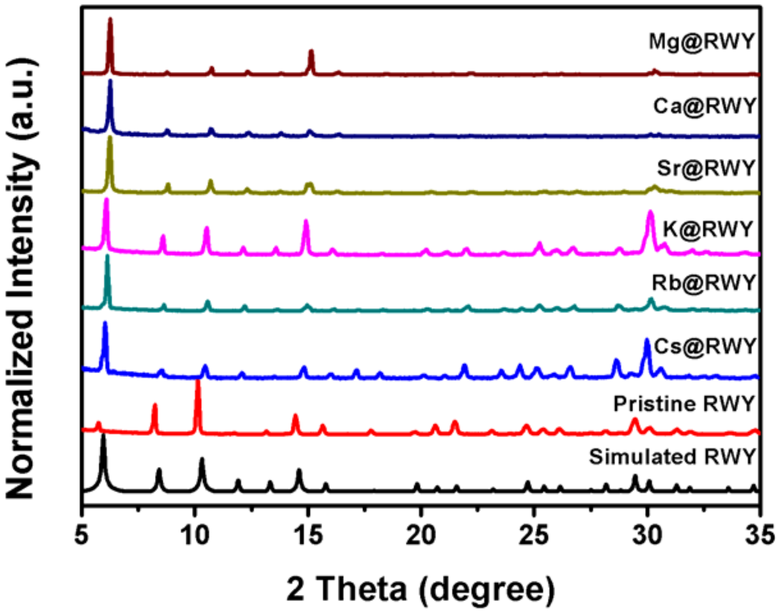

Figure 4.1 PXRD patterns of the various cation-exchanged samples.

4.3.2 Surface Area Characterizations

There exists a large amount of water molecules in the channels of ion-exchanged samples including Cs@RWY and K@RWY, which need to be removed by degas process before the gas adsorption analysis. The degas processes were typically performed at 373 K for 10 h. PXRD measurements indicated that the samples of Cs@RWY, Rb@RWY, and K@RWY could retain the pristine structure after degas treatment but Na@RWY, Mg@RWY, Ca@RWY, and Sr@RWY could not retain the crystallinity (even at 313 K) (Figure 4.2 and 4.3). As such, the samples of Na@RWY, Mg@RWY, Ca@RWY, and Sr@RWY didn't exhibit porosity. For the situation in Ca@RWY, Sr@RWY, and Mg@RWY, the instability is perhaps due to the larger void spaces in these samples induced by the greatly reduced amount of the charge-balancing cations (Mg^{2+}, Ca^{2+}, and Sr^{2+}), compared with those in Cs@RWY, Rb@RWY, and K@RWY. For Na@RWY, it may be related to the weak interaction between Na^+ and the framework and the precise reason still requires further study. As a result, in this work, only the gas adsorption properties of the latter ones were characterized and studied.

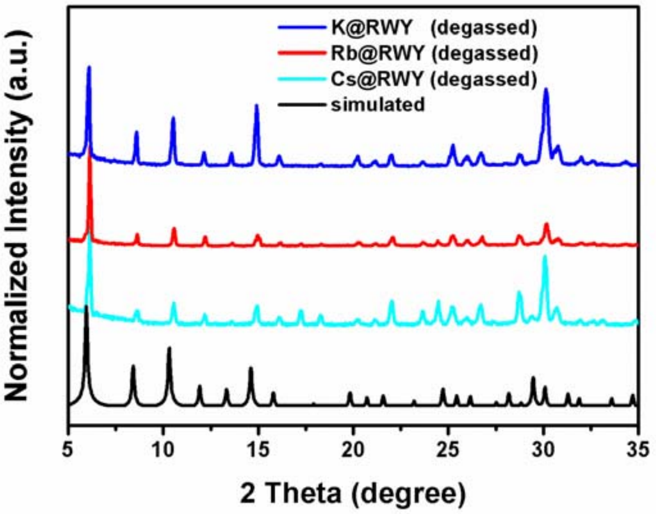

Figure 4.2 Powder X-ray diffraction patterns for Cs@RWY, Rb@RWY, and K@RWY after dried in the vacuum oven for 10 h at 373 K.

To investigate the surface areas of the activated samples, N_2 adsorption measurements were performed at 77 K. As shown in Figure 4.4a, all the samples were found to exhibit typical type-I adsorption isotherms and steep N_2 uptake in the low-pressure regions ($P / P_0 < 0.05$), indicating the microporosity of these materials. The Brunauer–Emmett– Teller (BET) surface areas of Cs@RWY, Rb@RWY, and K@RWY were calculated to be 526, 638, and 716 m^2/g, respectively. The pore volume was found to increase from 0.277, 0.363 to 0.381 $cc \cdot g^{-1}$, respectively. The pore size distributions, as calculated by Horvath-Kawazoe method, indicated that the exchanged cations had little effect on the pore size (Figure 4.4b). The median pore size of all the exchanged samples was found to be nearly the same with the value of 0.62 nm. As a result, the increase of the BET surface areas from Cs@RWY to K@RWY is believed to be mainly caused by the decrease of the formula weight and cation sizes rather than the increase of the pore size.

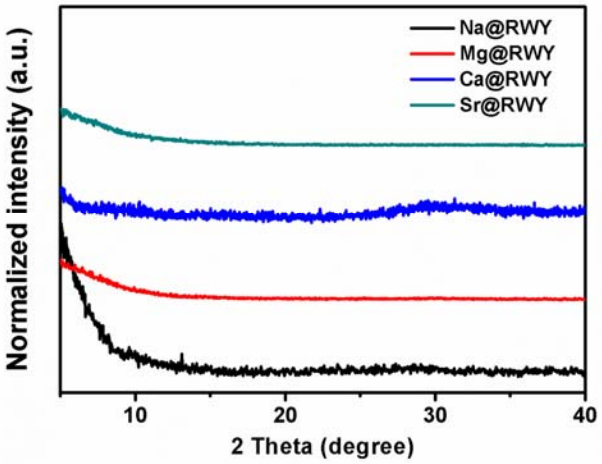

Figure 4.3 Powder X-ray diffraction patterns for Na@RWY, Mg@RWY, Ca@RWY, and Sr@RWY after dried in the vacuum oven for 10 h at 373 K.

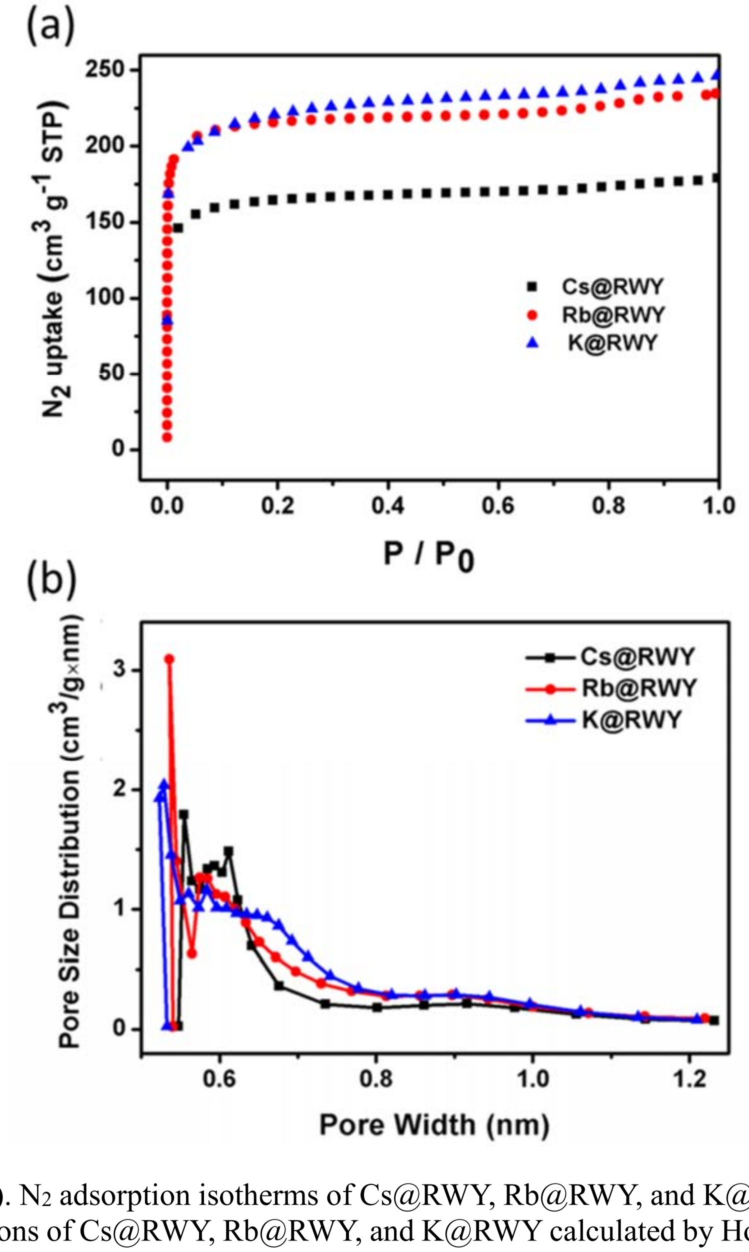

Figure 4.4 (a). N$_2$ adsorption isotherms of Cs@RWY, Rb@RWY, and K@RWY; (b). Pore size distributions of Cs@RWY, Rb@RWY, and K@RWY calculated by Horvath-Kawazoe method.

4.3.3 Selectivity of CO_2 Adsorption

The CO_2 adsorption isotherms at 273 K, 298 K, and 313 K for Cs@RWY, Rb@RWY, and K@RWY are shown in Figure 4.5, 4.6 and 4.7. The relatively high uptake is observed in all the samples, with the order following Cs@RWY < Rb@RWY < K@RWY. K@RWY exhibits the highest capacity of 86.7 cm^3/g (3.87 mmol/g) at 313 K and 1 atm. Due to the difference in the formula weight of the as-exchanged samples, it is thus more reasonable to compare the volumetric capacity. The calculated results revealed that the volumetric capacity of all the samples still exhibited the increase trend from Cs@RWY to K@RWY, indicating the stronger affinity towards CO_2 for K@RWY. Notably, the previously studied porous chalcogenides (mostly chalcogels) have a high selectivity for CO_2 capture. However, one issue for those chalcogels is their small capacity for CO_2 uptake (< 1 mmol/g), as shown in Table 4.2. The uptake capacity reported here represents the highest value among chalcogenides, which is also higher than commercialized oxide zeolite (NaX). The volumetric uptake value is also comparable to the MOF-74 series.

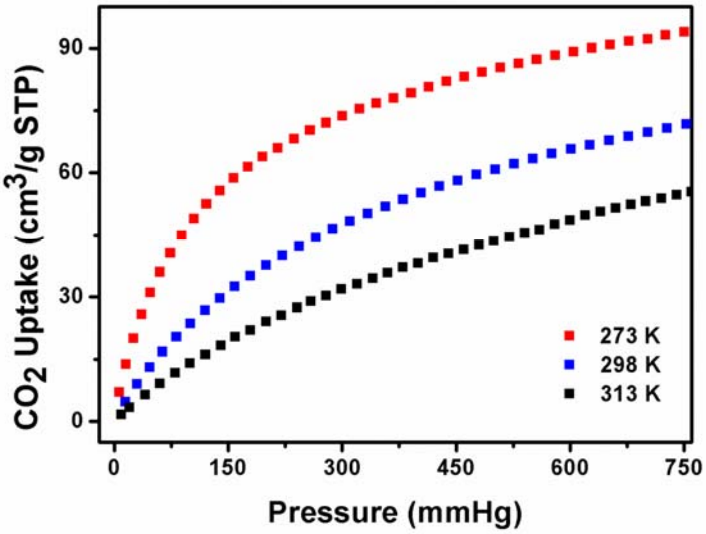

Figure 4.5 CO_2 adsorption isotherm of Cs@RWY at 273 K, 298 K, and 313 K.

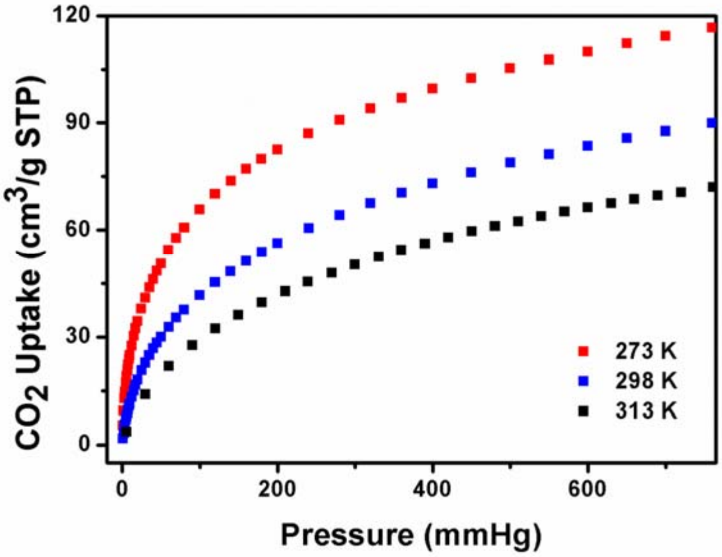

Figure 4.6 CO_2 adsorption isotherm of Rb@RWY at 273 K, 298 K, and 313 K.

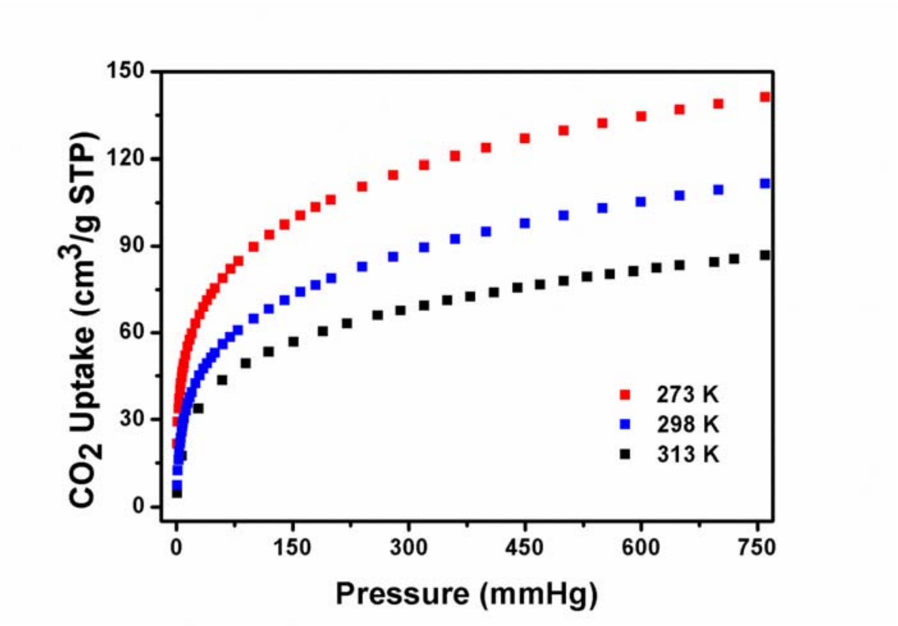

Figure 4.7 CO_2 adsorption isotherm of K@RWY at 273 K, 298 K, and 313 K.

Table 4.2 Comparison of CO_2 adsorption capacity and IAST-calculated selectivity for 15/85 % CO_2/N_2 mixture in different porous materials at 298 K.[23, 24, 28, 42-46]

Materials	Adsorption enthalpy (kJ / mol)	CO_2 uptake (mmol / g)	CO_2 uptake (mmol / cm^3)	BET surface (m^2 /g)	Selectivity
MOF-74 series	37-47	5.36-7.81	6.60-7.23	816-1495	182[b]
Cu-BTC	30	4.1	3.67	1571	~20
MoS_x aerogel	13-15	0.7[a]	N.A.	115-370	N.A.
$CoMo_3S_{13}$ chalcogel	6-13	0.9[a]	2.727[a]	569	N.A.
Zeolite NaX	31-37	2.72	1.52	183	146[b]
Zeolite 13X	40	4.70	3.24	726	30.4
Cs@RWY	30.2-32.1	3.21	5.84	526	180[a]
Rb@RWY	30.5-35.1	4.00	6.45	656	E.H.
K@RWY	35.0-41.1	4.98	6.86	716	E.H.

[a] Data collected at 273 K. [b] 296 K and 1 atm. N.A. = not available. E.H. = extraordinarily high

To better understand the affinities towards CO_2 of the as-exchanged samples, the adsorption heat (Q_{st}) was calculated based on the Clausius-Clapeyron equation. All the adsorption isotherms were well fitted based on the dual-site Langmuir model (Table 4.3, 4.4 and 4.5). This could be ascribed to be the existence of two kinds of surface sulfur sites in a T2 unit, that is, four core-sulfur sites and six edge-sulfur sites. It was found that the low coverage of the Q_{st} values increased from Cs@RWY (30.2 – 32.1 kJ mol^{-1}) to K@RWY (35.0 – 41.1 kJ mol^{-1}) (Figure 4.8 and Table 4.2). The affinity gap of the exchanged samples could be explained as follows. For cation-exchanged RWY, even though the location of the charge-balancing cations could not be determined by single-crystal structure analysis, they should be present near the surface of framework due to the electrostatic interactions, similar to the situation in oxide zeolites. K^+, with higher charge-to-volume ratio than Rb^+ and Cs^+, may have stronger interaction with CO_2, which contribute to its higher Q_{st}. Also, the adsorption mechanism in these materials should include the strong interaction of 'soft' CO_2 and 'soft' exposed framework sulfur sites. For such interactions, the large near-surface Cs^+ sites provide greater steric hindrance for the access of CO_2 to the sulfur sites.

Table 4.3 Fitting parameters for gas adsorption at 273 K.

	gas	$N_{i,A,sat}$ cm^3 g^{-1}	$K_{i,A}$ mmHg^{-1}	$N_{i,B,sat}$ cm^3 g^{-1}	$K_{i,B}$ mmHg^{-1}	R^2
Cs@RWY	CO_2	81.68	1.173×10^{-2}	71.20	5.384×10^{-4}	0.99997
Rb@RWY	CO_2	42.08	9.358×10^{-2}	84.31	4.660×10^{-3}	0.99954
K@RWY	CO_2	107.24	4.540×10^{-3}	56.21	0.45243	0.9985
Cs@RWY	N_2	2.94	6.82×10^{-5}			0.99998

Table 4.4 Fitting parameters for CO_2 adsorption at 298 K.

	$N_{i,A,sat}$ cm^3 g^{-1}	$K_{i,A}$ mmHg^{-1}	$N_{i,B,sat}$ cm^3 g^{-1}	$K_{i,B}$ mmHg^{-1}	R^2
Cs@RWY	29.35	6.820×10^{-3}	87.93	1.530×10^{-3}	0.99999
Rb@RWY	85.31	2.02×10^{-3}	35.25	2.333×10^{-2}	0.99998
K@RWY	46.83	0.1503	96.52	2.63×10^{-3}	0.99965

Table 4.5 Fitting parameters for CO_2 adsorption at 313 K.

	$N_{i,A,sat}$ cm^3 g^{-1}	$K_{i,A}$ mmHg^{-1}	$N_{i,B,sat}$ cm^3 g^{-1}	$K_{i,B}$ mmHg^{-1}	R^2
Cs@RWY	521.05	5.469×10^{-5}	50.97	2.810×10^{-3}	0.99989
Rb@RWY	27.28	2.01×10^{-2}	88.52	1.450×10^{-3}	0.99998
K@RWY	75.06	1.68×10^{-3}	44.826	7.772×10^{-2}	0.99983

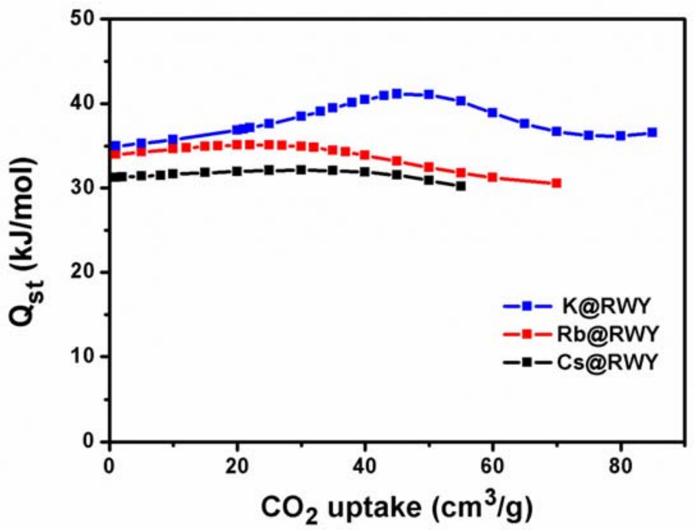

Figure 4.8 Adsorption heats of Cs@RWY, Rb@RWY, and K@RWY.

Due to the high uptake and strong interaction for CO_2 adsorption, we were motivated to test the CO_2/N_2 selectivity of the samples. Remarkably, the values of the CO_2/N_2

selectivity are impossible to determine validly under ambient temperature (298 K) because the N_2 adsorption of all three samples is essentially zero despite of the various efforts we have made, indicative of extraordinarily high selectivity. The negligible adsorption of N_2 persists for K^+ and Rb^+ samples even down to 273K. Eventually we were able to achieve a measurable, yet very low amount of N_2 adsorption of Cs@RWY (Figure 4.9). The adsorption isotherms of CO_2 and N_2 at 273 K for Cs@RWY were shown in Figure 4.10, in which a high amount of CO_2 uptake and a very small amount of N_2 uptake were observed, indicating a high CO_2/N_2 selectivity. The ideal adsorbed solution theory (IAST), a widely adopted method to predict mixed isotherm from pure gas isotherm, was then employed to determine the selectivity of CO_2 over N_2. The predicted selectivity in a mixture of 15 % CO_2 and 85 % N_2 in molar ratio under different pressure is shown in the inset of Figure 4.10. The value is found to be around 180, higher than the commercialized oxide zeolite materials and approximately equal to MOF-74. All these results demonstrated the extraordinarily high CO_2/N_2 selectivity of cation-exchanged zeolitic chalcogenide materials.

To test the recyclability of CO_2 adsorption of K@RWY, which exhibited the highest CO_2 uptake and the largest adsorption heat Q_{st} among these samples, the CO_2 gas adsorption isotherms were measured for eight cycles at 273 K and 1 atm. Between each cycle, the adsorbed CO_2 was readily removed under dynamic vacuum treatment for 2 h at room temperature. The results demonstrated that the uptake capacity was maintained over eight cycles, indicating a complete regeneration of this material through a facile process (Figure 4.12a).

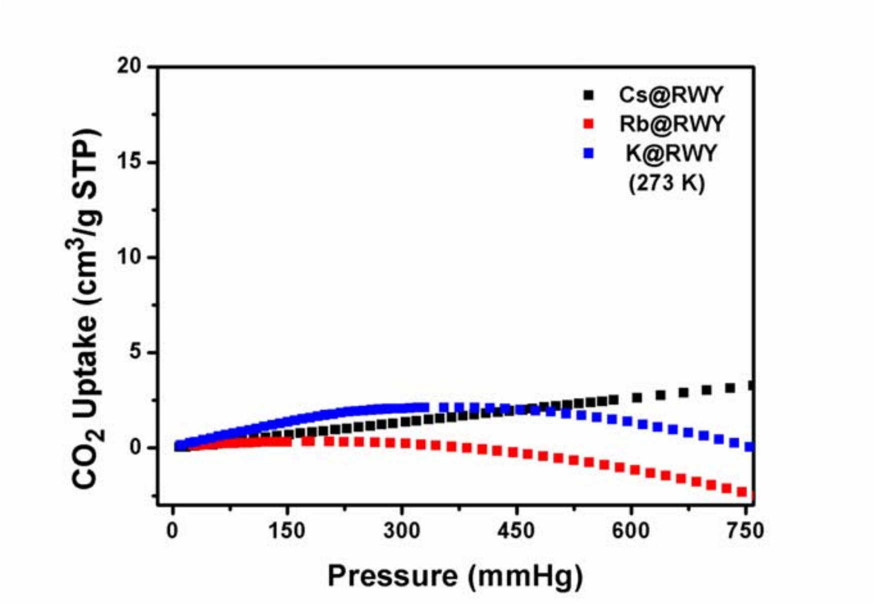

Figure 4.9 N_2 adsorption isotherms of Cs@RWY, Rb@RWY, and K@RWY at 273 K.

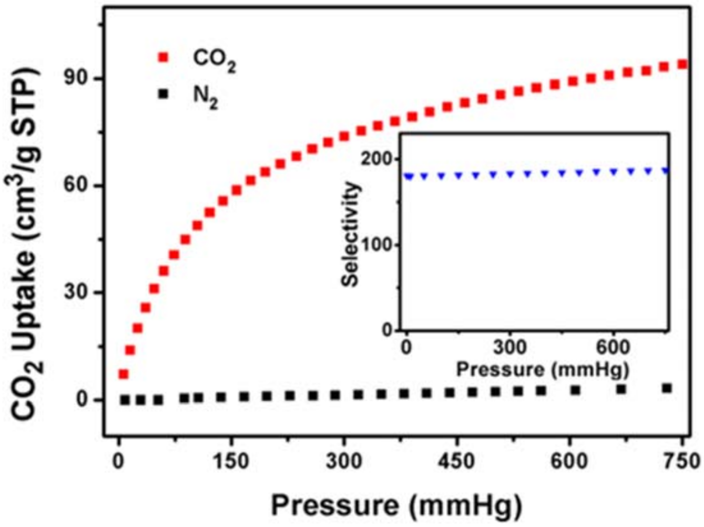

Figure 4.10 Adsorption isotherms of Cs@RWY for CO_2 and N_2 at 273 K. Inset shows the CO_2/N_2 selectivity calculated by IAST theory.

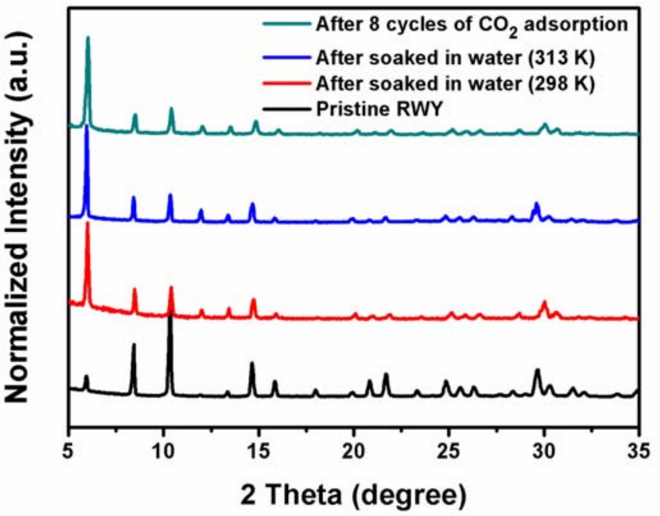

Figure 4.11 The powder X-ray diffraction patterns for K@RWY after 8 cycles adsorption and after being soaked in water at 298 K and 313 K for 24 h.

The cation-exchanged zeolitic chalcogenides do have a strong tolerance towards water based on the fact that all these samples were prepared in aqueous solutions. To further confirm the high stability, the K@RWY samples were directly soaked in water at RT and 313 K (40° C) for 24 hours (Figure 4.11). The results shown in Figure 4.12b indicated that K@RWY still maintained a very high capacity after the regeneration process. In comparison, even under a less harsh condition, the CO_2 adsorption capacity of regenerated Mg-MOF-74 decreased significantly.[26]

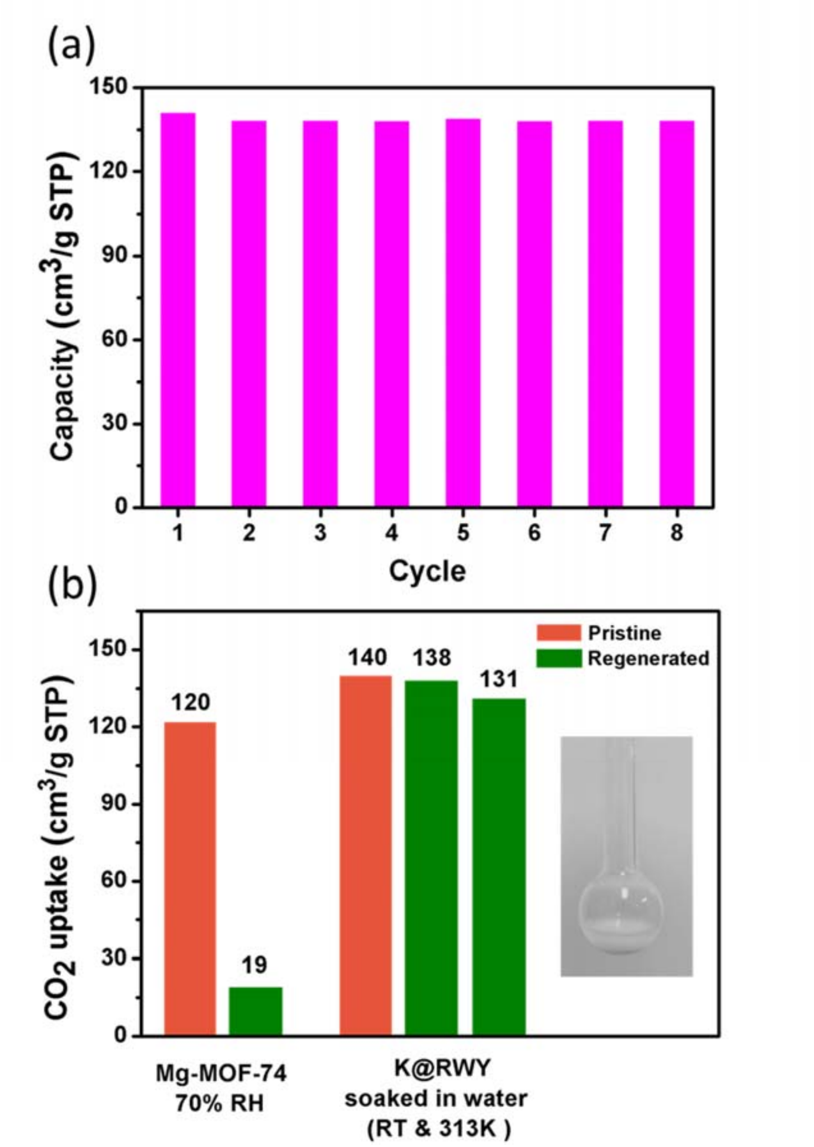

Figure 4.12 (a) Eight cycles of CO_2 uptake of K@RWY at 273 K and 1 atm. (b) CO_2 capacities of pristine Mg-MOF-74 and regenerated Mg-MOF-74 samples after hydration at 70% RH (data from ref. 26) versus CO_2 capacities of K@RWY and regenerated K@RWY samples after soaking in water for 24 hours at RT (left) and 313 K (right). Inset shows the picture of K@RWY soaking in water.

4.4 Conclusion

In summary, we have successfully synthesized a series of cation-exchanged samples through a post-synthetic stepwise ion-exchange strategy and evaluated their application in CO_2 adsorption. The results demonstrated that the samples of Cs@RWY, Rb@RWY, and K@RWY exhibited excellent CO_2 adsorption properties, which could be ascribed to the strong interaction between highly polarizable CO_2 and 'soft' electron-rich sulfur surface, as well as the interactions between extra-framework cations and CO_2. Particularly, the best performance was found in K@RWY with the highest uptake of 6.3 mmol/g at 273 K and 1 atm and the adsorption heat (35.0-41.1 mol^{-1}). More importantly, the N_2 adsorption of K@RWY under 298 K and even 273 K cannot be detected, which indicates an extraordinarily high CO_2/N_2 selectivity. Notably, it is also the best performance among all the reported chalcogenide materials. In addition, K@RWY also exhibited a good recyclability and a strong tolerance towards water.

4.5 Reference

(1) Lu, W.; Sculley, J. P.; Yuan, D.; Krishna, R.; Wei, Z.; Zhou, H. C. *Angew. Chem. Int. Ed.*, 2012, **51**, 7480-7484.

(2) Haszeldine, R. S. *Science*, 2009, **325**, 1647-1652.

(3) Rochelle, G. T. *Science*, 2009, **325**, 1652-1654.

(4) Yu, K. M. K.; Curcic, I.; Gabriel, J.; Tsang, S. C. E. *ChemSusChem*, 2008, **1**, 893-899.

(5) Wang, Q.; Luo, J.; Zhong, Z.; Borgna, A. *Energy Environ. Sci.*, 2011, **4**, 42-55.

(6) Xu, X.; Song, C.; Andresen, J. M.; Miller, B. G.; Scaroni, A. W. *Energy Fuels*, 2002, **16**, 1463-1469.

(7) Stuckert, N. R.; Yang, R. T. *Environ. Sci. Technol.*, 2011, **45**, 10257-10264.

(8) Li, G.; Xiao, P.; Webley, P.; Zhang, J.; Singh, R.; Marshall, M. *Adsorption*, 2008, **14**, 415-422.

(9) Merel, J.; Clausse, M.; Meunier, F. *Ind. Eng. Chem. Res.*, 2008, **47**, 209-215.

(10) Liu, Q.; Cheung, N. C. O.; Garcia-Bennett, A. E.; Hedin, N. *ChemSusChem*, 2011, **4**, 91-97.

(11) Deroche, I.; Gaberova, L.; Maurin, G.; Llewellyn, P.; Castro, M.; Wright, P. *Adsorption*, 2008, **14**, 207-213.

(12) Zhao, X. X.; Xu, X. L.; Sun, L. B.; Zhang, L. L.; Liu, X. Q. *Energy Fuels*, 2009, **23**, 1534-1538.

(13) Lu, C.; Bai, H.; Wu, B.; Su, F.; Fen-Hwang, J. *Energy Fuels*, 2008, **22**, 3050-3056.

(14) Hao, G. P.; Li, W. C.; Qian, D.; Lu, A. H. *Adv. Mater.*, 2010, **22**, 853-857.

(15) Dawson, R.; Stöckel, E.; Holst, J. R.; Adams, D. J.; Cooper, A. I. *Energy Environ. Sci.*, 2011, **4**, 4239-4245.

(16) Thallapally, P. K.; McGrail, B. P.; Atwood, J. L.; Gaeta, C.; Tedesco, C.; Neri, P. *Chem. Mater.*, 2007, **19**, 3355-3357.

(17) McDonald, T. M.; D'Alessandro, D. M.; Krishna, R.; Long, J. R. *Chem. Sci.*, 2011, **2**, 2022-2028.

(18) McDonald, T. M.; Lee, W. R.; Mason, J. A.; Wiers, B. M.; Hong, C. S.; Long, J. R. *J. Am. Chem. Soc.*, 2012, **134**, 7056-7065.

(19) Mason, J. A.; Sumida, K.; Herm, Z. R.; Krishna, R.; Long, J. R. *Energy Environ. Sci.*, 2011, **4**, 3030-3040.

(20) D'Alessandro, D. M.; Smit, B.; Long, J. R. *Angew. Chem. Int. Ed.*, 2010, **49**, 6058-6082.

(21) Sumida, K.; Rogow, D. L.; Mason, J. A.; McDonald, T. M.; Bloch, E. D.; Herm, Z. R.; Bae, T.-H.; Long, J. R. *Chem. Rev.*, 2011, **112**, 724-781.

(22) Zhao, X.; Bu, X.; Zhai, Q.-G.; Tran, H.; Feng, P. *J. Am. Chem. Soc*, 2015, **137**, 1396-1399.

(23) Dunne, J.; Rao, M.; Sircar, S.; Gorte, R.; Myers, A. *Langmuir*, 1996, **12**, 5896-5904.

(24) Liang, Z.; Marshall, M.; Chaffee, A. L. *Energy Fuels*, 2009, **23**, 2785-2789.

(25) Zuluaga, S.; Fuentes-Fernandez, E. M.; Tan, K.; Xu, F.; Li, J.; Chabal, Y. J.; Thonhauser, T. *Journal of Materials Chemistry A*, 2016, **4**, 5176-5183.

(26) Kizzie, A. C.; Wongfoy, A. G.; Matzger, A. J. *Langmuir*, 2011, **27**, 6368-6373.

(27) Ori, G.; Massobrio, C.; Pradel, A.; Ribes, M.; Coasne, B. *Phys. Chem. Chem. Phys.*, 2016, **18**, 13449-13458.

(28) Shafaei - Fallah, M.; Rothenberger, A.; Katsoulidis, A. P.; He, J.; Malliakas, C. D.; Kanatzidis, M. G. *Adv. Mater.*, 2011, **23**, 4857-4860.

(29) Bag, S.; Kanatzidis, M. G. *J. Am. Chem. Soc.*, 2010, **132**, 14951-14959.

(30) Lin, Q.; Bu, X.; Mao, C.; Zhao, X.; Sasan, K.; Feng, P. *J. Am. Chem. Soc*, 2015, **137**, 6184-6187.

(31) Oh, Y.; Bag, S.; Malliakas, C. D.; Kanatzidis, M. G. *Chem. Mater.*, 2011, **23**, 2447-2456.

(32) Shafaei-Fallah, M.; He, J.; Rothenberger, A.; Kanatzidis, M. G. *J. Am. Chem. Soc.*, 2011, **133**, 1200-1202.

(33) Armatas, G. S.; Kanatzidis, M. G. *Nat. Mater.*, 2009, **8**, 217-222.

(34) Akhtar, F.; Liu, Q.; Hedin, N.; Bergström, L. *Energy Environ. Sci.*, 2012, **5**, 7664-7673.

(35) Park, H. J.; Suh, M. P. *Chem. Sci.*, 2013, **4**, 685-690.

(36) Dincă, M.; Long, J. R. *J. Am. Chem. Soc.*, 2007, **129**, 11172-11176.

(37) Bae, T. H.; Hudson, M. R.; Mason, J. A.; Queen, W. L.; Dutton, J. J.; Sumida, K.; Micklash, K. J.; Kaye, S. S.; Brown, C. M.; Long, J. R. *Energy Environ. Sci.*, 2013, **6**, 128-138.

(38) Zheng, N.; Feng, P. *Science*, 2002, **298**, 2366-2369.

(39) Yang, H.; Luo, M.; Luo, L.; Wang, H.; Hu, D.; Lin, J.; Wang, X.; Wang, Y.; Wang, S.; Bu, X.; Feng, P.; Wu, T. *Chem. Mater.*, 2016, **28**, 8774-8780.

(40) Myers, A. L.; Prausnitz, J. M. *AlChE J.*, 1965, **11**, 121-127.

(41) Banerjee, D.; Zhang, Z.; Plonka, A. M.; Li, J.; Parise, J. B. *Crystal Growth & Design*, 2012, **12**, 2162-2165.

(42) Lee, J.-S.; Kim, J.-H.; Kim, J.-T.; Suh, J.-K.; Lee, J.-M.; Lee, C.-H. *J. Chem. Eng. Data*, 2002, **47**, 1237-1242.

(43) Caskey, S. R.; Wong-Foy, A. G.; Matzger, A. J. *J. Am. Chem. Soc.*, 2008, **130**, 10870-10871.

(44) Subrahmanyam, K. S.; Malliakas, C. D.; Sarma, D.; Armatas, G. S.; Wu, J.; Kanatzidis, M. G. *J. Am. Chem. Soc.*, 2015, **137**, 13943-13948.

(45) Millward, A. R.; Yaghi, O. M. *J. Am. Chem. Soc.*, 2005, **127**, 17998-17999.

(46) Britt, D.; Furukawa, H.; Wang, B.; Glover, T. G.; Yaghi, O. M. *Proc. Natl. Acad. Sci. U.S.A.*, 2009, **106**, 20637-20640.

Chapter 5 Zeolitic Porous Chalcogenide Serving as Sulfur-rich Hard Template towards Highly Efficient Electrocatalyst for Oxygen Reduction

5.1 Introduction

Zeolitic porous chalcogenide, as a typical kind of crystalline porous materials (CPMs)[1-13], has attracted extensive attentions owing to its robust and highly porous nature, with cation-exchange property. They have exhibited several promising potential applications,[14-18] including photocatalytic hydrogen evolution, radioactive waste capture, selective photocatalysis and selective carbon dioxide adsorption. As extra-framework charge-balanced species, the cationic species can be evenly distributed inside the cages since the framework is made of well-defined molecular chalcogenide clusters. Through the cation exchange, the custom-design cationic guests with functionality can be encapsulated into the frameworks with uniform distribution.

The strategy mentioned above opens a new avenue to endow zeolitic porous chalcogenide with more functionalities. Mesoporous silica, such as SBA-15, has been widely utilized as the hard template to fabricate the carbon materials.[19-23] In comparison, as a sulfur-rich microporous and robust framework, zeolitic porous chalcogenide can be applied as an ideal matrix for synthesizing highly porous heteroatom-doped carbon materials with plenty number of active sites when carbon based cationic species are diffused into the materials. Due to electroneutrality breakage and charge relocation, the resulting porous heteroatom-decorated carbon materials after thermal treatment possess the tunable surface and fast electron transferring ability, both of which are the necessary prerequisite for developing efficient electrocatalysts.[24-33]

Among various electrocatalytic reactions, oxygen reduction reaction (ORR) has received increasing interest recently due to the scarcity, poor stability and poor methanol tolerance of Pt with its alloy, which are the current widely used electrocatalysts for ORR on cathode in low-temperature fuel cells. Extensive efforts have been devoted to developing high-performance ORR electrocatalysts with long-term durability.[34-42] Some of the recent work discloses that multiple heteroatom codoped nanocarbon materials exhibit synergistic effect for improving ORR activity. By comparing solely nitrogen-doped with nitrogen/sulfur dual doped carbon materials, it was observed that the presence of sulfur improves the overall electrocatalytic activity of the material in both basic and acidic media.[27, 29, 43]

Traditional methods for including sulfur in nitrogen doped-materials involves the pyrolysis of a composite of physically mixed thiourea or thioacetamide and carbon precursors or carbon supports with diffusion of sublimed sulfur. However, these approaches often lead to poor control in surface area, uniform heteroatom dispersion, excellent electron transport and large numbers of accessible active sites. The robust and crystalline zeolitic porous chalcogenide provides an opportunity to eliminate these obstacles and develop highly efficient ORR electrocatalyst.

Herein, we report on a rational design and artful synthesis of highly porous, selfsupported nitrogen/sulfur-containing carbon frameworks with trace amounts of nonprecious metal decoration, showing superior electrocatalytic ORR performance beyond Pt. Unlike random blending and nanocasting the physically mixed mixtures as reported over the years, by adopting step-by-step cation excahnge process, $[Fe(1,10\text{-}phenanthroline)_3]^{2+}$ ($[Fe(Phen)_3]^{2+}$) can be diffused and evenly distributed in the nanocages of the zeolitic porous chalcogenides, followed by thermal treatment and HF leaching to remove the unreactive and large nanoparticles. The as-synthesized electrocatalysts here exhibited a surface area of 684 m^2/g including micropores and mesopores and highly efficent performance, with onsite potential comparable to 20% Pt/C and half-wave potential ($E_{1/2}$, 0.867V) 30mV more positive than that of 20% Pt/C in 0.1M KOH. In addition, it showed excellent long-term durability and high tolerance to methanol crossover. These valuse are among the best in non-precious metal ORR electrocatalysts up to now. Our synthetic strategy here shows that the zeolitic porous chalcogenide can provide a platform to synthesize the carbon materails with even distribution of heteratoms.

5.2 Experienmental Section

5.2.1 Chemicals

Germanium dioxide (GeO_2, 99.999%), gallium nitrate hydrate ($Ga(NO_3)_3 \cdot xH_2O$, 99.9998%) and zinc nitrate hexahydrate ($Zn(NO_3)_2 \cdot 6H_2O$, 98%) were purchased from Acros. N-(2-aminoethyl)-morpholine (AEM, 98%+) and sulfur powder (S, 100mesh, 99.5%) was purchased from Alfa Aesar. All chemicals were used as purchased without further purification.

5.2.2 Synthesis of CPM-120-ZnGaGeS-AEM

125mg GeO_2, 117mg $Ga(NO_3)_3 \cdot xH_2O$, 90mg $Zn(NO_3)_2 \cdot 6H_2O$, 260mg S and 3.0mL AEM were mixed thoroughly in a 23mL Teflon-lined stainless autoclave and stirred for 1 hour. After heating the sealed reaction mixture at 190 °C for 12 days, around 150mg of small pale yellow rhombic-dodecahedral crystals were obtained. The powder impurities can be washed away using methanol. The pure crystals were obtained by filtering and washing with extra methanol. The phase purity was supported by Powder x-ray diffraction (PXRD). The presence and ratio of Zn/Ga/Ge/S were confirmed by energy-dispersive-X-ray (EDX) spectroscopy.

5.2.3 Ion-exchange Experiment

CPM-120-ZnGaGeS-AEM was immersed in 20mL 1M CsCl aqueous solution in a glass vial. The vial was then transferred in an 80 °C oven. During the exchange, the CsCl solution was refreshed every 12 hours. After 2 days, the crystals was filtered and washed with water to remove any residual Cs^+ cations on the surface.

CPM-120-ZnGaGeS-Cs obtained in the first steps was immersed in 20mL 0.05M $Fe(Phen)_3SO_4$ aqueous solution in a glass vial for 3 days at room temperature. During the exchange, the $Fe(Phen)^3SO_4$ solution was refreshed every 12 hours. After 3 days, the crystals was filtered and washed with water then ethanol (each times each) to remove any residual cations on the surface.

5.2.4 Powder X-ray Diffraction

Powder X-ray Diffraction (PXRD) data were performed a Bruker D8 Advance powder diffraction meter with CuKα radiation (40 kV, 40 mA, λ = 1.5418 Å). The simulated powder pattern was calculated using single-crystal X-ray diffraction data of CPM-120-ZnGaGeS and processed by the Mercury 2.3 program provided by the Cambridge Crystallographic Data Centre.

5.2.5 Scanning Electron Microscopy (SEM) and Energy Dispersive Spectroscopy (EDS)

The images and data were carried out on Philips FEI XL30 field emission scanning electron microscope (FESEM) equipped with PGT-IMIX PTS EDS detector, or on Nova Nano-SEM450 (Schottky field emission scanning electron microscope) integrated with EDS allowing to perform qualitative and quantitative chemical analysis and image capture. EDS data acquisition was performed with an accelerating voltage of 20 kV and 60 s accumulation time.

5.2.6 Gas Adsorption

Gas sorption isotherms were measured on a Micromeritics ASAP 2020M surface-area and pore-size analyzer up to 1 atm of gas pressure by the static volumetric method. All gases used were of 99.99% purity, and the impurity trace water was removed by passing the gases through the molecular sieve column equipped in the gas line. The gas sorption isotherms for N_2 were measured at 77 K. All of the samples were degassed at 150 °C overnight before measurement.

5.2.7 Electrocatalytic Performance Measurements

Electrochemical characterization of the catalysts was performed in a conventional three-electrode cell using CHI760D electrochemical workstation (CH Instruments, USA) controlled at room temperature and under atmospheric pressure. Ag/AgCl and platinum wire were used as reference and counter electrodes, respectively. All potentials in this report were converted into reversible hydrogen electrode (RHE). A ring-disk electrode (RDE) with a glassy carbon disk and a Pt ring was served as the substrate for the working electrode. The catalyst ink was prepared by mixing the catalyst powder (5 mg) with 40 μL Nafion solution (5 wt %) and 0.6 mL ethanol in an ultrasonic bath. Then 5 μL of catalyst ink was pipetted onto the GC electrode with a catalyst loading of 0.2 mg cm^{-2} in 0.1 M KOH. As a comparison, commercial 20 wt % platinum on Vulcan carbon black (Pt/C from Alfa Aesar) was prepared by blending Pt/C (10 mg) with 80 μL Nafion solution (5 wt %) and 1.2 mL ethanol in an ultrasonic bath. A Pt loading about 20 μg cm^{-2} was applied in both alkali and acid conditions.

Linear sweep voltammetry (LSV) polarization curves for the oxygen reduction reaction (ORR) were measured in an oxygen saturated 0.1 M KOH electrolyte with a sweep rate of 10 mV s^{-1} at various rotating speeds from 400 to 2500 rpm. The cyclic voltammogram (CV) were recorded insolutions saturated with either Ar or O2 gas without rotation with same sweep rate as that of LSV curve. The electron transfer number (n) and kinetic current density (jK) were analyzed on the basis of Koutecky−Levich equations.

5.3 Results and Discussion

5.3.1 Preparation and Characterization

CPM-120-ZnGaGeS-AEM was employed as the platform here and a step-by-step cation exchange process was realized. As a zeolitic analogue, the basic building blocks in CPM-120-ZnGaGeS-AEM is T2 $[Zn_{0.76}Ga_{0.70}Ge_{2.54}S_8]^{2.22-}$ cluster, joined together by sharing the corner S^{2-} anions and giving a supersodalite type structure. The sodalite cage consists of four- and six-membered rings, among which the aperture size of six-membered ring is 7.66Å. The host framework here is a highly anionic framework, with protonated AEM molecules as charge-balanced species in the channel, which can be substituted by other cationic species. Our previous study also shows that with the dimension size larger than the window size of six-membered ring, the cation exchange process can still be processed, possibly due to the dynamic molecular shapes, as well as possible association and dissociation equilibria of metal-chalcogen bonds in chalcogenide framework. In our step-by-step cation exchange process, the protonated AEM molecules was firstly exchanged completely with Cs^+, which was proved successfully previously. Here it is worth mentioning that CPM-120-ZnGaGeS-AEM has a BET surface area of 499 m^2 g^{-1}, resulting from nitrogen sorption. The Cs^+ can be then replaced by $[Fe(Phen)_3]^{2+}$ (the material obtained are denoted as CPM-120-Cs-Fe(phen)$_3$), which can be proved by the color change with naked eyes and optical microscope, coupled with the characteristic adsorption peak from UV-vis adsorption spectrum. In addition, nitrogen sorption shows that the BET surface area will decrease to 296 m^2 g^{-1}, as the included larger [Fe(Phen)$_3$]$^{2+}$ will block the pores. (Figure 5.1) Other gas adsorption data are also decreased. Calcination process of the iron-included samples at 800°C under argon, followed by the leaching process in 10% HF solution at room temperature were then performed in order to obtain Fe, N, S codoped carbon material with high porosity (denoted as CPM-120-Cs-Fe(phen)$_3$-800). HF leaching process here can remove most of the unreactive species, such as amorphous Ge and Ga, ZnS, iron carbide, iron sulfide and metallic nanoparticles. It is worth noting that the rhombic-dodecahedral shape of the as-synthesized crystal can be retained through the whole process, even after the calcination and HF leaching process.

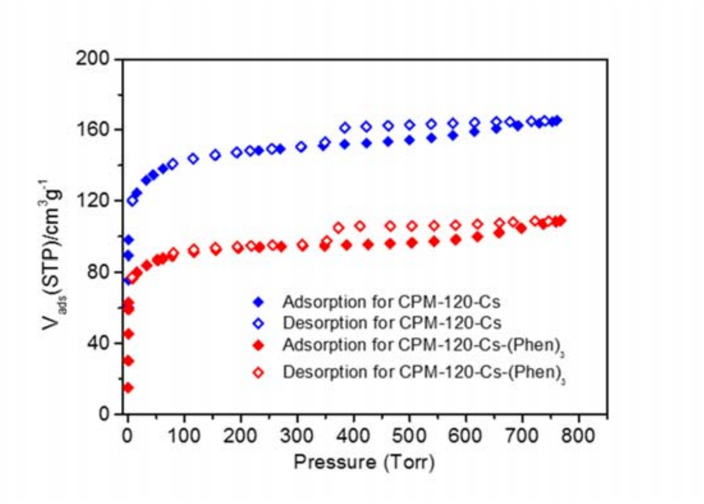

Figure 5.1 Nitrogen sorption isotherms for CPM-120-Cs and CPM-120-Cs-(Phen)$_3$.

The powder X-ray diffraction pattern (PXRD) shows that the peak of CPM-120-Cs-Fe(Phen)$_3$ matched well with the simulated one. (Figure 5.2) SEM-EDX conforms that the ratio of Cs:Fe is around 1:1, consistent with the ICP-OES results. After calcination, PXRD pattern exhibits some strong peaks matching well with Wurlzite-2H ZnS. Besides, the broad shoulder peak in the range of 20-30° belongs to the graphitic carbon materials. However, there is no peak for Ge and Ga species, suggesting that Ge and Ga have been molten during the calcination process and became to the amorphous form. (Figure 5.3) After leaching, the peaks of ZnS in PXRD pattern disappeared. It is worth noting that there are no diffraction peaks relevant to any Fe-related species, suggesting that the iron species are highly dispersed among the carbon frameworks without any large nanoparticles. Nitrogen sorption isotherms at 77K exhibit a typical type IV sorption behavior, where there is a steep increase at ultralow pressure and a slight hysteretic desorption at high pressure, indicating this material possess a high BET surface area of 684 m^2 g^{-1} with hierarchical pores including both of micro- and mesopores. (Figure 5.4) Here the Fe, N, S-codoped carbon material with hierarchical porous structure can greatly contribute to the ORR activity through the synergistic effect.

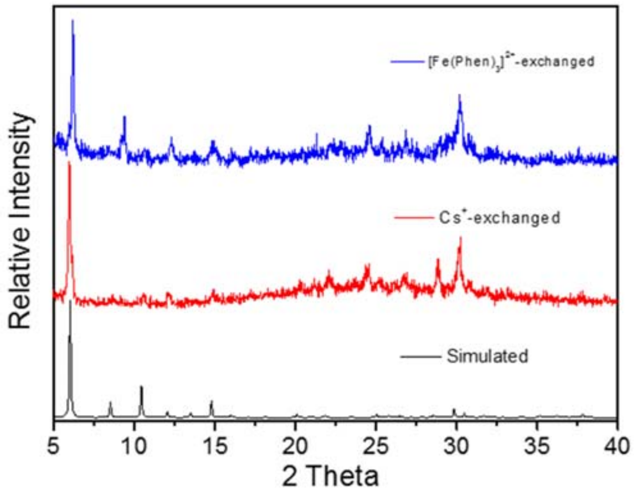

Figure 5.2 PXRD patterns for CPM-120-Cs and CPM-120-Cs-$(Phen)_3$.

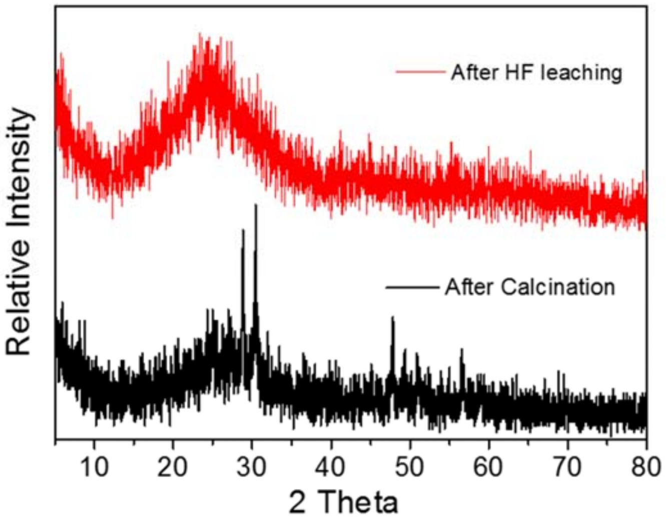

Figure 5.3 PXRD patterns for CPM-120-Cs-(Phen)3 after calcination and then after HF leaching.

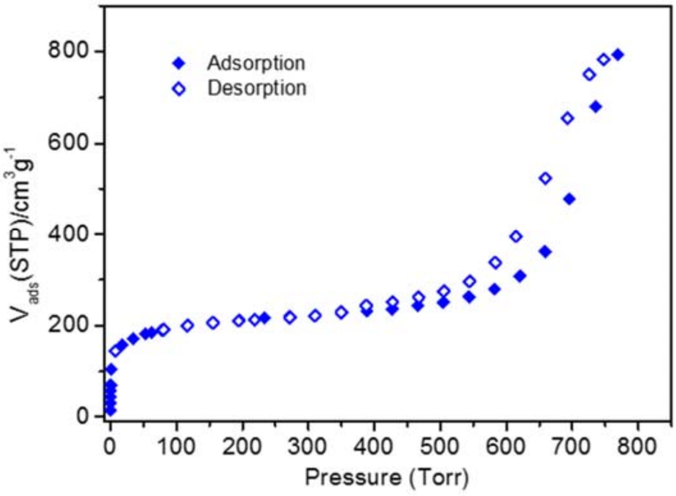

Figure 5.4 Nitrogen sorption isotherms for CPM-120-Cs-(Phen)3-800-HF.

5.3.2 Catalytic Activity Evaluation

The ORR activity was firstly investigated in O_2-saturated alkaline solution (0.1M KOH) by using rotating disk electrode (RDE) at room temperature. Cyclic voltammograms (CVS) of CPM-120-Cs-Fe(phen)$_3$-800 were measure in O_2- or N_2-saturated 0.1M KOH solution, exhibiting an apparent reduction in the CV profile of O2-saturated case, where there is no virtual slopes for the cathodic current in Ar-saturated solutions. (Figure 5.5) Steady-state linear sweep voltammetry (LSV) curves with a scan rate of 10mV s^{-1} indicate that the material here are among the best ORR electrocatalysts. The onsite potential is 0.956V, which is comparable to the commercial 20% Pt/C (0.938V). In comparison, the half-wave potential ($E_{1/2}$) is ~30mV more positive than that of Pt/C. (0.867V for CPM-120-Cs-Fe(phen)$_3$-800 vs. 0.838V for 20% Pt/C). (Figure 5.6)

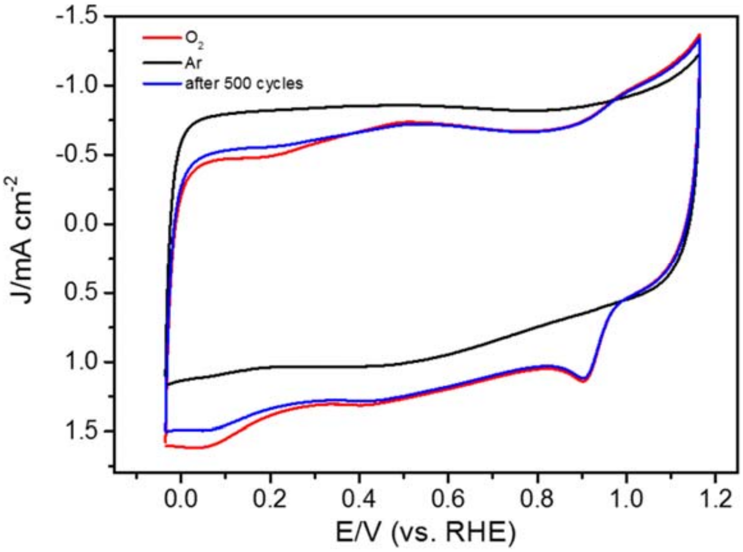

Figure 5.5 CV curves of CPM-120-Cs-(Phen)$_3$-800 in O_2- and Ar-saturated 0.1M KOH.

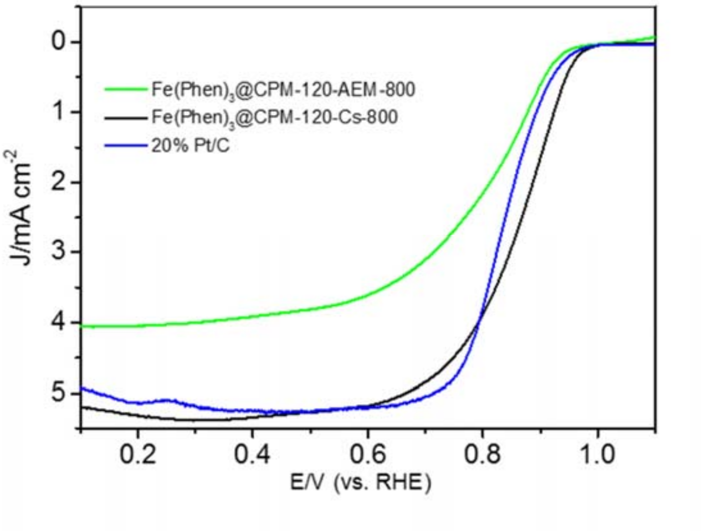

Figure 5.6 RDE voltammograms of CPM-120-Cs-(Phen)$_3$-800, CPM-120-AEM-(Phen)$_3$-800 and 20% Pt/C in O_2-saturated 0.1M KOH.

LSV curves were also measured at different rotation rates in order to reveal their catalytic reaction pathways. The corresponding Koutecky-Levich (K-L) plots were shown in Figure 5.7 and 5.8. The electron transfer numbers were calculated based on the slope of KL plots with a number of 3.88, approaching the theoretical value of 4.0 for Pt/C. This number indicate the four-electron reduction process to produce water is favored, a quite promising characteristic for fuel cell applications.

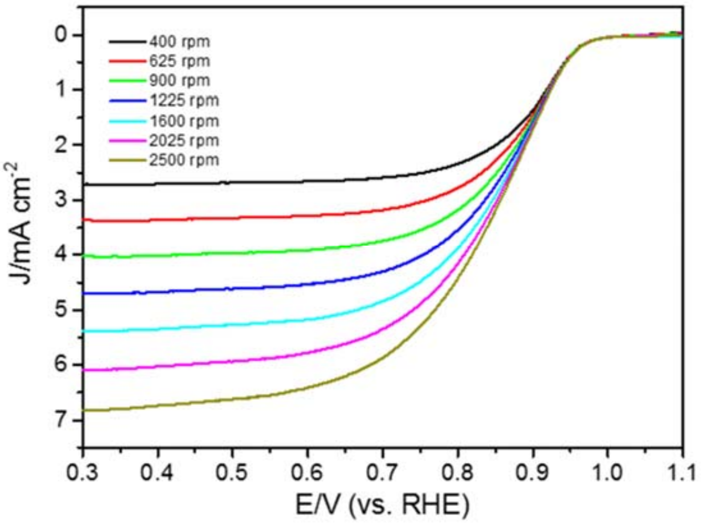

Figure 5.7 RDE voltammograms at different rotation rates of CPM-120-Cs-(Phen)$_3$-800 in O$_2$-saturated 0.1M KOH.

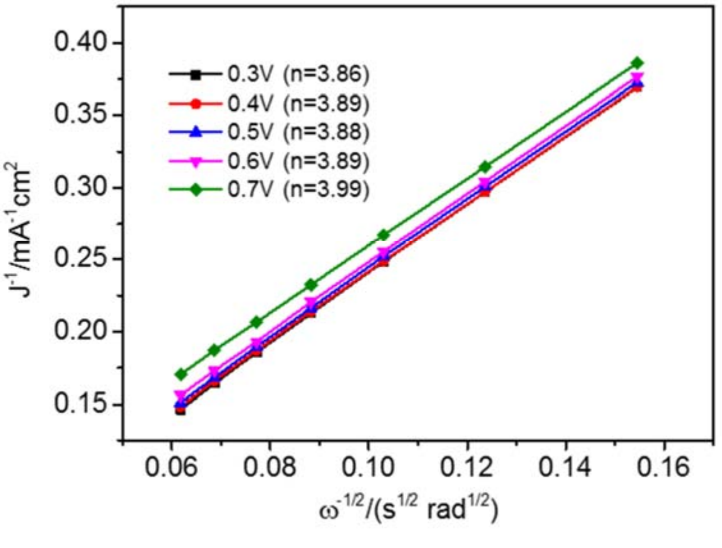

Figure 5.8 Koutecky-Levich plots (bottom) of CPM-120-Cs-(Phen)$_3$-800 in O$_2$-saturated 0.1M KOH.

In addition, several controlled experiments were performed in order to prove that the chemical composition of zeolitic chalcogenide analogue, along with the step-by-step cation exchange process, are crucial to realize the highest ORR performance. UCR-20-GaGeS-Cs here were employed here to show the key role of formed ZnS shell after calcination. UCR-20-GaGeS-Cs is analogous to CPM-120-ZnGaGeS-Cs, but based on a zinc-free T2 cluster. After step-by-step cation exchange, calcination and HF leaching process, the material obtained is denoted as UCR-20-Cs-Fe(Phen)$_3$-800. As shown in Figure 5.9, the ORR performance of UCR-20-Cs-Fe(Phen)$_3$-800 is lower than that of CPM-120-Cs-Fe(Phen)$_3$-800, in terms of both of onsite and half-wave potentials. The onsite and half-wave potential of UCR-20-Cs-Fe(Phen)$_3$-800 is 0.921V and 0.851V, respectively, which are still comparable of those of 20% Pt/C. However, the measured current density is much lower than CPM-120-Cs-Fe(Phen)$_3$-800 and 20% Pt/C.. Moreover, step-by-step cation exchange process is necessary for preparing the highly efficient electrocatalyst. The protonated AEM molecules were directly ion-exchanged by Fe(Phen)$_3^{2+}$, and the final material is denoted as CPM-120-AEM-Fe(Phen)$_3$-800. The obtained material shows relatively low ORR activity, as shown in Figure . The poor performance here can be attributed to two reasons: 1). due to the bulky protonated amine molecules in the channel, the cation exchange process should be much slower than that with Cs$^+$, implying less iron-related active sites; 2). as the cation exchange process is not sufficient, there are quite a few amounts of protonated amines left in the channel, these sp^3-carbon-containing alkyl amines would not make contributions to the conductivity of the electrocatalysts after calcination process. The crucial step-by-step process is further proved in UCR-20-GaGeS-

TAEA and UCR-20-GaGeS-Cs, where TAEA is another kind of alkyl amine molecules. (Figure 5.10)

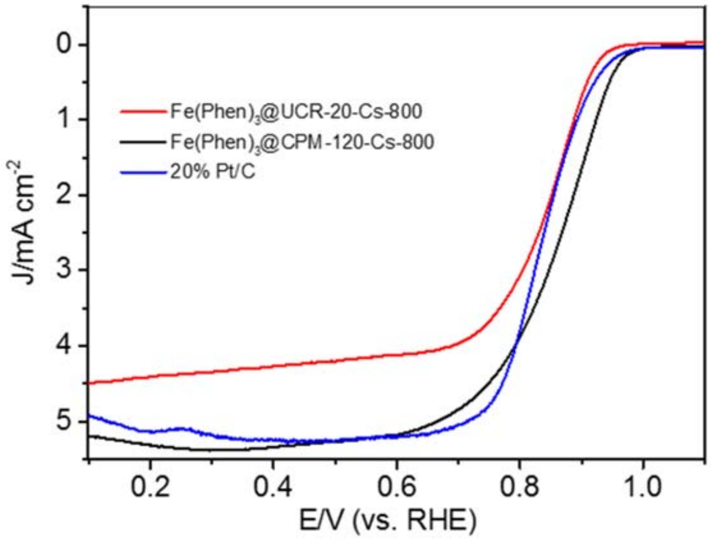

Figure 5.9 RDE voltammograms of UCR-20-Cs-(Phen)$_3$-800, CPM-120-Cs-(Phen)$_3$-800 and 20% Pt/C in O_2-saturated 0.1M KOH.

To investigate the methanol-crossover effects and durability, the chronoamperometric measurements were carried out. CPM-120-Cs-Fe(phen)$_3$-800 shows a stable current-time (*i*-t) chronoamperometric response after the addition of 3.0M methanol, exhibiting potential application in methanol fuel cells. In addition, for the sustainable practical application of fuel cell electrocatalysts, their long-term durability is critical. In the first stability test, no obvious changes were observed in the peak current of the CV curves after 5000 cycles. Moreover, the chronoamperometric durability test shows that after 50,000 seconds, the current density decays only a little, still maintaining 95% of the initial current density, a remarkedly better long-term stability than commercial 20% Pt/C.

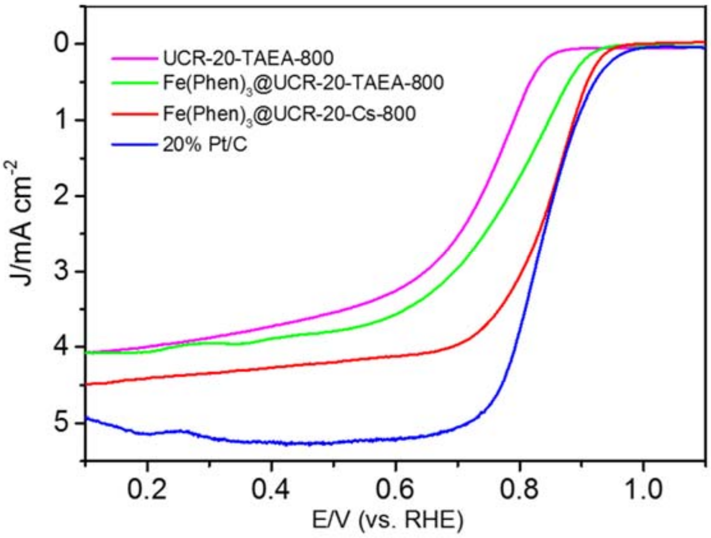

Figure 5.10 RDE voltammograms of UCR-20-TAEA-800, UCR-20-TAEA-(Phen)$_3$-800, UCR-20-Cs-(Phen)$_3$-800 and 20% Pt/C in O_2-saturated 0.1M KOH.

All of the results here are in agreement with the CV curve observations and conform that the zeolitic porous chalcogenide materials can significantly enhance the ORR catalytic activity, due to its robust and highly porous nature, reflected from the high surface area.

5.4 Conclusion

By adopting the step-by-step cation exchange, the hierarchical porous carbon frameworks with uniform nitrogen, sulfur, iron distribution was successfully synthesized. The resulting materials can be functionalized as quite efficient ORR electrocatalyst, showing superior onsite and half-wave potential beyond Pt/C in alkaline solution. The excellent performance here can be attributed to the well-defined crystalline zeolitic porous chalcogenide, with high surface area and high-density heteroatoms evenly distributed inside the frameworks. The design concept presented here to heteroatom doping, especially for the design of S-doped materials, is quite general and amenable to the extension of the compositional scope of the high-surface-area catalysts with more exposed active sites for practical applications.

5.5 Reference

(1) Lin, Y.; Massa, W.; Dehnen, S. *J. Am. Chem. Soc.*, 2012, **134**, 4497-4500.

(2) Li, H.; Kim, J.; Groy, T. L.; O'Keeffe, M.; Yaghi, O. M. *J. Am. Chem. Soc.*, 2001, **123**, 4867-4868.

(3) Cahill, C. L.; Parise, J. B. *J. Chem. Soc., Dalton Trans.*, 2000, 1475-1482.

(4) Li, H.; Laine, A.; Keeffe, M.; Yaghi, O. M. *Science*, 1999, **283**, 1145.

(5) Li, H.; Eddaoudi, M.; Laine, A.; O'Keeffe, M.; Yaghi, O. M. *J. Am. Chem. Soc.*, 1999, **121**, 6096-6097.

(6) Cahill, C. L.; Ko, Y.; Parise, J. B. *Chem. Mater.*, 1998, **10**, 19-21.

(7) Cahill, C. L.; Ko, Y.; Hanson, J. C.; Tan, K.; Parise, J. B. *Chem. Mater.*, 1998, **10**, 1453-1458.

(8) Cahill, C. L.; Parise, J. B. *Chem. Mater.*, 1997, **9**, 807-811.

(9) Zhang, X.-M.; Sarma, D.; Wu, Y.-Q.; Wang, L.; Ning, Z.-X.; Zhang, F.-Q.; Kanatzidis, M. G. *J. Am. Chem. Soc.*, 2016, **138**, 5543-5546.

(10) Fang, L.; Iyer, R. G.; Tan, G.; West, D. J.; Zhang, S.; Kanatzidis, M. G. *J. Am. Chem. Soc.*, 2014, **136**, 11079-11084.

(11) Vaqueiro, P.; Romero, M. L.; Rowan, B. C.; Richards, B. S. *Chemistry – A European Journal*, 2010, **16**, 4462-4465.

(12) Vaqueiro, P.; Romero, M. L. *Inorg. Chem.*, 2009, **48**, 810-812.

(13) Vaqueiro, P.; Romero, M. L. *J. Am. Chem. Soc.*, 2008, **130**, 9630-9631.

(14) Hu, D.; Zhang, Y.; Lin, J.; Hou, Y.; Li, D.; Wu, T. *Dalton Transactions*, 2017, **46**, 3929-3933.

(15) Lin, Q.; Bu, X.; Mao, C.; Zhao, X.; Sasan, K.; Feng, P. *J. Am. Chem. Soc.*, 2015, **137**, 6184-6187.

(16) Zheng, N. F.; Bu, X. G.; Wang, B.; Feng, P. Y. *Science*, 2002, **298**, 2366-2369.

(17) Chen, X.; Bu, X.; Lin, Q.; Mao, C.; Zhai, Q.-G.; Wang, Y.; Feng, P. *Chemistry – A European Journal*, 2017, **23**, 11913-11919.

(18) Yang, H.; Luo, M.; Luo, L.; Wang, H.; Hu, D.; Lin, J.; Wang, X.; Wang, Y.; Wang, S.; Bu, X.; Feng, P.; Wu, T. *Chem. Mater.*, 2016, **28**, 8774-8780.

(19) Wang, Y.-g.; Xia, Y.-y. *Electrochim. Acta*, 2006, **51**, 3223-3227.

(20) Han, Y.-J.; Kim, J. M.; Stucky, G. D. *Chem. Mater.*, 2000, **12**, 2068-2069.

(21) Wang, Y. M.; Wu, Z. Y.; Shi, L. Y.; Zhu, J. H. *Adv. Mater.*, 2005, **17**, 323-327.

(22) Joo, S. H.; Choi, S. J.; Oh, I.; Kwak, J.; Liu, Z.; Terasaki, O.; Ryoo, R. *Nature*, 2001, **412**, 169-172.

(23) Gao, F.; Lu, Q.; Zhao, D. *Adv. Mater.*, 2003, **15**, 739-742.

(24) Yang, L.; Jiang, S.; Zhao, Y.; Zhu, L.; Chen, S.; Wang, X.; Wu, Q.; Ma, J.; Ma, Y.; Hu, Z. *Angew. Chem.*, 2011, **123**, 7270-7273.

(25) Wang, S.; Iyyamperumal, E.; Roy, A.; Xue, Y.; Yu, D.; Dai, L. *Angew. Chem. Int. Ed.*, 2011, **50**, 11756-11760.

(26) Zhao, Y.; Yang, L.; Chen, S.; Wang, X.; Ma, Y.; Wu, Q.; Jiang, Y.; Qian, W.; Hu, Z. *J. Am. Chem. Soc.*, 2013, **135**, 1201-1204.

(27) Liang, J.; Jiao, Y.; Jaroniec, M.; Qiao, S. Z. *Angew. Chem. Int. Ed.*, 2012, **51**, 11496-11500.

(28) Wang, X.; Wang, J.; Wang, D.; Dou, S.; Ma, Z.; Wu, J.; Tao, L.; Shen, A.; Ouyang, C.; Liu, Q. *Chem. Commun.*, 2014, **50**, 4839-4842.

(29) Zhang, Y.; Chu, M.; Yang, L.; Deng, W.; Tan, Y.; Ma, M.; Xie, Q. *Chem. Commun.*, 2014, **50**, 6382-6385.

(30) Silva, R.; Voiry, D.; Chhowalla, M.; Asefa, T. *J. Am. Chem. Soc.*, 2013, **135**, 7823-7826.

(31) Liang, H.-W.; Wei, W.; Wu, Z.-S.; Feng, X.; Müllen, K. *J. Am. Chem. Soc.*, 2013, **135**, 16002-16005.

(32) Ding, W.; Wei, Z.; Chen, S.; Qi, X.; Yang, T.; Hu, J.; Wang, D.; Wan, L. J.; Alvi, S. F.; Li, L. *Angew. Chem.*, 2013, **125**, 11971-11975.

(33) Sa, Y. J.; Park, C.; Jeong, H. Y.; Park, S. H.; Lee, Z.; Kim, K. T.; Park, G. G.; Joo, S. H. *Angew. Chem.*, 2014, **126**, 4186-4190.

(34) Wang, Y.; Kong, A.; Chen, X.; Lin, Q.; Feng, P. *Acs Catalysis*, 2015, **5**, 3887-3893.

(35) Cheng, Q.; Yang, L.; Zou, L.; Zou, Z.; Chen, C.; Hu, Z.; Yang, H. *ACS Catalysis*, 2017, **7**, 6864-6871.

(36) Yasuda, S.; Furuya, A.; Uchibori, Y.; Kim, J.; Murakoshi, K. *Adv. Funct. Mater.*, 2016, **26**, 738-744.

(37) Chen, P.; Zhou, T.; Xing, L.; Xu, K.; Tong, Y.; Xie, H.; Zhang, L.; Yan, W.; Chu, W.; Wu, C. *Angew. Chem. Int. Ed.*, 2017, **56**, 610-614.

(38) Chen, Y.; Ji, S.; Wang, Y.; Dong, J.; Chen, W.; Li, Z.; Shen, R.; Zheng, L.; Zhuang, Z.; Wang, D. *Angew. Chem.*, 2017, **129**, 7041-7045.

(39) Shen, H.; Gracia‐Espino, E.; Ma, J.; Zang, K.; Luo, J.; Wang, L.; Gao, S.; Mamat, X.; Hu, G.; Wagberg, T. *Angew. Chem. Int. Ed.*, 2017, **56**, 13800-13804.

(40) Han, Y.; Wang, Y.-G.; Chen, W.; Xu, R.; Zheng, L.; Zhang, J.; Luo, J.; Shen, R.-A.; Zhu, Y.; Cheong, W.-C. *J. Am. Chem. Soc.*, 2017.

(41) Zhang, H.; Hwang, S.; Wang, M.; Feng, Z.; Karakalos, S.; Luo, L.; Qiao, Z.; Xie, X.; Wang, C.; Su, D. *J. Am. Chem. Soc.*, 2017, **139**, 14143-14149.

(42) Wang, Y.; Chen, X.; Lin, Q.; Kong, A.; Zhai, Q.-G.; Xie, S.; Feng, P. *Nanoscale*, 2017, **9**, 862-868.

(43) Chen, C.; Yang, X.-D.; Zhou, Z.-Y.; Lai, Y.-J.; Rauf, M.; Wang, Y.; Pan, J.; Zhuang, L.; Wang, Q.; Wang, Y.-C. *Chem. Commun.*, 2015, **51**, 17092-17095.